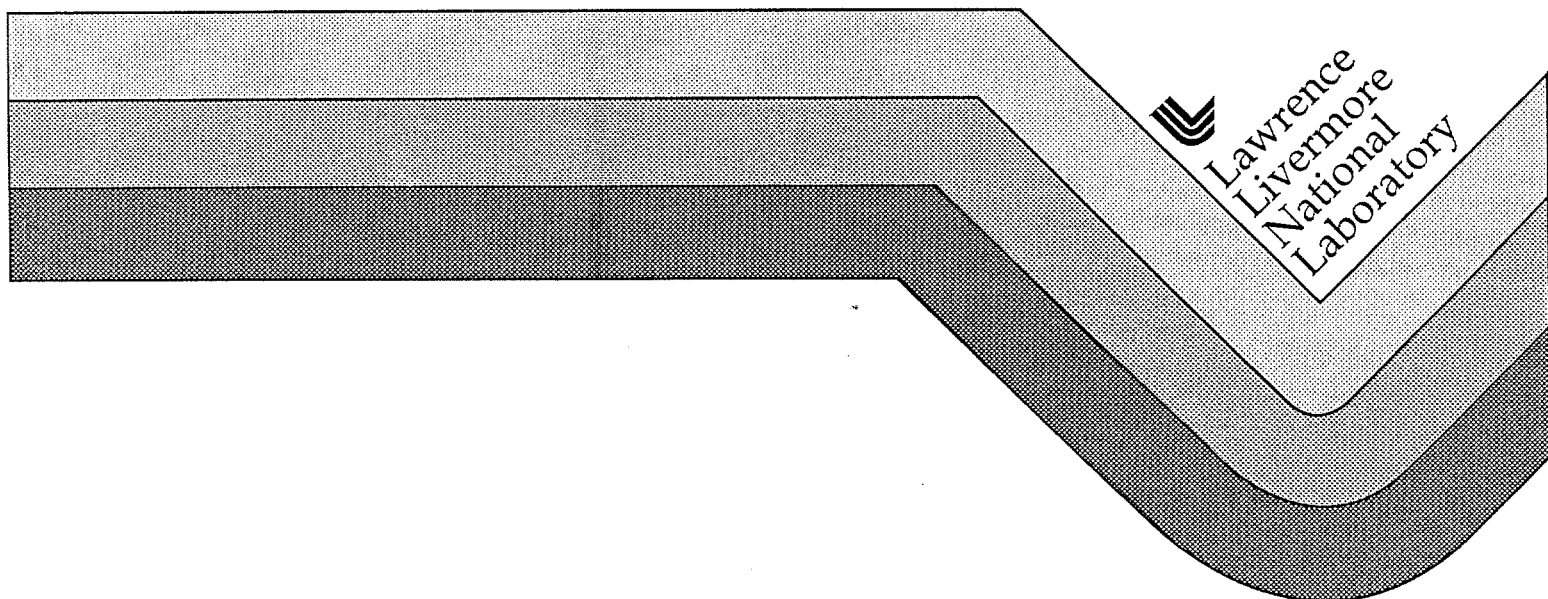# Numerical Investigation of the Thrust Efficiency of a Laser Propelled Vehicle

James Randolph Mulroy
Stanford University

August, 1990

Lawrence
Livermore
National
Laboratory

DISCLAIMER

NUMERICAL INVESTIGATION OF THE THRUST EFFICIENCY

OF A LASER PROPELLED VEHICLE

A DISSERTATION

SUBMITTED TO THE DEPARTMENT OF AERONAUTICS AND ASTRONAUTICS

AND THE COMMITTEE ON GRADUATE STUDIES

IN PARTIAL FULFILLMENT OF THE REQUIREMENTS

FOR THE DEGREE OF

DOCTOR OF PHILOSOPHY

By

James Randolph Mulroy

August 1990

i

ii

I certify that I have read this dissertation and that in my opinion it is fully adequate, in scope and quality, as a dissertation for the degree of Doctor of Philosophy.

_____

I-Dee Chang (Principal Advisor)

I certify that I have read this dissertation and that in my opinion it is fully adequate, in scope and quality, as a dissertation for the degree of Doctor of Philosophy.

_____

Brian Cantwell

I certify that I have read this dissertation and that in my opinion it is fully adequate, in scope and quality, as a dissertation for the degree of Doctor of Philosophy.

_____

Robert MacCormack

I certify that I have read this dissertation and that in my opinion it is fully adequate, in scope and quality, as a dissertation for the degree of Doctor of Philosophy.

_____

Milton Van Dyke

Approved for the University Commitee
on Graduate Studies:

_____

Dean of Graduate Studies

iii

Abstract

The flow situation for a thruster propelled by ablated gas which is energized by a laser pulse is numerically simulated. The flow is axisymmetric and nonsteady, and is assumed to be inviscid due to its high Reynolds number.

The high pressure expansion of the laser heated gas generates thrust as it pushes against the vehicle. Gas expansion lateral to the thrust vector causes performance to decrease. The vehicle geometry and the laser pulse characteristics determine the degree to which the flow is one dimensional. As the thruster's parameters are varied, its impulse is calculated and compared to the limiting impulse of a one-dimensional system, and thus the thrust efficiency is computed.

Lateral expansion losses computed by simulating the flow of the expanding gas time-accurately on a computer are far less than losses predicted using the method of characteristics, which is the best alternate means of computation. Flows which exhibit a substantial amount of lateral expansion can still yield an expansion efficiency which exceeds 70%. This finding has significant implications on the eventual design of flight hardware.

Steger and Warming's flux split numerics for the Euler equations are modified for blast simulations into near vacuum ambient conditions. At the interface between the near vacuum ambient and the wave front, the solution is first order accurate but sufficiently robust to handle pressure ratios exceeding one million and density ratios exceeding 10,000 between the thrust gas and the ambient gas. Elsewhere the solution is second order accurate.

The majority of the calculations performed assume an ideal gas equation of state

with $\gamma = 1.2$. The propellant Lithium Hydride has shown excellent promise in the laboratory, yielding $I_{sp} = 800 - 1000$ sec. Equilibrium and kinetic modeling of LiH is undertaken, with a variable γ of from 1.25 to 1.66 resulting from the kinetic assumptions of ionization equilibrium and frozen chemistry. These additional mechanisms are then incorporated into the efficiency calculations.

Preface

When I mention the phrase *laser propulsion* to my fellow students and professors, I get mixed reactions. Some people are enthusiastic about the concept, and an equal number are pessimistic. The idea of remotely powering a vehicle with a laser has only recently become feasible, although the concept under study here was first advanced by Arthur Kantrowitz in 1972. Advances in high energy lasers have made it possible to seriously talk about laser propulsion. No data within this thesis is classified, and during its preparation I never saw any classified information. This is because laser power figures are some of today's most zealously guarded secrets. Yet it suffices to say that the capability for a ground based pulsed laser to deliver a time averaged power in the megawatt range to a thruster which is climbing in the sky is a minimum requirement for a launch to orbit system. This capability is either in place today, or it is believed by those in the know to be achievable in the future.

This thesis is about the gasdynamics of laser propulsion, and studies the expansion efficiency of the blast wave generated when the propellant is superheated by laser. The fundamental research which has made it possible to understand the gasdynamics of laser propulsion begins at the turn of the century when Chapman (1899) and Jouget (1905) obtained the relation for the speed of a self-propagating detonation, today called the CJ condition. In 1965, the Soviet physicist Razier[4] used a CJ analysis to explain the dynamics of a new phenomenon, the laser supported detonation wave, now called the LSD wave. The LSD wave is the means by which a ground based laser supplies energy to the propellant in the system concept advanced by Kantrowitz[3] in 1972. Analysis of the blast wave following the laser heating is reliant on the work of Taylor[17] and Sedov[23]. These investigators,

vi

working independently of each other in the era of World War II and publishing after the war, obtained solutions for the blast wave in situations where the flow exhibits plane, cylindrical, or spherical symmetry. Laser propulsion blast does not in general exhibit this symmetry, and so numerical solution is required. The numerical algorithm making a realistic simulation possible is called Flux Vector Splitting, which was published in 1981 by Steger and Warming[20].

In this dissertation, there are about 50 figures. These were generated over time as the research progressed, and are of varying graphical sophistication. Each figure is one full page long. The figures are included at the end of the manuscript because otherwise: 1.) The manuscript would appear choppy, and 2.) The manuscript would be very difficult to edit. The manuscript was prepared in TEX and many of the figures were generated using the Claris MacDraw II program for the Apple MacIntosh, and MATLAB.

Acknowledgements

Table of Contents

List of Tables

List of Figures

Chapter One

Overview of Laser Propulsion and Problem Definition

Part 1: Introduction to Pulsed Laser Propulsion

A combination of factors have motivated a pulsed laser propulsion effort directed by the United States Department of Energy.

First, launch costs into low earth orbit using chemical rockets continue to be quite high, in the range of $2,500 per pound to low earth orbit[1]. Thus, for the price of launching 400 lb. to orbit the government can finance a 1 million dollar research program into something that might prove to be far less expensive than chemical rockets.

Second, high energy ground based pulsed lasers are being developed for military and scientific applications in the United States and abroad. The laser propulsion program is a consequence of this fact–the lasers are coming, so it is reasonable to find new applications for them. The program unabashedly takes advantage of the military character of work being done. Zapping a laser thruster into space is essentially the inverse of the problem of zapping an incoming re-entry vehicle[2]. We assume a laser propulsion system could be built once a working thruster is achieved, because the work on the other components to the system– laser hardware, pointing and tracking, and atmospheric beam propagation–is presently being done under the auspices of the SDIO.

And third, although a simple power analysis makes launching a manned vehicle into space via laser unrealistic, the trend towards miniaturization in high technology components and systems integration makes a small launch vehicle feasible. Should

laser propulsion prove workable and provide an inexpensive conveyor belt into space, certain missions involving many thousands of small vehicles become much more affordable. For example, a constellation of small space platforms capable of thwarting a ballistic missile attack has been suggested as a means of strategic defense. While the latter mission is military, the civilian uses of laser propulsion technology would also be considerable. As a rapid, low cost means of placing material into orbit, a laser propulsion system could be used to resupply the Space Station or to ferry up raw materials for space processing. Other applications will follow if the basic system becomes a reality.

Pulsed laser propulsion systems have interesting engineering merits, the chief of which is the fact that a laser propelled vehicle is remotely powered. While the precise system concepts are still subject to change, the overall idea of a pulsed laser system is deemed to be worth investigating because its potential performance per unit cost is higher than that for chemical rockets. Figure 1.1 shows the overall concept. Another significant feature of a laser propelled vehicle is the high exhaust velocity of its propellant. Unlike a chemical rocket which must carry both its fuel and oxidizer along with it, The pulsed laser system studied here will carry an ablative material as the propellant. The amount of energy supplied by the laser per unit mass of propellant can be greater than that supplied by chemical reactions alone, yielding higher exhaust velocities and specific impulse for laser systems. To refresh, the formula for the velocity change ΔV of a rocket is

$$\Delta V = g \; Isp \; \ln (MR) \qquad (1.1.1)$$

$$\Delta V \equiv c \; ln \; MR \qquad (1.1.2)$$

Where c is the effective exhaust velocity, Isp is the specific impulse, in seconds, g is the acceleration due to gravity, and MR is the ratio of the initial to the final mass of

2

the vehicle. The logarithmic character of the equation greatly favors high Isp; other factors have to be considered when selecting the ideal Isp for a given mission but in general the desire for a low total vehicle mass is a strong one, favoring as high an Isp as can be efficiently achieved. For ground to LEO missions, the final velocity of the vehicle is about 10 km/sec which leads to the conclusion that an effective exhaust velocity in the range of c = 10km/sec ($Isp = 1020$ sec) is optimal, and this speed is twice that which can be achieved via chemical propulsion. However, the ground to LEO mission also requires high thrust, presently ruling out such systems as ion and nuclear propulsion. The laser propulsion system planned is also a high thrust system, as illustrated by a sample calculation [Appendix 1].

Two possible ablative schemes have been introduced for a pulsed laser thruster. In a direct ablation scheme, laser absorption takes place at the solid surface and ejects hot gas. Here, Isp is about 300–400 sec. Higher performance is possible if the laser energy is directly deposited into the gas, at a cost of greater complexity. The scheme for doing this was devised by Arthur Kantrowitz in 1972[3]. Two laser pulses are sequenced. The first ablates some propellant material, while the second superheats the ablated gas via a breakdown wave which propagates up the beam axis. This process, which is analogous to a chemical detonation and is called a Laser Supported Detonation (LSD) wave, was first described by the Soviet physicist Razier[4] in 1965. Using Lithium Hydride as the propellant, and a CO_2 pulsed laser operating at a main pulse flux of 5 MW/cm^2 the LSD propagates at 8500 m/s yielding an Isp of 800–1000 sec.

A third potential use of pulsed lasers for propulsion has been experimentally demonstrated by Kare[5]. In this technique, ambient air is broken down by aiming a CO_2 laser operating in the infrared at a dimpled copper mirror. The dimples focus the plane waves of incident laser light to a point, where the flux is great enough to

3

initiate detonation. The hot core of plasma then shields further transmission, and so the wave grows in size. This technique might be coupled with a gas injection system for operation in space if it proves to be the best. Isp's in excess of 1000 sec are possible in air. Schematics of the three candidate systems are presented in Figures 1.2-1.4.

If specific impulse were the sole measure of launcher performance, then a direct ablation laser propulsion system would offer no advantage over a chemical rocket. But high efficiency and design simplicity are the hallmarks of an ablative system. We have yet to determine the overall cost efficiencies of the laser propulsion systems, because thruster efficiency is unknown. Kantrowitz[6] estimates a cost of $1000 per pound to LEO for a 10 MW two-pulse system which launches a 30.4 lb payload. The bottom line figure is cost. In an era of reduced government outlays, cost-efficiency has become increasingly important in the design of aerospace hardware, and is one of the guiding motivations for laser propulsion research. In conjunction with advanced chemical propulsion systems, a successful laser launch system will afford the United States with far greater defense and civilian opportunities in space because the launch costs will be lower than at present.

A summary of chemical propulsion systems and laser propulsion systems is presented in Table 1. The Space Shuttle has been in operation since its maiden flight in 1981, while laser propulsion is still under research. Thus, the laser propulsion figures have yet to be demonstrated in flight hardware. Still, the data show why laser propulsion has attracted attention. In addition to the savings gained by powering the vehicle with commercial electricity generated on the ground, the ability to remotely power a rocket provides for simple, low cost vehicles. The high potential performance of laser propelled vehicles, coupled with the expactation of a low cost system, has motivated the recent efforts in this area.

4

Table 1: Comparison of Specific Impulse for Chemical and Laser Propelled Systems.

System	Specific Impulse (sec)
Chemical Rockets:	
Hydrazine as a monopropellant	205
RP-1 - Oxygen	305
Hydrogen - Oxygen	455
Hydrogen - Fluorine	500
Laser Propulsion:	
Pulse Laser Direct Ablation	300–400
Double Pulse LSD Wave	800–1000
Laser Heating of Air	≈ 1000

The figures in Table 1 are approximate and depend in the chemical case on the combustion chamber pressure. The Space Shuttle Main Engine, fueled by liquid hydrogen and oxygen, operates at a chamber pressure of 202 atm and achieves a vacuum Isp of 455 sec. In comparison, the pressure behind a Lithium Hydride LSD wave supported by 5×10^6 W/cm^2 of CO_2 laser light at 10.6 micrometers has been calculated to be 35 atm[7]. This wave travels at 8500 m/s and in general the effective exhaust velocity of an LSD thruster is about the same as its detonation speed. Hyde[8] has shown that:

$$c \leq \frac{D}{(\gamma^2 - 1)^{\frac{1}{2}}} \qquad (1.1.3)$$

where D is the detonation speed, c is the effective exhaust velocity, and γ is the ratio

of specific heats for the gas, which is assumed constant for this bounding calculation. A perfect LiH thruster operating at a frozen $\gamma = 1.3$ and a D=8500 m/s would achieve c=10,232 m/s for a specific impulse of 1044 s. In two different laboratory experiments with LiH performed on a small scale, Isp's of 800 s and 1000 s have been reported [9][10]. When thinking about pulsed laser propulsion, the microsecond time scales and highly transient nature of the propellant flow situation are very different from those found in conventional chemical rocket flows. However, each separate laser pulse can be analyzed by conventional rocket engineering methods. The effective exhaust velocity for each pulse is the same as the time-averaged effective exhaust velocity. To see this, suppose that there are N pulses per second, which is to say that the pulse frequency is N $(sec)^{-1}$. The impulse recieved per pulse will be denoted I_p (Newton-sec), and the mass ejected per pulse will be denoted M_p (kg). The mass flow rate $\dot{m}$ of propellant is

$$\dot{m} = N M_p \text{ (kg/sec)} \tag{1.1.4}$$

and the average thrust T over one second is

$$T = N I_p \text{ (Newtons)} \tag{1.1.5}$$

So, using the definition of effective exhaust velocity,

$$c \equiv \frac{T}{\dot{m}} \text{ (m/s)} \tag{1.1.6}$$

it is seen that the pulse frequency cancels, and we are left with the result that the effective exhaust velocity can be computed from one pulse.

$$c = \frac{I_p}{M_p} \text{ (m/s)} \tag{1.1.7}$$

6

Part 2: The Two Pulse Model System: Problem Defined.

The two pulse system was singled out for investigation due to its promise. This system pairs two laser pulses in close succession. The first pulse ablates some propellant from the vehicle surface. After a brief expansion of the ablated gas, a main pulse is transmitted which initiates and drives an absorption wave through the gaseous propellant. Behind the absorption wave, which is called a Laser Supported Detonation (LSD) wave, the gas is superheated, giving rise to high pressures. After the main pulse, the expanding blast wave of the hot gas generates much additional thrust. This cycle of ablation, detonation, and blast is repeated, each time applying an impulse to the target vehicle.

As theoretical and computational aerodynamicists, we have been assigned the task of characterizing the gasdynamics of this system. A detailed analysis of the electronic and kinetic processes within the LSD wave is performed by Physical Sciences Incorporated (PSI), and is not the goal of this thesis. Together with experiments performed by other investigators, an ongoing research program headed by Jordin Kare of LLNL has been studying the two pulse system. As necessary for the development of concepts and for the provision of background material, this thesis will discuss aspects of the laser propulsion system outside of the aerodynamic realm, but by no means should it be construed that this thesis describes the entire system.

The heart of the two pulse system is the LSD wave: it is the mechanism by which laser energy from a remote source can be used to superheat a gas. Successful initiation and propagation of the LSD wave is a make-or break issue for the two pulse scheme. This thesis presupposes that the technical difficulties encountered in creating an efficient LSD wave can be solved. At the present time, the candidate

propellant Lithium Hydride has shown promise in the laboratory. The ablation process is straightforward in comparison. The absorption takes place at the surface, and the ablation laser flux need not be nearly so great as that required to sustain an LSD. Careful tailoring of the ablation pulse can be used to create favorable conditions for the LSD wave.

The LSD wave propagates due to absorption by Inverse Brehmstrahlung. (Figure 1.5). This is absorption of a photon by a free electron in the presence of an ion or neutral particle which acts as a collision partner. The collision partner is required to conserve momentum, since the photon is annihilated. Ion-electron interactions have a much higher absorption cross section than neutral-electron collisions, but at low degrees of ionization these ion-electron collisions are rare, so it is difficult to initiate an LSD wave in a cold gas. Assuming a plane wave of radiation incident on a uniform gas with fixed γ, Razier assumed that all of the absorption took place in a thin layer which made the flow analogous to a chemical detonation. Using a Chapman-Jouget analysis, which yields the minimum possible detonation speed consistent with the conservation equations and an exit boundary condition of sonic flow in wave fixed coordinates[11], he then provided a formula for the speed of the detonation front, which agreed with experiment.

$$D = \left[2(\gamma^2 - 1)\frac{\Phi}{\rho_0} \right]^{\frac{1}{3}}$$
(1.2.1)

Where

D=LSD Wave Speed

$\Phi=$ Main Pulse Laser Flux

$\rho_0=$density of unprocessed gas

For aerodynamic purposes it is often sufficient to assume that the absorption wave

8

is infinitely thin. For the Lithium Hydride LSD wave studied by PSI, the distance from the absorption front to the CJ point is 0.1 cm. The rapidly propagating wave front induces a velocity behind it, which decays to zero by a rarefaction wave. Thus, relative to the base surface, the velocity of the gas increases from zero at the base to its maximum value just behind the wave front. (Figure 1.6)

Following the initiation and propagation of the LSD wave, the laser is turned off and the blast phase begins. During this time the cloud of hot gas created by the LSD expands and cools. During the expansion, a substantial amount of additional impulse is transmitted to the vehicle. Blast flow which is not aligned with the thrust vector generates no thrust due to expansion, its kinetic energy is therefore lost. The more one dimensional the flow is, the greater the impulse transmitted to the vehicle. The flow situation can remain largely one dimensional or it can become fully three dimensional in short order, depending on the relationship between the laser spot diameter and the distance propagated by the LSD wave. Forming a dimensionless Aspect Ratio, A from these,

$$A = \frac{\text{LASER SPOT DIAMETER}}{\text{LSD PROPAGATION DISTANCE}} \qquad (1.2.2)$$

we have a parameter which conveniently describes the one-dimensionality of the flow. For $A < 1$ the flow is fully three dimensional, and for $A > 100$, the flow is essentially one dimensional.

An ideal gas analysis in one dimension using the method of characteristics by AVCO[12] and duplicated by the author finds that the total impulse received by a 1-D thruster due to detonation and blast into a vacuum is 9.5 times that received during just the detonation phase. Starting at t=0 when the main pulse begins, Table 2 constructed from these results shows the motivation for a detailed study of

9

the blast phase. The details of this code will be discussed in chapter 2, where it is used together with some simplifying assumptions to estimate 3-D losses.

To calculate the thrust received as realistically as possible, computational simulation of the Euler equations is undertaken in chapter 3. Here, existing algorithms, such as the Flux-Splitting procedure of Steger and Warming have been used, with new boundary conditions, shock-handling procedures, and specialized grids. Overall, these simulations describe the blast wave following the LSD wave over the vehicle configurations and into the near vacuum ambient conditions expected in space flight. The accuracy of these algorithms is also studied, classically and empirically.

Historically, these CFD efforts were motivated by the need to describe the flow over small vehicles, and by the presently compelling need to scale up experimental data (Figure 1.7). In these regimes, very few simplifying assumptions about the three-dimensionality of the flow can be successfully argued for. Only direct simulation can provide the answers to such questions as:

1. In the laboratory, if one doubles the laser spot diameter, holding all other parameters constant, what is the expected increase in impulse?

2. Is a large beam diameter even necessary? How good is thrust performance when the Aspect Ratio is 10?

3. A containment skirt or nozzle will add complexity to the design, but improve system performance. By how much?

4. What role do real-gas effects play in the blast wave?

The fundamental problem attacked in this thesis is to describe the three dimensional flow situation in the blast wave phase of a two pulse laser thruster. This accomplished, the thrust efficiency of a vehicle or experimental apparatus may be computed. And, as part of a team of investigators led by LLNL working on the

10

problem, the research documented here aims to be compatible with and supportive of the work done by our colleagues. From an academic standpoint, capturing the flowfield has required the development of techniques that were not available at the initiation this research. These techniques are applicable to the general area of detonation and shock dynamics.

Table 2:   **Summary of Detonation and Blast Impulse Development**

for a 1-D Thruster with Vacuum Ambient Conditions

Flow Timescales	Normalized Impulse	Percent of Max
0	0	0
1	1.0	11
10	5.9	62
100	7.9	83
1000	8.8	93
10000	9.5	100

Code: AVCO.BAS, a method of characteristics expansion code based on the work of ref [12]. Assumptions: $\gamma = 1.2$, 1-D flow. I_{max} corresponds to the 10000 timescale value of the impulse. The theoretical maximum normalized impulse reported in [12] is 9.86, but the solution is stopped at 10,000 timescales for practicality. The detonation period extends from 0 to 1 time scale, at which time the blast begins. The timescale of the flow is defined as:

$$\tau \equiv \text{FlowTimescale} = \text{Main Pulse Laser on Time.}$$

The Impulse is normalized against the detonation value:

$$f \equiv \text{Normalized Impulse} = \frac{\text{Total Impulse Received}}{\text{Impulse Received During Detonation}}$$

Chapter Two

Models and Solutions Using the Method of Characteristics

Part 1: Discussion of the Method of Characteristics

Prior to employing CFD to solve the problem of predicting the thrust efficiency of a laser propelled rocket, a solution using the 1-D method of characteristics (MOC) and a worst case assumption for the lateral expansion of thrust gases was deemed worthwhile. Together with the reliability of the method of characteristics, the conservative assumptions used make these calculations a lower bound calculation of the thrust efficiency. While computational methods are necessary for small aspect ratios, these MOC solutions provide the answer for large aspect ratios, where the use of compuational methods is expensive and unnecessary. The final curve of thrust efficiency versus aspect ratio is then constructed from a combination of these two methods.

A second use of these MOC solutions is as a boundary condition in the space-time of the axisymmetric non-steady simulations run on a computer. Since there is a 1-D solution in part of the flow, called the 1-D core (Figure 2.1), the most accurate technique possible is used to calculate it. This reduces numerical error.

The 1-D solution is plotted on an x-t diagram. The flow is assumed to be an ideal gas which is isentropic behind the detonation wave, with $\gamma = 1.2$ The solution for the entire 1-D field is given by the Riemann Invariants,

$$J^+ = u + \frac{2c}{\gamma - 1}$$

$$J^- = u - \frac{2c}{\gamma - 1} \tag{2.1.1}$$

It can be shown that the non-steady isentropic Euler equations, which are partial

differential equations [13],

$$U_t + F_x = 0 \qquad (2.1.2)$$

in which

$$U = \begin{bmatrix} \rho \\ \rho u \\ e \end{bmatrix} \qquad (2.1.2)$$

$$F = \begin{bmatrix} \rho u \\ \rho u^2 + p \\ (e + p)u \end{bmatrix} \qquad (2.1.3)$$

become simple ordinary differntial equations along the characteristics dx/dt=u+c and dx/dt=u-c. First, the 1-D Euler set of P.D.E.'s is rephrased in terms of the Riemann Invariants:

$$\frac{\partial J^+}{\partial t} + (u + c)\frac{\partial J^+}{\partial x} = 0$$

$$\frac{\partial J^-}{\partial t} + (u - c)\frac{\partial J^-}{\partial x} = 0 \qquad (2.1.4)$$

Next, with $\vec{e}_0 = (1, 0)$ the unit time vector, and $\vec{e}_1 = (0, 1)$ the unit x vector, we introduce the vectors $\vec{\eta}$ and $\vec{\xi}$ which are suggested by eq.(2.1.4)

$$\vec{\eta} = (1, u + c) \qquad \vec{\xi} = (1, u - c) \qquad (2.1.5)$$

Since by definition the gradient of a function f in the (t,x) coordinate system is

$$\nabla f = \frac{\partial f}{\partial t}\vec{e}_0 + \frac{\partial f}{\partial x}\vec{e}_1$$

The equations (2.1.4) for the Riemann invariants become

$$\nabla J^+ \cdot \vec{\eta} \equiv \frac{dJ^+}{d\vec{\eta}} = 0$$

$$\nabla J^- \cdot \vec{\xi} \equiv \frac{dJ^-}{d\vec{\xi}} = 0 \qquad - \qquad (2.1.6)$$

14

The zeroes on the RHS of these equations make them exceptionally easy to solve. Along paths in (t,x) space parameterized by a varaible λ

$$(t, x) = (t_0, x_0) + \lambda \vec{\eta}$$

we have $J^+ = $ const, while along the alternative paths parameterized by μ

$$(t, x) = (t_0, x_0) + \mu \vec{\xi}$$

we have $J^- = $ const. In ref[12] the terminology used is different; $P \equiv J^+$ while $Q \equiv -J^-$. The advantage of this type of notation is that the numbers P,Q are always> 0, which makes visualization of the solution somewhat easier. The general procedure for solution of the 1-D nonsteady isentropic flow following the detonation wave is:

Beginning with the initial and boundary conditions for the problem, the solution is constructed by tracing rays of constant P and rays of constant Q until they reach another ray or a boundary, at which a new ray trajectory is calculated using this new data. The solution is complete when at each point in (t,x) space, a value for P and Q have been specified. To illustrate, the solution for the centered rarefaction wave is shown in Figure 2.2. This flow, treated in ref[14], is simpler than the laser propulsion flow, and more familiar.

Part 2: Coordinate System for Pulsed Laser Propulsion

It is appropriate for this problem to work in non-dimensional quantities. System parameters, such as the detonation speed of the LSD wave, are subject to change as laser power is improved and other propellants are tried. Thus, to create results which are applicable to a wide range of cases, non-dimensional quantities are used wherever possible. To obtain results in SI units, conversion calculations are made at the end of a computer run. For the double pulsed laser propulsion system, the reference parameters are shown in Table 3. In general the ablated gas density is in the range of 0.1 kg/m^3 and the main pulse laser flux for a CO_2 laser driven system is approximately 10^7 W/cm^2 = 10^{11} W/m^2. For the propellenat Lithium Hydride, the expected values of pressure and density behind the LSD wave are substantially less than the reference values. While these quantities are combinations of the more fundamental units of mass, length and time, they are listed for convenience.

Table 3: Reference Quantities used in Non-Dimensionalizations

Quantity	Name	Reference Value
Time	τ	$1\mu sec = 10^{-6}$ sec
Speed	D	10 km/sec = 10,000m/sec
Length	$D\tau$	1cm = 0.01m
Density	ρ_{ref}	1 kg/m^3
Pressure	$p_{ref} = \rho_{ref}D^2$	100 MPa = 990 atm
Energy Density	$e_{ref} = p_{ref}$	
Laser Flux	Φ	10^7 W/cm^2

Space and time values in the solution are nondimensionalized by the reference

length, and time via

$$X = \frac{x}{D\tau}$$
$$T = \frac{t}{\tau}$$

(2.2.1)

The Euler Equations, prior to solution, are non-dimensionalized by multiplying the entire equation by the diagonal matrix **N** and by converting the differentiation to non-dimensional form. The calculation will be illustrated for the 1-dimensional case for simplicity; the higher dimensional cases for 2-D and axisymmetric flow are similar.

$$\mathbf{N} = \ diag \ \left(\ \frac{1}{\rho_{ref}}, \ \frac{1}{\rho_{ref}D}, \ \frac{1}{e_{ref}} \ \right)$$
$$\frac{\partial}{\partial t} = \frac{1}{\tau}\frac{\partial}{\partial T}$$
$$\frac{\partial}{\partial x} = \frac{1}{\tau}\frac{\partial}{\partial X}$$

(2.2.2)

We begin with the 1-D Euler set :

$$U_t \ + \ F_x = 0$$

(2.2.3)

Converting the time and space differences, we have:

$$\frac{1}{\tau}U_T \ + \frac{1}{D\tau}F_X = 0$$

(2.2.4)

Defining F' via $F' \equiv F/D$, We have that F' has the same dimensions as U, and so we combine F' into (2.2.4) and post-multiply the entire equation by N to get:

$$\mathbf{N}\left[\frac{1}{\tau}U_T \ + \frac{1}{\tau}F'_X\right] = 0$$

(2.2.5)

Thus the entire set of Euler equations is non dimensionalized, yielding the form:

$$\tilde{U} \equiv \mathbf{N}U$$

$$\tilde{F} \equiv \mathbf{N}F'$$

(2.2.6)

$$\tilde{U}_T + \tilde{F}_X = 0$$

17

Henceforth, all gas-dynamic calculations performed in this thesis are dimensionless, unless otherwise stated. The results will scale with the appropriate reference quantities. Again, the objective is to provide results which easily scale with the characteristics of the thruster, and the aspect ratio defined in (1.2.2) is the primary scale factor. One of the principal reasons for carrying out these calculations is numerical. Evaluating the matrix N using the SI values in Table 3 yields an eight order of magnitude differerential in the quantities in the state vector.

$$N = diag(\ 1\ \frac{m^3}{kg},\ 10^{-4}\ \frac{m^2 s}{kg},\ 10^{-8}\ \frac{m^2}{N}\ ) \qquad (2.2.7)$$

And since the flux vector is non-dimensionalized by N/D, the span of numbers covers machine 0 to 10^{12}. Machine representation of such a large span of numbers is straight forward on a CRAY computer; the large word size of these machines necessitates that only single precision be used. But on smaller computers such as the 32 bit VAX and the 16 bit and 32 bit PC's where some of the computer codes in this thesis were built, it was found that single precision was best used only after the non-dimensionalizing. Numerically, then non-dimensioanalization was used to safeguard the use of single precision arithmetic in order to speed up codes and to avoid the memory penalty inherent in using double precision.

Part 3: Self Similar 1-D Detonation Wave

This analysis assumes that the detonation front is negligibly thin. The ambient conditions are assumed to be a still gas slug recently evaporated by the ablation pulse. Ablation analysis in [12] shows this to be an acceptable idea. The classical problem [15] of detonations consists of:

1.) Determination of the Detonation Speed, and

2.) Determination of the Flow Induced by the Detonation.

1. Determining the Detonation Wave Speed

This is known simply as *the D Problem* . For an LSD wave propagating into a uniform slab of ideal, fixed γ gas of density ρ_0 under a flux Φ, the detonation speed D is

$$D = \left[2(\gamma^2 - 1)\frac{\Phi}{\rho_0}\right]^{\frac{1}{3}} \tag{2.3.1}$$

This is occasionally called the Razier speed, in recognition of the Soviet physicist who calculated it; and it assumes that the laser flux is completely absorbed due to inverse Brehmstrahlung. This saturates the flow with energy, and so the heat added is a maximum, for a given speed of detonation. The jump relations across the wave are therefore Chapman-Jouget relations. The density jump is

$$\rho_{CJ} = \rho_0 \frac{\gamma + 1}{\gamma} \tag{2.3.2}$$

and the pressure jump is

$$p_{CJ} = \frac{\rho_0 D^2}{\gamma + 1}. \tag{2.3.3}$$

Because they are useful for constructing the Riemann invariants, the velocity and speed of sound behind the wave front are given:

$$u_{CJ} = \frac{D}{\gamma + 1}$$
$$c_{CJ} = \frac{\gamma D}{\gamma + 1}$$

$$(2.3.4)$$

Note that $u_{CJ} + c_{CJ} = D$, so the detonation wave front moves at the correct characteristic speed.

2. Determining the Flowfield Induced Behind the Wave

This is classically known as *the Piston Problem* . An isentropic rarefaction wave follows the detonation wave. The two problems are coupled. Solution is achieved in x-t space via a similarity transformation to the variable x/t, and is sometimes called the Taylor wave, after G.I. Taylor, who solved the problem for plane and spherical symmetry.

For an LSD wave thruster, the solution is constructed using the Riemann invariants in the normalized x-t space X-T, with X and T given by (2.2.1). Behind the detonation, the value of the Riemann invariants $P = J^+$ and $Q = -J^-$ are found from the jump conditions.

$$P_{CJ} = \frac{D}{\gamma + 1} \left[\frac{3\gamma - 1}{\gamma - 1} \right]$$
$$Q_{CJ} = \frac{D}{\gamma - 1}$$

$$(2.3.5)$$

For $\gamma = 1.2$, $P_{CJ} = 5.909\, D$ and $Q_{CJ} = 5\, D$. The P invariants are fixed on characteristic rays emanating from the origin with slope $X/T = (u+c)/D$. Throughout the rarefaction, Q remains a constant at its wave front value. This system has a piston speed of 0, corresponding to a hard wall boundary condition. At the hard

20

wall (w), the velocity is 0 and Q is constant, so:

$$Q_w = \frac{D}{\gamma - 1}$$

$$u_w = 0$$

$$P_w = Q_w$$

$$c_w = \frac{1}{2}(\gamma - 1)Q_w = D/2$$

(2.3.6)

The u+c characteristic slope for the P invariant at the wall is $c_w = D/2$, so a constant state region of zero velocity is described by:

$$u = 0, \ c = D/2 \quad : \quad 0 \le \frac{X}{T} \le \frac{D}{2}$$

(2.3.7)

The change of P is linear in the fan between the still region and the wave front, giving rise to ramp shaped velocity and speed of sound profiles there. Introducing the slope variable $\zeta = X/T$, the entire self-similar solution is established (Figure 2.3) For $0 \le \zeta \le 1/2$ equation (2.3.7) applies, while for $1/2 < \zeta \le 1$ we have

$$u = \frac{2D}{\gamma + 1}(\zeta - 1/2)$$

$$c = D/2 + \frac{(\gamma - 1)D}{\gamma + 1}(\zeta - 1/2)$$

(2.3.8)

Part 4. 3-D Efficiency Calculations–The Worst Case

As planned, the two pulse thruster will rely on a plane wave of incident laser light to initiate and propagate the LSD wave. On the beam centerline, the core of the flow will remain one dimensional until a rarefaction wave from the edge of the thruster reaches the centerline. Consider a circular thruster, as shown in Figure 2.1. As the LSD and later its blast wave propagates off the thruster surface, a shrinking volume of one dimensional flow is found in the center. Interior to a circle moving inward at the local speed of sound that begins on the outer diameter of the thruster, the base pressure is given by the 1-D pressure. Outside this horizon, the pressure is actually some function of the radius, which is conservatively assumed to be zero. With an initial laser spot radius of R_0, the core is the region interior to R_{core}, given by

$$R_{core}(T) = R_0 - \int_{T_0}^{T} c_{core}(t)dt \qquad (2.4.1)$$

And the worst case pressure is given by:

$$p(r,t) = \begin{cases} p(0,t), & 0 \leq r \leq R_{core}; \\ 0, & r > R_{core}. \end{cases} \qquad (2.4.2)$$

The Impulse transmitted to the vehicle is the product of force and time, expressed by the integral

$$I = \int_0^{\infty} \int_0^{R_{max}} p(r,t) \; r \; dr \; dt \qquad (2.4.3)$$

At any time the accrued impulse is given by

$$I(t) = \int_0^{t} \int_0^{R_{max}} p(r,t') \; r \; dr \; dt' \qquad (2.4.4)$$

The Blast contribution to the total impulse transmitted to the vehicle is substantial. Normalizing the impulse against the impulse received during the detonation phase,

at the end of which $t = \tau$ produces a measure of this. Using the same notation as [12], we define f as the normalized impulse

$$f(t) = \frac{I(t)}{I(\tau)} \qquad (2.4.5)$$

Using dimensionless time, this equation is simply $f(T) = I(T)/I(1)$.

The 3-D thruster efficiency η_{3D} is a comparison of the impulse received by the 3-D vehicle with a 1-D vehicle which has the same area.

$$\eta_{3D} = \lim_{t \to \infty} \frac{f(t)_{3D}}{f(t)_{1D}} \qquad (2.4.6)$$

The reference one-dimensional $\gamma = 1.2$ thruster yields a normalized impulse of 9.5 after 10000 laser time scales according to Table 2. Truncation of the limiting process at 10000 τ is due to the fact that almost no additional impulse is acquired after f=9.5. The theoretical maximum for f is 9.86; however, the more pracitcal figure is 9.5. For a 1 microsecond main laser pulse, duty cycled at 100 Hertz, there are 10,000 τ in between main pulses.

The tool developed to implement these calculations is the code AVCO.BAS, written in 1987 for the Microsoft Quick Basic Compiler. It was named after the original AVCO team that first performed the 1-D calculation. By performing base pressure integration using the worst case assumption in eq. (2.4.2), the code AVCO3D.BAS extends the 1-D thruster analysis to an axisymmetric thruster. From the 1-D code, plots of base pressure versus time and impulse development versus time are given in Figures 2.4 and 2.5. These curves assume importance later, when computational fluid dynamics is used to simulate the flow, because the 1-D thruster provides the upper bound for performance.

Figure 2.6 depicts the 3-D efficiency versus the aspect ratio, under the simplifying worst case assumption for the base pressure profile. The worst case assumption is

23

extremely conservative, as shown in Figure 2.6 and listed in Table 3. For a circular thruster, a great deal of thruster area is found near the edge, and so integration of the decaying pressure profile outside the 1-D core flow region is required for a realistic estimate. Accurate efficiency calculations for the aspect ratio range $2 < A < 40$ cannot be made with the worst case assumption, but as expected the curve shows improved performance with vehicle size.

While calculation of the pressure in this outer flow region $r > R_{core}(t)$ via an application of the method of characteristics in (z,r,t) space might be achieved if the target surface remained a hard wall for all values of r, the vehicle is expected to be a cone or cylinder which has a base that extends only to the point R_{max}. And, while the MOC has proven to be a valuable technique in two independent variables for calculating gas flows, it is nowhere near as simple in three independent variables. Characteristic rays, along which the solution is constant in (x,t) space, become conical surfaces in such a space as (z,r,t), and this difference makes implementation in higher dimensions quite complex. In addition, the cylindrical geometry introduces source terms into the Euler equations, yielding characteristic equations which have a non-zero right hand side with the differential operator on the LHS. This means that along characteristic trajectories the solution is not constant but obeys an ODE. In cases where the expansion of a gas into vacuum has a greater degree of symmetry than in the case of laser propulsion, ODE's have been formulated and solved by quadrature. G.I. Taylor [17] and even recently, Schmaltz[16] have attcked and solved this type of problem. One such case would be the expansion of gas from a line source into vacuum in cylindrical coordinates, which has no analog in laser propulsion. Given these restrictions on the use of the method of characteristics for higher dimensional work, and the availability of good numerical methods for the Euler equations, 3-D calculations of the flow are best done using CFD.

Table 4: Axially Symmetric Expansion Effects, Worst Case Scenario.

A	$f(T_{max})$	η_{3D} (%)
10	2.05	21.7
20	3.93	41.6
30	4.90	51.8
40	5.50	58.2
50	5.93	62.7
60	6.25	66.1
70	6.50	68.7
80	6.71	70.9
90	6.88	72.7
100	7.03	74.3
120	7.46	78.8
160	7.62	80.5
200	7.86	83.0
250	8.08	85.4
300	8.25	87.1
350	8.49	89.7
450	8.58	90.7
500	8.66	91.5

Solution Advanced to $T_{max} = 10,000\tau$ upon which propulsive efficiency is based. Fluid is an ideal gas with $\gamma = 1.2$ A = Aspect Ratio, defined in (1.2.2), and η_{3D} is defined in (2.4.6).

Chapter Three

Part 1: Blast Flow Situation and Equations of Motion Used

By solving the initial-boundary value problem of a blast wave propagating off the base of a cone, the thrust received by the cone is found. The most likely candidate shape for a vehicle is a cone, with propellant covering its base. Because the flow behind the LSD wave has a known solution, these simulations begin just as the main pulse from the laser is turned off. The 1-D method of characteristics solution for the flow in the rear of the LSD wave is used as the initial condition for the blast. Edge effects during detonation are ignored. The total thrust transmitted to the vehicle is then computed by adding the blast impulse to the detonation wave impulse.

The cone is an axisymmetric body, and the flow is non-steady. Convection dominates this flow. Viscous momentum transport, heat conduction, and heat transport by radiation are shown to be small contributors to the solution and are ignored. The gas is assumed to be ideal, with a $\gamma = 1.2$ This γ is shown to be a good choice for Lithium Hydride in the Laser Propulsion regime. Thus, the equations of motion of the fluid to be solved are:

$$
\begin{bmatrix} \rho \\ \rho u \\ \rho v \\ e \end{bmatrix}_t + \begin{bmatrix} \rho u \\ \rho u^2 + p \\ \rho u v \\ (e+p)u \end{bmatrix}_z \begin{bmatrix} \rho v \\ \rho u v \\ \rho v^2 + p \\ (e+p)v \end{bmatrix}_r = -\frac{v}{r} \begin{bmatrix} \rho \\ \rho u \\ \rho v \\ (e+p) \end{bmatrix} \tag{3.1.1}
$$

The following calculations and data are included to show that the flow is governed primarily by the inviscid Euler equations. Of prime importance is the time-scale of the flow, on the order of microseconds. Often, there simply is not sufficient time for other mechanisms to act in the presence of such large convection. The gas used in the calculations is equilibrium LiH, at a density of 0.05 kg/m^3 and a temperature

of $8000 K$ – conditions expected in the region immediately behind the LSD wave at the base of the thruster. The gas is shown to be a continuum. Items of interest are documented below and are: 1. Number Density, 2. Radiation, 3. Viscosity and Heat Conduction. The equilibrium properties of LiH are computed using the thermodynamic code of Gordon and McBride[18].

1. Number Density

At the density and temperature given above, we find:

$$n = 8.73 \times 10^{24} \ m^{-3} \tag{3.1.2}$$

This number density is 35% of that for air at STP, which has a number density of $2.54 \times 10^{25} \ m^{-3}$ and so diffusive transport is ignored. The gas is considered to be uniform in its elemental composition. At the expansion wave front, the density is much less, and so this assumption breaks down. However, the flow there is supersonic and information of this will not get back to the base, where the flow is subsonic. The flow will be ionized, but charge neutrality and translational equilibrium of the electrons is assumed on the basis of the high number density of propellant gases. The mean free path of the gas atoms, λ is computed with the atoms assumed to have a 4 Angstrom diameter, yielding a collision cross section $\sigma = \pi d^2$ and the result for λ is:

$$\lambda = \frac{1}{\sqrt{2} n \sigma} \tag{3.1.3}$$

From the values given, we have $\sigma = 5.02 \times 10^{-19} \ m^2$ and $\lambda = 1.61 \times 10^{-7} \ m = 1.61 \times 10^{-5} \ cm$. Thus, even when expanded by a factor of 50 the base gas has a mean free path of $8.05 \times 10^{-4} \ cm$. This path length is far smaller than the length scales of the vehicle and flowfield around it. With L the length of travel of the LSD wave specified to be $1 \ cm$ The Knudsen number, $Kn = \frac{\lambda}{L}$ is thus approximately 10^{-4} and so the gas is governed by the equations of motion for a continuous fluid.

2. Radiation

In LSD calculations performed on ablated Aluminum in air, Jumper et. al.[19] found radiation losses to be small. The energy and time scales used in their simulations were similar to those expected in Laser Propulsion. However, Aluminum has a higher molecular weight than Lithium Hydride, so the temperatures achieved are about twice that for an LiH system–$20,000K$ for Aluminum and $10,000K$ for LiH. Before going further, a comparison of the system parameters used in their Aluminum simulations with the candidate LiH Laser Propulsion (LP) system is made. Table 5 shows the similarity between the two flow situations.

Table 5: System Parameters for Aluminum LSD calculations in Air and the Two Pulse LiH Laser Thruster

System Parameters	Jumper et. al	2 pulse LP
Laser Flux	$10^7 \ W/cm^2$	$10^7 \ W/cm^2$
Laser on Time	$10\mu sec$	$1\mu sec$
Material	Aluminum	LiH
Max Temperature	$20,000K$	$10,000K$
Beam Diameter	$1 \ cm$	$10cm+$
Beam Profile	Gaussian	Square
Early Flow Situation	2-D axisym.	2-D axisym.
Ambient Medium	Air, 1 atm	None
Energy Fluence	$17 \ J/cm^2$	$10 \ J/cm^2$

These investigators were concerned with re-radiation of thermal energy in the LSD to the target surface. For optically thin calculations, where the product of the absorption coefficient and the distance travelled is considered small, they report re-radiative heating of the surface of less than 1% of the laser energy fluence. For optically thick calculations, where the gas is assumed to behave like a blackbody

with an emissivity of $\epsilon = .18$, the target receives less than 3% of the laser fluence by re-radiation of gas energy. In the Laser Propulsion system, we are concerned with the total loss of propellant energy, and so we must account for energy radiated out the sides and front of the wave as well as that radiated to the surface. Except for flows with a small aspect ratio, the frontal area of the beam will far exceed the area to which radiation may escape to the side of the thruster. Thus a 10% loss of propellant energy due to radiation would be highly conservative.

In order to better estimate radiative losses for a laser propelled vehicle, the 1-D expansion code *AVCO.BAS* was modified. The resulting code, *RAD.BAS* calculates blackbody radiation for a 1-D thruster, The radiation is assumed to be one-dimensional, and not coupled to the gas-dynamics of the expansion. The system is diagramed in Figure 3.1, and its

---

Table 6: RAD.BAS Initial Conditions and System Parameters

Laser Flux	$\Phi = 10^7 \ W/cm^2$
Pulse Duration	$\tau = 1\mu sec$
Fluence	$10 \ J/cm^2$
Detonation Speed	$D = 8.5 \ km/sec$
Initial Base Temp.	$10,000 K$
Gas	Ideal, $\gamma = 1.2$
Gas Emissivity	$\epsilon = 0.18$

---

parameters are listed in Table 6. The gas slab behind the LSD wave quickly achieves a constant state in a region near the base. Most of the propellant is in this region, and it is assumed to radiate at the base temperature, which is plotted in Figure 3.2a. In addition, Figures 3.2b and 3.3 report the thermal radiative flux at the base and the integrated energy loss. At the base the radiation is thus assumed to be governed by the optically thick assumption. There, the solution is truncated at 100

timescales into the flow, at which time the gas temperature at the base is $4076K$ and the gas is assumed to be non- radiating.

Forward radiative losses are more difficult to predict. If the optically thick assumption is held, very rapidly the forward radiation will drop to near zero. This is because the gas cools at it expands, and the leading edge of the expanding propellant is a cold, high speed flow. The base condition is that of a still, high temperature gas. Some of the radiation from the base region will escape through the propellant, and so the forward condition is established as follows: For the first 20 time scales, the forward radiation will be equal to the radiation to the base– afterward it is zero. This condition is an estimate. Using these two conditions, the overall losses are calculated to be less than 2.5% of the laser energy input. If more extreme forward boundary conditions are used, the overall energy loss will be less than 5% of the total laser energy input. In either case, the role of radiation losses is minor. For all radiative flux calculations, the equation used is the Stephan-Boltzman Law:

$$q_{rad} = \epsilon \sigma T^4 \tag{3.1.4}$$

Small aspect ratio thrusters will lose a substantial amount of energy to the sides by radiation, and so the 2.5% loss for the 1-D system will be higher; a figure of 10% would be a safe upper bound for systems in the range $2 \leq A \leq 8$.

3. Viscosity and Heat Conduction

3A. Reynolds Number

The Reynolds Number is a standard estimate of the ratio of inertial to viscous forces:

$$Re = \frac{\rho U L}{\mu} \qquad - \tag{3.1.5}$$

30

Here U is the flow speed, and L is the characteristic length of the system with ρ and μ the density and viscosity. The difficulty lies in choosing the parameters on which the Reynolds Number is based. Very soon after the laser is turned off, convective speeds equal to the LSD propagation speed are achieved, and in the expansion, the fluid density times the characteristic length remains roughly constant. So a good basis for the Reynolds number is the LSD wave. A value for Re of 59,150 has been found for a Lithium Hydride thruster, and will be documented in Table 7.

Table 7: Reynolds Number Calculation

Density	$\rho = 5 \times 10^{-2} \ kg/m^3$
Temperature	$T = 8000K$
Velocity	$U = D = 10 \ km/s$
Time Scale	$\tau = 1 \ \mu sec$
Length Scale	$L = D\tau = .01 \ m$
Viscosity	$\mu = 8.45 \times 10^{-5} Ns/m^2$
Result	$Re = \frac{\rho U L}{\mu} = 59,150$

3B. Parametric Calculation of the Energy Flux due to Conduction

Without going into great detail the heat flux can be estimated parametrically as the thermal boundary layer thickness is varied. Here, the flow of heat from the propellant to the base q is assumed to obey the Fourier Law:

$$q = -k\frac{dT}{dx} \tag{3.1.6}$$

where k is the thermal conductivity. The heat flux will be assumed to be within a thermal boundary layer at the interface between the gaseous propellant and the unevaporated propellant. The change of temperature will be assumed to be $\Delta T = 8000K$ With Δx the parametric variable, we have

$$q \approx k\frac{\Delta T}{\Delta x} \tag{3.1.7}$$

31

For Lithium hydride, the value of k at $8000K$ will be used: $k = 1.118$ W/(m K) The results are listed in Table 8 and show that the thermal boundary layer must be very thin, on the order of $0.01cm$ in order to have heat conduction play a major role in the flow.

Table 8: Parametric Calculation of the Heat Flux By Conduction

$\Delta x \ (m)$	$q \ (W/m^2)$	q/Φ
10^{-2}	8.94×10^5	10^{-5}
10^{-3}	8.94×10^6	10^{-4}
10^{-4}	8.94×10^7	10^{-3}
10^{-5}	8.94×10^8	10^{-2}
10^{-6}	8.94×10^9	10^{-1}

Conclusions on Heat Conduction and Viscosity

1. Viscosity is not expected to slow down the expansion of gases for this model system along the thrust vector to any great degree. It will decelerate the lateral expansion of gas along the vehicle surface, but the main flow will not be greatly affected.

2. Temperature gradients at the base surface must be very large to allow for heat conduction to play a major role. The LSD wave is expected to be 0.1 cm thick, according to Physical Sciences Inc. A great change in temperature such as the 8000K used here is expected to require at least this much distance to be physically resolved. Under this assumption, the thermal boundary layer has a thickness not less than 0.1 cm and the heat flux by conduction to the wall is 10,000 times less than the laser flux. Even if the thermal boundary layer is .01 cm thick the heat flux at the surface will be 10^{-3} of the laser flux. Given that the vast majority

of impulse is acquired within 100 timescales, such a situation would result in the loss on the order of 10% of the propellant's energy by conduction, an appreciable amount but still leaving the inviscid, non-conducting Eulerian equations as a good approximation to the flow.

3. Temperature Gradients within the expansion are insufficient to allow conduction of heat to play a major role. Here, the thermal thickness is on the order of 1cm, and so the heat flux is $< 10^5$ of the Main Pulse Laser Flux.

4. To estimate the role of viscosity and heat conduction for Lithium Hydride propelled systems with different parameters, it is often only necessary to re-compute the Reynolds number. The Prandtl Number is .79 and so the viscous and thermal boundary layers will be comparably thick.

Final Notes

It must be stressed that these calculations are approximate and conservative because they assume a constant boundary layer thickness. The non-steady nature of this expanding flow will result in a thermal and viscous boundary layer whose thickness grows with time, and reduced shear and heat flux with time. One item which merits additional study is the high degree of ionization for the gas, which can yield electron mole fractions in excess of 10% – plasma conditions. The flow is assumed to be charge- neutral, operating in the presence of no appreciable electric or magnetic field during the blast. Under these assumptions, magnetohydrodynamic effects thus will not occur, and so in the mean the flow will be governed by the Euler equations. Still, the higher thermal speed of the electrons leads to problems not attacked here.

In addition, the problem of vapor recondensation is not attacked here, but is was suggested by Jumper et. al[19] to be a significant mechanism of heat transfer by the

hot gas in the LSD wave. The formation of the solid LiH form the gaseous phase is exothermic, and so some of the mass and energy of a given pulse may be lost due to surface recondensation.

Part 2: Numerical Method

Section 1. Challenge of Near Vacuum.

Modification of Steger and Warming 2nd Order Scheme.

The Euler equations are explicitly solved by finite differencing, using Steger and Warming's Flux-Splitting procedure[20]. The second order accurate predictor-corrector method is used on the points interior to the flow in conjunction with the first order accurate predictor at boundaries and across strong shocks.

A computational proceedure has been developed which searches for non-physical solutions by the second order scheme and substitutes in their place the more robust first order results. This is necessary for the near vacuum ambient conditions simulated for laser propulsion. Across strong shocks the second order scheme will produce numerical undershoots. These undershoots are catastrophic at the shock interface between the high pressure wave front and the near vacuum gas, because the undershoot predicts negative values for the density, pressure and internal energy.

Figure 2 of the Steger and Warming Paper shows a shock-tube density plot where the initial pressure ratio is 10:1. The numerical solution using the upwind 2nd order explicit scheme for the density undershoots the exact solution by an amount which is not catastrophic for that particular run. This undershoot rapidly would become catastrophic if the initial conditions were changed to a pressure ratio of 10,000:1 and a density ratio of 100:1, the type often used in the numerical work performed here. These conditions were found to be close enough to simulating a vacuum that pushing to greater pressure and density ratios was considered unnecessary. However, the algorithm has executed well at higher pressure ratios. The code *PROP.FOR*, which simulates the blast following an LSD wave, has been run with density ratio

35

of 100,000:1 and a pressure ratio of 10,000,000:1, where the ratios given relate the post LSD gas to the ambient gas. But it was found that the solution was virtually identical to runs performed with an energy ratio of 10,000:1 and a density ratio of 100:1, only more costly in terms of computer time.

Solutions of the simple wave equation in one dimension illustrate the point of a selective scheme, which is second order everywhere it can be and first order elsewhere. The first order solution is engaged only at boundaries, where the 2nd order terms cannot be constructed, and at the wave front where there is undershoot. Elsewhere the gradients are insufficient to result in any computational difficulty.

The equations,

$$U_t + F_x = 0 \quad , \quad F = U$$

are solved exactly by any function g in the variable $\eta = x - t$

$$U(x,t) = g(\eta)$$

and so waves propagate on lines x=t. Figure 3.4 illustrates the simulation of this equation by first, second, and modified second order schemes.

By running the second order scheme with no limiter at a Courant number of 1.0 or even at 2.0, the square wave remains perfectly square. The same result is achieved by running the first order scheme at a Courant number of 1.0. Such perfect numerical performance is not at present possible for the simulation of an axisymmetric blast wave. In the laser propulsion simulations, the solution varies spatially, but it is globally advanced by the same time step. Field points along the shock front will not all have the same jump magnitude and the time step will be shorter than necessary for some of these points, leading to the undershooting of the solution. And, in reality the fluxes of the Euler equations are non-linear functions unlike the

36

linear flux in the simple wave equation, so in computational work it was borne out that something had to be done at the shock front if the 2nd order scheme was to be used for these near vacuum computations.

It is important to state that solution of the linear wave equation is not the objective of the numerical method. However, solution of the linear wave equation shows the motivation for the development of a vacuum interface proceedure for the second order scheme. In fact, the non-linear Euler equations have self steepening mechanisms so that the dispersion of the solution by a first order upwind calculation remains finite in its extent. But global accuracy of a 2-D axisymmetric time accurate flow simulation virtually requires a second order scheme, as will be shown in section 5; and the vacuum ambient conditions necessitated the development of the vacuum interface proceedure.

Section 2. Finite Difference Technique.

The flux split proceedure, which is shown schematically in Table 9, will not be rigorously developed here. However, the concept of the method is simple. The fluxes of mass, momentum, and energy are split into forward winded components with positive characteristic speed and back winded components with negative charcteristic speed. In order to insure stable differencing, the forward winded components are differenced using the back difference operator, and vice versa, as shown in Figure 3.5. Essentially, the rationale of flux-splitting is that if material is blowing toward a point A, point A and a point upwind of A will form the correct flux difference. Downwind of A, whatever the flow is doing is "yesterday's news"–it is out of A's domain of dependence. The axisymmetric Euler equations are identical to the 2-D Euler equations with the exception of a source term which is due to the cylindrical geometry.

The predictor is first order accurate, and its results are stored for use at boundaries

37

Table 9: Steger & Warming 2nd Order Upwind Method

Definitions

$z_i = i\Delta z$

$r_j = j\Delta r$

Back Difference: $\nabla_z u_i = u_i - u_{i-1}$

Forward Difference: $\Delta_z u_i = u_{i+1} - u_i$

Second Back Difference: $\Delta_z^2 u_i = \Delta_z(\Delta_z u_i) = u_i - 2u_{i-1} + u_{i-2}$

Second Forward Difference: $\nabla_z^2 u_i = \nabla_z(\nabla_z u_i) = u_{i+2} - 2u_{i+1} + u_i$

Equation

$U_t + F_z + G_r = S(U, r)$

Predictor

$$U_{i,j}^{\overline{n+1}} = U_{i,j}^n + \Delta t S_{i,j}^n - \frac{\Delta t}{\Delta z}(\nabla_z F^+ + \Delta_z F^-)_{i,j}^n - \frac{\Delta t}{\Delta r}(\nabla_r G^+ + \Delta_r G^-)_{i,j}^n$$

Corrector

$$U_{i,j}^{n+1} = \frac{1}{2}\Big[U_{i,j}^n + U_{i,j}^{\overline{n+1}} + \Delta t S_{i,j}^{\overline{n+1}}$$

$$-\frac{\Delta t}{\Delta z}(\nabla_z F^+ + \Delta_z F^-)_{i,j}^{\overline{n+1}} - \frac{\Delta t}{\Delta r}(\nabla_r G^+ + \Delta_r G^-)_{i,j}^{\overline{n+1}}$$

$$+\frac{\Delta t}{\Delta z}(\Delta_z^2 F^- - \nabla_z^2 F^+)_{i,j}^n + \frac{\Delta t}{\Delta r}(\Delta_r^2 G^- - \nabla_r^2 G^+)_{i,j}^n \Big]$$

where the second order terms cannot be formed and where the shock interface causes the second order method to fail.

Section 3. Courant Condition.

The Courant condition insures numerical stability by insuring that the time step is short enough. Each field point is permitted to influence its nearest neighbors. Information in gas-dynamics is carried by waves, which have characteristic speeds. For the 1-D Euler equations, the wave speeds are u-c,u, and u+c. In 2-D and axisymmetric flow waves at the speeds v-c,v, and v+c carry information in the second dimension. In 1-D, the Courant Number is defined by

$$CN = Max(u - c, u, u + c)\frac{\Delta t}{\Delta x} \quad \leq \quad Max(|u| + c)\frac{\Delta t}{\Delta x} \qquad (3.2.1)$$

and so a Δt_C is found via the Courant condition from

$$\Delta t_c = \frac{CN\Delta x}{Max(|u| + c)} \qquad (3.2.2)$$

For most methods, $CN \leq 1$ insures stability in 1-D. Physically this means that a wave launched from a gridpoint i can influence only the points i-1 and/or i+1.

In two dimensions the time step is found by [21]:

$$\Delta t_c = \frac{CN}{Max\left[|u|/\Delta x + |v|/\Delta y + c\sqrt{1/\Delta x^2 + 1/\Delta y^2}\right]} \qquad (3.2.3)$$

For equispaced meshes, dx=dy, this becomes:

$$\Delta t_c = \frac{CN\Delta x}{Max\left[|u| + |v| + \sqrt{2}c\right]} \qquad (3.2.4)$$

Section 4. Axisymmetric Source Terms

When radial convection near the axis of symmetry is strong, the source term in the axisymmetric Euler equations (3.1.1) becomes large enough that it must be used to set the time step for the global advancement of the solution. The following is a

bounding calculation that is implemented in the code *PROP.FOR* and its descendants to handle large source terms, if necessary. Examination of the source term $S(U,r)$ in the axisymmetric Euler equations yields that the term is a scalar,$-v/r$, with the units of Time^{-1} multiplied by the vector shown below, which has the same dimensions as U.

$$S = -\frac{v}{r} \begin{bmatrix} \rho \\ \rho u \\ \rho v \\ e+p \end{bmatrix} \tag{3.2.5}$$

Since for an ideal gas $p = (\gamma - 1)[e - \frac{1}{2}\rho(u^2 + v^2)]$ we have that

$$e + p \leq \gamma e \tag{3.2.6}$$

We are concerned with the fractional change of the solution, which does not depend on the sign of the components of the U and S vectors. We take the absolute values of velocities, and define:

$$|U| = \begin{bmatrix} \rho \\ \rho|u| \\ \rho|v| \\ e \end{bmatrix} \tag{3.2.7}$$

Using the inequality above, the analogous term $|S|$ is bounded from above:

$$|S| = \frac{|v|}{r} \begin{bmatrix} \rho \\ \rho|u| \\ \rho|v| \\ e+p \end{bmatrix} \tag{3.2.8}$$

$$|S| \leq \gamma \frac{|v|}{r} |U| \tag{3.2.9}$$

The fractional change in solution due to the source term, defined by Q in the equation below, is bounded as well. Again using the absolute values of velocities, and the calling the change in the solution due to the source $\Delta|U|_s$, we have:

$$Q = \frac{\Delta|U|_s}{|U|} = \frac{|S|\Delta t}{|U|} \leq \gamma \frac{|v|\Delta t}{r} \qquad - \tag{3.2.10}$$

40

In practice, good solutions are achieved when the source terms are permitted to induce a change of no more than 5% ($Q = 0.05$) on the solution, however a 10% criterion ($Q = .1$) has been used as well without trouble when the radial flow is directed away from the axis of symmetry. In cases where the radial flow is converging on the axis of symmetry, such as in a cylindrical implosion, even the 5% criterion can be too dangerous because (-v/r) is a positive number tending to increase the magnitude of U. In general, the greater the amount of convection along the radial axis, the more conservative one has to be in specifying Q. Thus, after the Courant condition has been used to select a global time step, the source term is also checked to provide a safe time step, via

$$\Delta t_s = \frac{Q}{Max[\gamma|v|/r]} \tag{3.2.11}$$

The timestep used to advance the equations is then the minimum of the two.

$$\Delta t = Min(\Delta t_s, \Delta t_s) \tag{3.2.12}$$

Section 5: Convergence of Second Order Scheme

To show that second order accuracy leads to a solution which converges to the physical solution as grid resolution is increased, we begin with the Courant condition:

$$CN = \frac{\lambda_{max}\Delta t}{\Delta x} \leq 1 \qquad \Rightarrow \qquad \Delta t \propto \Delta x \tag{3.2.13}$$

where λ is the Euler eigenvalue. Because of the proportion $\Delta t \propto \Delta x$, the error in a method which is first order accurate in space and time will be proportional to Δt and for the general case of a method which is of order accuracy m in time and space, the error will be proportional to Δt^m.

41

In a computational simulation carried out to a time T with N iterations, with a constant time step, the time T is simply

$$T = N\Delta t \qquad (3.2.14.)$$

In reality, the time step in a changing solution changes as well, but for our purposes a constant time step is sufficient. If a global error ϵ is introduced in the solution with each time step, the error between the ideal solution and the compuational solution is

$$\frac{|U_{ideal}|}{|U_{computational}|} = 1 + \epsilon \qquad (3.2.15)$$

Let T be a constraint. If N iterations are performed in order to compute the solution at time T, we have, with $N \propto 1/\Delta t$

$$\frac{|U_{ideal}|}{|U_{computational}|} = (1 + \epsilon)^N \propto (1 + \epsilon)^{\frac{1}{\Delta t}} \qquad (3.2.16)$$

For the case of a second order method, $\epsilon \propto \Delta t^2$ and so a Taylor series expansion of the above equation yields

$$\frac{|U_{ideal}|}{|U_{computational}|} \approx 1 + N\epsilon \propto 1 + \frac{1}{\Delta t}\Delta t^2 = 1 + \Delta t \qquad (3.2.17)$$

Notice that a similar expansion for a first order method yields $N\epsilon$ of order unity, and so a first order simulation of a Courant condition limited problem will not converge as the grid spacing (and thus the time- step size) is reduced. Assuming that the orders of accuracy available for a simulation are 1,2,3,.., we have shown that second order accuracy is far more than aesthetically pleasing in a simulation; it is required for convergence.

Part 3: Choice of Grid. Preference of Equispaced Meshes for Time Accurate Problems.

The cone shaped vehicle for a laser thruster is principally determined by the mission requirements. The thruster surface should be flat, from which a plane LSD is launched. Illumination of the target surface must be achieved from a wide range of angles. And the payload must be protected from the laser beam and the outside environment in a housing which is aerodynamically and structurally efficient. A cone is a rational choice.

To perform simulations of the flow, which begins as an LSD wave close to the base of the cone surface and expands into the space around the cone, two grid strategies were devised. In the first strategy, a "C" type mesh was wrapped around the cone (Figure 3.6). The second strategy, which eventually won out, was to use two equispaced grids lined up with each cone face (Figure 3.7). Each technique has appeal. The "C" grid is a continuous mathematical object, easier to deal with than two discrete grids. The methodology for solving the Euler equations on the "C" grid already existed prior to undertaking this thesis, and without a doubt the "C" grid would yield decent results. However, the stretching of the "C" grid as it wrapped around the vehicle leads to some difficulties, particularly when the 2nd order upwind differencing scheme is used. While "C" type calculations need to carry a metric term with them, calculations on equispaced meshes do not. The zone of influence for a field point using the 2nd order upwind differencing scheme extends two points in all directions, that is, for a field point (i,j), the points $(i - 2, j), (i + 2, j), (i, j - 2),$ and $(i, j + 2)$ are all potential contributors to the solution. The spatially changing metric must be frozen at (i,j) for all of these contributors, leading to metric induced error.

Because the simulations are time-accurate, the acceptability of a curved mesh for

43

these calculations was deemed questionable. The dynamics of information travel on a mesh make it possible for information to travel between adjacent points. Curvature in the grid can lead to wavefront dispersion. For steady state calculations, transient errors of this type are not a problem since only the steady solution matters. For time-accurate problems, equispaced meshes offer a guaranteed convergence of the numerical approximations to the physical space-time problem being solved, whereas the issue is less clear for curved meshes. While a detailed investigation into this problem is not made here, the validity of this point is supported by a numerical investigation made and the results are shown in Figures 3.8 and 3.9. The problem is a two dimensional initial-boundary value problem for the Euler equations with identical initial and boundary conditions. A plane wave propagates through a square, equispaced mesh in the first case and through a curved mesh in the second. The wavefront is distorted into a curve by the curved grid.

Curved meshes are highly accurate where the density of grid points is made high, which is often advantageous. However, when the solution is being globally advanced by the same time step, and constrained by the Courant condition, high gridpoint density in a region can control the selection of timestep size. In the course of its evolution a flow may have high gradients in the densely covered region at one time and not another. During the period of high gradient in the dense grid region, the solution will be well captured there. Afterward, however, the high density of gridpoints in that region can become a global impediment. The high density of points yields small values for the time step size, potentially much smaller than is required elsewhere in the flow, where the action is.

For four reasons the approach taken here is to cover the cone with two equispaced meshes rather than one "C" type mesh. 1.) The extra computer memory and coding effort required in carrying around metric terms offers little advantage over connected

44

equispaced meshes, 2.) Metric error for second order difference approximations, and wave dispersion by grid curvature can reduce the accuracy of curved grids for time-accurate problems, and 3.) Satisfaction of the Courant condition in densely packed regions of the grid can yield time step sizes that are much more conservative than those required at other gridpoints, increasing the number of iterations required to run a solution out a specified length of time. Large numbers of iterations lead to a compounding of error in the solution. And 4.) The problem of solving for the flow over a corner using two grids intersecting at a sharp point rather than a "C" grid which smooths the corner would, if executed, offer greater aesthetic appeal.

Double Grid Plan for a Cone

For a 1-D non-steady problem the solution is given on an (x,t) or $(\mathbf{R}^1,t)$ diagram. Thus for an axisymmetric problem the space of the solution is $(\mathbf{R}^2,t)$. The region of $\mathbf{R}^2$ in which the flow takes place is called Ψ. It is covered by two rectangular regions, named Π and Λ , each covered by equispaced grids, shown in Figure 3.10.

$$\Psi = \Lambda \cup \Pi \qquad (3.3.1)$$

Inspection of the sets Π and Λ show that they overlap. The grids that cover them, however, are discrete sets and the best discrete overlap is achieved if the cone semi-vertex angle is 45 degrees. This is the cone angle used in all subsequent calculations, because it is simple to implement and a realistic estimate of the eventual vehicle design. The two grids are thus a discrete approximation to a connected region in $\mathbf{R}^2$.

The solution procedure for the Euler equations on these two grids is a patch of the solution on Π with the solution on Λ, running each as a 2-D Euler code in its own orthogonal equispaced coordinate system with a source term attached for axisymmetric effects. The initial condition is specified as a plane LSD wave within Λ. On the flat vehicle surfaces, the boundary conditions for the Euler equations

45

are straightforward. In the overlapping region, the field interior to the grid on II is used as a boundary condition for the grid covering Λ, and the field interior to the grid covering Λ is used as a boundary condition for the grid covering II. The coordinate systems used are different because they are aligned with the base of the cone in Λ and with the face of the cone in II. Transfer of scalars ρ, e is direct but the transfer of vectors $(\rho u, \rho v)$ requires a rotation from one coordinate system to the other. The exact overlap of discrete points between the two grids makes interpolation unnecessary for the vast majority of flow information transfers between the grids, however on one such surface, four field points in II are used to supply one point in Λ.

Equations of Motion, Transformations.

In region Λ, the coordinate basis for (z,r) space is $\vec{e_1}$, $\vec{e_2}$ as shown in Fig. 5. In region II the basis of the coordinates (x,y) is $\vec{e_1'}$, $\vec{e_2'}$ and is rotated 45° Counterclockwise with respect to basis for Λ. To establish a vector $\vec{A}$ in Λ as a vector $\vec{A'}$ in II, the transformation matrix $\mathbf{T}$ given below is used.

$$\vec{A'} = \mathbf{T}\vec{A} \qquad (3.3.2)$$

$$\mathbf{T} = \frac{1}{\sqrt{2}}\begin{bmatrix} 1 & 1 \\ -1 & 1 \end{bmatrix} \qquad (3.3.3)$$

The inverse mapping is the transpose of this orthoganal matrix, $\mathbf{T}^{-1} = \mathbf{T}^T$.

The equations of motion in Λ are the axisymmetric Euler Equations, which on the left hand side are the same as the 2-D Euler equations. The RHS of the 2-D Euler eq. is 0, while in the axisymmetric case a source term accounts for the increasing flow volume with radius. We have, in Λ:

$$\begin{bmatrix} \rho \\ \rho u \\ \rho v \\ e \end{bmatrix}_t + \begin{bmatrix} \rho u \\ \rho u^2 + p \\ \rho uv \\ (e+p)u \end{bmatrix}_z + \begin{bmatrix} \rho v \\ \rho uv \\ \rho v^2 + p \\ (e+p)v \end{bmatrix}_r = -\frac{v}{r}\begin{bmatrix} \rho \\ \rho u \\ \rho v \\ (e+p) \end{bmatrix} \qquad (3.3.4)$$

46

While in Π, with velocity vector $(\tilde{u}, \tilde{v})$ the equations are transformed to a 2-D set on the LHS with a different source term:

$$\begin{bmatrix} \rho \\ \rho\tilde{u} \\ \rho\tilde{v} \\ e \end{bmatrix}_t + \begin{bmatrix} \rho\tilde{u} \\ \rho\tilde{u}^2 + p \\ \rho\tilde{u}\tilde{v} \\ (e+p)\tilde{u} \end{bmatrix}_x + \begin{bmatrix} \rho\tilde{v} \\ \rho\tilde{u}\tilde{v} \\ \rho\tilde{v}^2 + p \\ (e+p)\tilde{v} \end{bmatrix}_y = -\frac{\tilde{w}}{r} \begin{bmatrix} \rho \\ \rho\tilde{u} \\ \rho\tilde{v} \\ (e+p) \end{bmatrix} \qquad (3.3.5)$$

Here the velocity $\tilde{w}$ in Π is the same as v in Λ and is:

$$\tilde{w} = \frac{\tilde{u} + \tilde{v}}{\sqrt{2}} \qquad (3.3.6)$$

A detailed check of this transformation has been made using the substitutions shown in Table 10.

Table 10: Connection of Quantities Between Grids

Quantity in Π	Quantity in Λ
ρ	ρ
p	p
e	e
$\tilde{u}$	$\frac{1}{\sqrt{2}}(u + v)$
$\tilde{v}$	$\frac{1}{\sqrt{2}}(v - u)$
x	$\frac{z+r}{\sqrt{2}} + x_0$
y	$\frac{r-z}{\sqrt{2}} + y_0$

Using this transformation and ref[21], we have

$$\begin{bmatrix} \frac{\partial}{\partial x} \\ \frac{\partial}{\partial y} \end{bmatrix} = \frac{1}{D} \begin{bmatrix} \frac{\partial y}{\partial r} & -\frac{\partial y}{\partial z} \\ -\frac{\partial x}{\partial r} & \frac{\partial x}{\partial z} \end{bmatrix} \qquad (3.3.7)$$

where

$$D = \frac{\partial x}{\partial z}\frac{\partial y}{\partial r} - \frac{\partial x}{\partial r}\frac{\partial y}{\partial z} = 1 \qquad (3.3.8)$$

Thus, we see that the vector $(\frac{\partial}{\partial z}, \frac{\partial}{\partial r})$ transforms just like the vector $\vec{A}$ in (3.3.2).

$$\begin{bmatrix} \frac{\partial}{\partial x} \\ \frac{\partial}{\partial y} \end{bmatrix} = \mathbf{T} \begin{bmatrix} \frac{\partial}{\partial z} \\ \frac{\partial}{\partial r} \end{bmatrix} \qquad (3.3.9)$$

47

It is important to realize that both the independent and the dependent variables are transformed when changing from the system in Λ to the system in Π. This is a different approach than is commonly used for "C" grids, where the independent variable is multiplied by a scalar, but otherwise unchanged. Nevertheless, the axiom that conservation laws are mapped into conservation laws is upheld by the transformation from one grid to another. Although the transformation from Λ to Π is a simple rotation, the amount of algebraic manipulation required is considerable. For brevity, these manipulations will not be included here but to insure accuracy the calculations were done by hand on two separate occasions and the same result was achieved. On physical grounds, it can be argued that the equations of motion of a compressible inviscid fluid would be invariant under rotations, and that such algebraic mainipulations betray a lack of confidence in what must be the physical truth. But the requirement of absolute certainty in equation (3.3.5) makes the tedious algebra well worthwhile.

Boundary Conditions. Since two regions, Λ and Π are used, the correct boundary conditions must be specified on the surfaces $\partial \Lambda$ and $\partial \Pi$. Second order accuracy can be achieved only on the points which can count two or more points between themselves and the boundary, as shown in Figure 3.11. Implementation of boundary conditions is discussed for the various cases A,B,C, and D below.

A.) Vehicle Surfaces.

Let $\vec{n}$ be the normal unit vector to the surface. The boundary conditions for the Euler equations at the hard wall vehicle surfaces are

$$\vec{u} \cdot \vec{n} = 0 \tag{3.3.10}$$

$$\frac{\partial p}{\partial n} \equiv \nabla p \cdot \vec{n} = 0 \tag{3.3.11}$$

B.) Grid Boundaries Interior to the domain Ψ

Let U_Λ be the solution in Λ, and U_Π be the solution in Π. Along the section of $\partial\Pi$ interior to Λ, with $\mu = \frac{1}{\sqrt{2}}$ we use the transformation $\mathbf{T}_{\Pi\Lambda}$ defined by:

$$\mathbf{T}_{\Pi\Lambda} = \begin{bmatrix} 1 & 0 & 0 & 0 \\ 0 & \mu & \mu & 0 \\ 0 & -\mu & \mu & 0 \\ 0 & 0 & 0 & 1 \end{bmatrix} \tag{3.3.12}$$

we have

$$U_\Pi = \mathbf{T}_{\Pi\Lambda} U_\Lambda \tag{3.3.13}$$

and along the section of $\partial\Lambda$ interior to Π, we have, with $\mathbf{T}_{\Lambda\Pi} = \mathbf{T}_{\Pi\Lambda}^T$

$$U_\Lambda = \mathbf{T}_{\Lambda\Pi} U_\Pi \tag{3.3.14}$$

Along the Segment with $z = 0$, $r > R_{base}$ for the boundary of the grid Λ, half of the points do not intersect exactly with points from Π, and so the field values from the four nearest points in Π are averaged and mapped onto $\partial\Lambda$.

C.) The corner, $z = 0$, $r = R_{base}$

This point has one point each from Π and Λ. The flow is singular there because the surface is discontinuous, and so the points are considered to be just slightly displaced along the surface, as shown in Figure 3.12. In this case, the standard surface boundary condition is used, so the corner points take information from within their respective grids.

D.) Exit Boundaries, or $\partial\Psi$

The outer perimeter of the computational domain is sufficiently far from the base surface that the expanding blast wave has accelerated to a high supersonic speed by the time it reaches the exit. Because the numerical scheme used is an upwind scheme, the flux vectors will have no component pointing back into the grid when this is the case, and so no information from the supersonic exit boundary can be

49

transmitted back into the grid. With $\vec{n}_{os}$ the normal vector for these outer surfaces, the simple 0th order boundary conditions are sufficient. These are implemented via

$$\nabla U \cdot \vec{n}_{os} = 0 \qquad (3.3.15)$$

These conditions provide for flux vectors F, G which do not radiate information into the domain. This has been checked and found to work. More advanced characteristic boundary conditions could be used, but in view of the physical situation, the high exit mach number negates their need.

Proof of Concept

The double grid plan and the corner assumption were tested by simulating the supersonic flow over a cone. In front of the cone face, an oblique shock forms, and around the corner, an expansion fan is centered. The freestream mach number is chosen to be 2.89, because for a $\gamma = 1.4$ ideal gas flowing over a 45° cone, the shock angle is predicted to be 60°. This prediction is due to the established solution for a cone at zero angle of attack. The density contour plot in Figure 3.12a shows a shock angle of 60° and a crisp expansion fan, despite that the run was made with a small grid. In addition, as the expansion fan reaches the shock wave, the wave weakens in pressure and density jump and makes a shallower angle with the free stream.

Part 4: PROP.FOR and Results.

Code Description

The code PROP.FOR stands for Propulsion, Fortran. This is a two-grid, axisymmetric or 2-D Euler code which calculates the blast flow emanating from the base of a cone. Boundary conditions were described in detail in Part 3. The difference operator used for the equations is selectable. The usual choice is the 2nd Order Upwind Steger and Warming Scheme, with the global search algorithm that replaces any undershoots with 1st order accurate results.

The equation of state for these calculations is an ideal gas, with $\gamma = 1.2$. Both the independent and the dependent variables are non-dimensionalized by the system parameters, in a manner analogous to the non-dimensionalization procedure used in the 1-D method of characteristics code reported in Chapter 2. Precisely, this amounts to a matrix multiplication of the Euler set by scalars and a substituion of non-dimensional space and time, and is given in Appendix 2. The objective of this non-dimensionalizing procedure is to scale the equations using the system reference density, ρ, detonation speed D, and laser on time τ, so that results of a particular calculation will be readily convertible to a variety of system parameter sets, instead of fixed for only one system design.

Initial Condition

For all runs, a plane LSD wave is used as the initial condition for the blast (Figure 3.13). The LSD is assumed to extend to the edge of the base of the vehicle, and edge effects during detonation are ignored. Treatment of the edge effects during detonation has also been achieved by a linear model in which the wave diameter decreases at the local speed of sound, which is 1/2 D. This leads to a trapezoidal shape for the detonation wave instead of a rectangle. However, for these blast runs,

51

the simpler rectangular shape was used. The blast wave aspect ratio (eq. 1.2.2), phrased in terms of the system parameters, is

$$A = \frac{\text{Vehicle Base Diameter}}{\text{LSD Travel Distance}} = \frac{2R_{base}}{D\tau} \qquad (3.4.1)$$

Advantage of Near Vacuum Ambient Conditions

In these runs, the pressure ratio of the initial base pressure to the ambient gas pressure is 10,000. The density ratio is 100. Figures 3.14a and 3.14b illustrate the flowfield after 2τ of blast. However, in Figure 3.14a, the density ratio was set to 10. In this case a strong shock wave forms, containing the propellant gas to a much smaller volume than in the case plotted in Figure 3.14b. Here, the smooth decay of the flow density contours (and pressure contours) shows that the gas is freely expanding and that the ambient gas is sufficiently thin that a vacuum is simulated.

1-D Core Routine

View of the x-t diagram for the 1-D flow shows a region of constant state behind the wave. In the center of the blast, there is a shrinking region of 1-D flow which is interior to a rarefaction wave propagating inward from the edge of the thruster. In this region, the flow is solved by the method of characteristics and superposed on the computational solution. Numerical error in this important flow region is then avoided, because the solution for the Euler equations in the 1-D region by method of characteristics is practically exact. In practice, the region of constant state behind the LSD and Blast is superposed on the solution, and the finite difference algorithm solves the rest of the flow. This core region contains the bulk of the gas which accounts for the blast impulse, and so by avoiding the inevitable buildup of numerical error in the core, the solution is enhanced. The core region is visible in Figures 3.14a and 3.14b. Here, the Aspect Ratio is 6 and the blast is 2 timesclaes

τ old, so the region of 1-D flow is still sizeable.

Impulse and Thrust Efficiency

The surface pressure is integrated in time on all vehicle surfaces to compute the instantaneous force on the vehicle. The vehicle mass is assumed to be so much greater than the mass of propellant gases that the vehicle is assumed to remain stationary during each blast. Consider a $100kg$ vehicle with a $1m^2$ base area. The gas slab is initially $1cm$ thick and has a density of $0.1kg/m^3$. The mass of gas in this case would be $10^{-3}kg$, which is 100,000 times less than the mass of the vehicle—validating the stationary vehicle assumption.

Integrating the pressure on all surfaces S the force on the vehicle is

$$\vec{F}(t) = \int_S p\,d\vec{A} \qquad (3.4.2)$$

Here, vector notation is used. By symmetry, the force lateral to the thrust vector cancels, and so a scalar treatment of force and impulse implies the component on the thrust axis. Adopting this convention, the impulse acquired is

$$I(t) = \int_{t_0}^{t} F(t')\,dt' \qquad (3.4.3)$$

The pressure integration scheme used on the base scans along the base and defines the area dA as well as P by taking the average radius and pressure between two adjacent points. In practice, the grid used is indexed by the integers (j,k) in the (z,r) directions, yielding

$$
\begin{aligned}
dF &= \bar{p}\,dA \\
\bar{p} &= \frac{1}{2}(p_k + p_{k-1}) \\
dA &= \bar{r}\,dr \\
&= \frac{1}{2}(r_k + r_{k-1})(r_k - r_{k-1})
\end{aligned}
\qquad (3.4.4)
$$

is a valid one. Thrust measurements for large Z will not exceed 1-D performance (where $A = \infty$), but they will closely approximate it as Z is increased to 4 or more.

Therefore, this analysis recommends using a larger target size than LSD diameter as a means of simulating 1-D performance in the laboratory. In addition it asserts and proves, by the rapid convergence of impulse advantage and the comparison of (A,Z) results with 1-D results, that the ballistic measurements of impulse obtained with large flat targets for finite aspect ratio waves will still be less than the impulse received by a 1-D thruster. It is thus valid to claim the thrust experimentally received by area outside the laser spot as thrust which would be received by a large aspect ratio vehicle.

Part 6: Skirt Nozzle Simulations

Section 1: Boundary Conditions and Code Assumptions

To improve the performance of a thruster operating with a small Aspect Ratio, a skirt device has been suggested as a means of containing the propellant within a smaller volume. An important design constraint for such a skirt is that it does not occlude the propellant surface from the laser, even when the beam incidence is not along the thrust axis. The work accomplished with the 45 degree cone, culminating in the code *PROP.FOR* is used as the basis for a code which simulates a 45 degree cone with a nozzle that is an extension of the cone's angled face–*SKIRT.FOR*. The vehicle geometry is shown in Figure 3.21. This code is a superset of *PROP.FOR*, with a specialized boundary condition for the skirt section of the vehicle.

Considering the Axisymmetric Euler equations, the most direct method of implementing boundary conditions is to specify the value of all fluxes F and G on the boundary of the computational domain.

$$U_t + F_z + G_r = S(U, r)$$

A second approach, used here, is to specify the value of the field vector U on the boundary. This value of U provides for the correct value of the flux vectors F and/or G , and is a reasonable extrapolation of the local field. This way, good plots which include the boundary points can be constructed, and the mathematical influence of the selected boundary field points is correct. For example, consider a hard flat wall, with the grid lines normal to it. Only the pressure need be specified at the wall in order to feed the correct information into the grid's interior points. No velocity component normal to the wall is possible, but the tangential component is not in general equal to zero. Provided that the correct value of the pressure is specified,

the use of physical assumptions to specify the tangential flow velocity is acceptable, and yields more attractive plots of the solution.

Additional complexity is introduced when simulating a thin skirt that juts out into the computational domain, but the same Euler BC's apply and can be implemented to a satisfactory degree of accuracy. The Euler BC's are

$$\vec{u} \cdot \vec{n} = 0$$
$$\frac{\partial p}{\partial n} \equiv \nabla p \cdot \vec{n} = 0 \qquad (3.6.1)$$

Since it makes a 45° angle with the axis of symmetry, the skirt is diagonal to the grid lines in the primary grid. Thus the key to the problem is to find the field value at a point which is normal to the skirt. The tangential flow pattern dictates that u=v along the skirt surface. With normal vectors as shown,

$$\text{Underside}: \vec{n} = (n1, n2) = \frac{1}{\sqrt{2}}(1, -1)$$
$$\vec{t} = (t1, t2) = \frac{1}{\sqrt{2}}(1, 1)$$
$$\text{Upperside}: \vec{n} = (n1, n2) = \frac{1}{\sqrt{2}}(-1, 1) \qquad (3.6.2)$$
$$\vec{t} = (t1, t2) = \frac{1}{\sqrt{2}}(1, 1)$$

The grid lines in the main grid are not normal to the skirt, so additional relations for the density and tangential velocity components must be prescribed. There is a danger here of ruining the solution by overspecifying the B.C.'s. However, the conditions used are physically compatible with the initial condition of a plane LSD wave launched off the base of the thruster. View of the results shows that the assumptions **A1.**, **A2.** lead to a continuous field structure in which the pressure contours are normal to the surface of the grid, which they must be if (3.6.1) is held there.

$$\textbf{A1.}\ \frac{\partial \rho}{\partial n} = 0$$
$$\textbf{A2.}\ \frac{\partial (\vec{u} \cdot \vec{t})}{\partial n} = 0 \qquad \qquad (3.6.3)$$

On **A1.**: If the entropy, s , obeys $ds/dn = 0$ then **A1.**. follows as a direct consequence of(3.6.1). In a controlled expansion flow, assumption of no entropy gradient is generally safe.

On **A2.**: The physical situation of the propagating LSD agrees with this assumption. Once the thin shock layer has passed, the flow induced behind it is quasi-steady in comparison. Soon into its development, the presence of the skirt will allow for large velocities along it, but not normal to it. This is consistent with condition **A2**. So long as there are not strong convective waves moving toward the skirt surface– and this is true for the LSD wave–, condition **A2** is accurate.

These assumptions are physical in nature and depend on the flow character. For engineering purposes, the practicality of a skirt device could be assessed if the simulation were carried out under the assumption of quasi- one dimensional flow at the boundary; these conditions are more accurate.

Section 2: Results

To run *skirt.for* the skirt length L_{skirt} is a variable, and the parameter space under study involves the skirt length and the Aspect Ratio. The skirt length is non-dimensionalized by the LSD travel distance to create the parameter Z:

$$Z = \frac{\text{Skirt Length}}{\text{LSD Travel Distance}} \equiv \frac{L_{skirt}}{D\tau} \qquad (3.6.4)$$

Blast simulations are performed over a parameter space in (A, Z), to determine the impulse transmitted to the vehicle. The ranges simulated are:

$$\text{Aspect Ratio} : 2 \leq A \leq 10$$
$$\text{Skirt Length} : 0 \leq Z \leq 4 \qquad (3.6.5)$$

The emphasis is on small Aspect Ratios, because the prior work has shown that for

61

$A > 24$, a great deal of the 1-D value of the impulse is recovered by a thruster with no skirt, which corresponds to $Z = 0$. Figure 3.23 shows impulse development in time for a vehicle without a skirt and with a skirt to show the substantial advantage that a skirt device can yield for small Aspect Ratio waves. Figure 3.24 shows the converged values of the normalized impulse transmitted to the vehicle by the LSD/Blast wave over the (A, Z) range in question. Again, the normalization factor for the impulse is the impulse received during the detonation phase.

Due to the comparatively small values of A simulated, it was possible to run the computer simulations until the impulse converged; the product: (COMPUTER TIME)×(MEMORY REQUIRED) increases substantially with A. Of note is the large increase in performance achieved for even a short skirt. Containment of the lateral expansion during the first few timescales of the flow enables the thruster to approach 1-D performance. In addition, the 45° skirt increases the area for the exhaust gases to push against, yielding better performance.

The area ratio AR of the nozzle is established in terms of the parameters (A, Z) via

$$AR = 1 + 4\frac{Z}{A} + 4\frac{Z^2}{A} \qquad (3.6.6)$$

The area ratio is plotted over the parameter space in Figure 3.22 When $A = 2$ The high AR values for the case explain the large relative magnitude of the impulse acquired by the thruster. In fact, the normalized impulse for the case $Z = 4$, $A = 2$ is the greatest in the parameter space, indicating the strength of the area ratio's influence on the solution.

Part 7: Point Explosion Benchmark

For 1-D nonsteady gasdynamic codes the usual benchmark for a code's accuracy is the shock tube simulation. However in 2-D and axisymmetric nonsteady calculations there is no benchmark which is quite as good. Nevertheless, there is a flow which can test a higher dimensional code: the point explosion. Far away from the core of the explosion, the shock front of a blast wave following a point explosion propagates according to the power law:

$$R(t) = Ct^\delta \qquad (3.7.1)$$

Where R(t) is the position of the wave front, C is a constant, and δ depends on the number of dimensions of the flow and the structure of the ambient density field into which the blast propagates. With α and ν to be subsequently defined we have for δ

$$\delta = \frac{2}{\nu + 2 - \omega} \qquad (3.7.2)$$

The general case for the density field is a power law for the density with A a constant and

$$\rho = Ar^{-\omega} \qquad (3.7.3)$$

In the calibration runs performed here, the ambient density is a constant, so $\omega = 0$. The geometric term ν is the number of dimensions of the flow. We have

$$\nu = 1 : \text{Plane, 1-D Blast}$$

$$\nu = 2 : \text{Cylindrical, 2-D Blast}$$

$$\nu = 3 : \text{Point, 3-D Blast}$$

Simulated here is a ball of hot gas released in an axisymmetric field, so $\nu = 3$. And since $\omega = 0$, we expect that

$$R(t) = Ct^{\frac{2}{5}} \qquad (3.7.4)$$

In fact for $\omega = 0$, the values for δ with $\nu = (1, 2, 3)$ are $\delta = (2/3, 1/2, 2/5)$.

In addition to specifying the trajectory in (r, t) space via the power laws above, quadratures of the flowfield profile behind the blast wave front have been performed by Sedov [23] for the strong point explosion, where counterpressure is ignored. Korobeinkov [24] includes the effect of counterpressure and a thorough treatment of Sedov's problem. G.I. Taylor also studied this problem[17], and is mentioned in Courant and Friedrichs[22]. Of historical interest, the power law scaling of these blasts have been borne out by experience. Apparently Taylor correctly estimated the yield of an atomic bomb by viewing the time intervaled photographs of its blasting fireball which had been released by the AEC, causing some alarm. By plotting r versus t he was able to estimate the energy which had been released.

This point explosion problem, or PEP, is an ideal test problem for a new 2-D or axisymmetric Euler algorithm because there is a high degree of symmetry in the flow and a highly precise solution in the literature. The second order Steger and Warming method, with its modification for extreme pressure and density jumps introduced by the author, is tested here. In order to simulate a blast wave emanating from a point explosion, the code *PROP.FOR* was made into an axisymmetric testbed *ORION.FOR* and the initial condition package was changed to the case of a point explosion in an otherwise quiescent ambient fluid. In all cases, $\nu = 3$ and $\gamma = 1.4$. The wave is allowed to propagate a substantial distance, at which time the profiles of density, pressure, and velocity are compared with the values from [23] and [24] . Generation of the Sedov data is performed separately in the code *SEDOV.FOR*, which also was developed for the test. Figure 3.26a shows the propagation of the shock front with time, as well as the curve for which $R = t^{\frac{2}{5}}$, which is the predicted propagation for this situation. The data is presented in a log-log manner in Fig 3.26b. Agreement is excellent.

The approach for collecting and presenting the numerical data is to take a snapshot

of the flow at the initial condition and at three stations. The initial condition
used is the Sedov Profile, and thus the numerical algorithm is tested by comparing
the station data to the initial condition. In general the velocity behaved very
predictably, its profile remaining linear in all cases. The density and pressure are
shown at station 0, the initial condition, with a radius of 35 grid points, and at
stations 1,2, and 3, with respective radii of 55,60, and 65 grid points. Since $R = Ct^{\frac{2}{5}}$,
if the time of the solution initially is called t_0 then the time at station 3 would be
$4.7t_0$. During this time, the wave overpressure is substantially reduced, as can be
seen from the station data persented in Figure 3.27 The density ratio across the
shock, nominally 6, is not achieived however, due to the fact that the density jump
at the shock is immediately followed by a very steep drop in the density to nearly 0.
As the wave expands, the number of data points within the wave increases, yielding
better resolution of the solution on the equispaced grid. Figure 3.28 illustrates the
density profile. A value of 5 for the density jump is achieved at station 3.

To test the self-similarity of the solution, the pressure and radius are normalized
by their wave front values. The wave front position on the grid is designated to
be the point of maximal pressure. The pressure data at all stations are shown in
Figure 3.29. At stations 1,2, and 3 the core pressure is 1.04, .94, and .91 of the
nominal 0.365 value. It was deemed unnecessary to normalize the density; it is
simply plotted versus the normalized radius in Figure 3.30 to compare the shape of
the profiles. At stations 2 and 3 the fit is very close to the Sedov solution, although
at neither station is the density peak of 6 achieved. Nevertheless, to drive the figure
to 6 simply requires more computer memory and power. The close agreement of
the density profile at all other points suffices to capture the vast majority of the
steep shock and the rapid drop off of the density behind it.

Detailed study of the density profile for Sedov's solution shows that the strong point

explosion is an extremely challenging flow to capture by direct simulation of a bomb, making it a very tough benchmark for a numerical algorithm. As already noted, for $\gamma = 1.4$, the density falls from 6 times the ambient to near 0 in a very thin region behind the wave front, so it requires an enormous amount of data to represent this phenomenon on an equispaced mesh. At the core of the explosion $\rho \to 0$, leading to additional difficulty – the pressure remains finite at the core of the explosion, and so the temperature, which is propotional to $\frac{P}{\rho}$, becomes infinite at the core. Thus the speed of sound, which is proportional to $\sqrt{T}$ also becomes infinite, and so even though there is no mass present in the core region, the numerical stability requirement imposed by the Courant condition leads to very small time steps. We have

$$(|\vec{u}| + c)_{max} \Delta t \le \Delta x \qquad (3.7.5)$$

Since $c \to \infty$ at $r = 0$, satisfaction of the Courant condition leads to

$$\Delta t \to 0 \qquad (3.7.6)$$

Therefore, exact duplication of the Sedov profile is impossible via explicit computational means because of the singularity of T as $r \to 0$, yet good quality simulations are possible. The key to solving the problem accurately is to drive the density in the core region as low as is economically possible [25]. With each reduction of the core density came an improvement in the results. A high speed of sound behind the wave keeps the core of the flow in contact with the wave front, and good solutions are extracted. If the core density is made too high, the solution can be lost. This flow is more difficult to capture on a grid than the Laser Propulsion blast, because it has a tremendous density and pressure gradient behind the shock. The grids used for these calibrations were 64^2 and 128^2, respectively, with clearly better results obtained with the bigger grid. Only the runs on the 128^2 grid are presented, beacause of the density jump's large data requirement.

The calibrations have achieved, for axisymmetric point explosion:

1. Excellent Agreement of $R(t) = Ct^{\frac{2}{5}}$ with theory

2. Good Pressure Profile Agreement. Errors of +4,-6, and -10 percent with the Sedov profile after considerable change in the solution.

3. Good Density Profile Agreement at sufficient radius. The peak value is missed but the overall profile shapes agree well.

From these runs the amount of data required to adequately represent the LSD wave as an initial condition can be better estimated. The initial size of the Sedov wave used here was 36 cells from core to wave front. For close work on the laser thruster, a bare minimum of 12 points and a preferred lower bound of 16 points are needed from the base to the wave front to avoid the type of behavior where the density jump is cut off. Using 32 points to represent the LSD wave from base to wave front is very conservative, and requires much more storage, so it is overkill in the preliminary design and conceptual phase for a system. In the LSD wave, the gradients in density are nowhere near as steep as in the Sedov wave, and so the data requirement is reduced.

Chapter Four

Real Gas Propellant Modeling

Part 1: Introduction to Propellant Modeling

The chief endeavor of this thesis is the prediction of axisymmetric expansion efficiency, which depends mainly on the geometry of the LSD wave and thruster, and only secondarily on the choice of propellant. However, The 1-D impulse received by the thruster depends strongly on the propellant used and the detonation speed achieved. In addition, the laser power and energy delivery required to drive a system also depend strongly on the propellant selected. Theoretical and experimental results on Lithium Hydride show it to be a promising propellant, and the best candidate yet found. Therefore, to better describe the thrust efficiency of a laser propelled vehicle, an investigation into the properties of the candidate propellant Lithium Hydride is worthwhile.

Among others, the ideal ablative laser propellant would have these properties.

Lithium Hydride does not meet all of these requirements, but they are not equally important. It has a high ablation energy, at 35,000 kJ/kg [26]. Potentially, its frozen flow losses are high, in the range of the ablation losses, because of the substantial energy of the H_2 bond. Where it excels is in categories 4-6. When evaporated by ablation, the LiH gas consists of Li atoms and H_2 molecules in the equilibrium state. The Lithium atoms ionize when 5.39 eV is supplied, which is a comparatively low figure–Hydrogen ionizes at 1 Rydberg = 13.6 eV. Lithium's low ionization energy makes the production of ions necessary to initiate and sustain an LSD wave possible at a lower laser flux than many other candidate propellants. Theoretical analysis of LiH performed by Physical Sciences, Inc. predict that an LSD wave can be maintained over a large range of laser flux and ablated gas density[27].

Table 12: Desirable Laser Propellant Properties

1. Low cost

    The bottom line.

2. Storability and structural strength

    A simple vehicle design is a prime objective.

3. Low Ablation Energy Requirement

    Ablation Energy is not recoverable for thrust.

4. Low Threshold Laser Flux for LSD maintenance

    Very important for laser propagation efficiency.

5. Low Molecular Weight

    The kinetic energy of a molecule is $\frac{1}{2}mv^2$,

    favoring low m for propellant gases.

6. Ease of LSD wave initiation

    Generally, ease of ionization leads to this.

7. Low Frozen Flow Losses

    A great deal of chemical bond energy may be lost.

8. Robust Operating Range of Laser Flux and Ablation Densities.

    The propellant should be flexible to system parameter variations,

    so that tolerances on the laser driver are not too severe.

Hale[9] and Reilly[10] have each reported Isp's of 800-1000 sec using LiH as the propellant driven by CO_2 lasers. These experiments were performed at small scale, where the axisymmetric expansion losses are high, and so the achievement of such high Isp is promising.

In this chapter, equilibrium Lithium Hydride will be investigated to determine an

engineering model of its equation of state. Secondly, a more complex model, which assumes that the ionization of the Li atoms is in equilibrium while the dissociation of the Hydrogen is frozen will be developed. Compatibility of the model with the work of Physical Sciences, Inc. on LSD structure will be shown, and the rarefaction wave behind the propagating LSD wave will be constructed. Results for the frozen chemistry model will be shown and compared to the case of the idealized assumptions used in setting up the LSD wave for the work of Chapter 3. And finally, an analysis of the reaction rate for the recombination of the Hydrogen atoms will be made to roughly determine what amount of recombination will take place, and where it is significant.

Part 2: Equilibrium Lithium Hydride

Section 1: Functional Form

The ideal gas equation of state, $p = \rho RT$ is a familiar member of the class of equations of state with the following functional form:

$$p = \rho f(\varepsilon) \tag{4.2.1}$$

where ε is the internal energy per unit mass of the gas, and is found from the stagnation energy per unit volume e. First, the internal energy per unit volume ϵ is found from the stagnation value:

$$\epsilon = e - \frac{1}{2}\rho|\vec{u}|^2 \tag{4.2.2}$$

Factoring out the density gives the internal energy per unit mass

$$\varepsilon = \frac{\epsilon}{\rho}. \tag{4.2.3}$$

With the definitions above, confusion among the $e, \epsilon,$ and ε quantities is avoided.

Flux vector splitting is made possible by the homogeneity property of the Euler equations. This splitting permits the computational simulation of the extreme flow situation in laser propulsion. In order for the Euler equations to have fluxes which are homogeneous, an equation of state with the functional form of eq.(4.2.1) is stated by Steger and Warming to be sufficient. This homogenaiety will be shown in one dimension; it also applies in two and three dimensional Euler sets. Within the 1-D Euler equation,

$$U_t + F_x = 0 \quad \text{with} \quad F = F(U) \tag{4.2.4}$$

we find that, for scalars α,

$$F(\alpha U) = \alpha F(U). \tag{4.2.5}$$

71

This leads to flux vector splitting, because (4.2.5) implies

$$F = \mathbf{A}U \quad \text{and} \quad \mathbf{A} = \frac{\partial F}{\partial U} \tag{4.2.6}$$

The split fluxes are formed by finding the eigenvalues and eigenvectors of $\mathbf{A}$, and carrying out the procedures given by Steger and Warming. Other functional forms do not work. For example, a perturbation analysis using δ as a small number was performed. The equation of state used was, with g a continuous function,

$$p = \rho(1 + \delta g(\rho))f(\varepsilon). \tag{4.2.7}$$

Using the symbolic manipulator program *MACSYMA*, this functional form was put to the test by direct substitution into the Euler equation (4.2.4). It was hoped that this functional form would satisfy the homogenaiety requirement in eq. (4.2.5) but it failed. Had it succeeded, greater flexibility in constructing a model equation of state for Lithium Hydride would have been achieved. The rationale behind this is that in truth, a real gas has an equation of state which is a function of two variables:

$$p = f(\rho, \varepsilon) \tag{4.2.8}$$

Forms of the type in eq.(4.2.7) at least allow for values of $\left(\frac{\partial p}{\partial \rho}\right)_\varepsilon$ which vary with the density at the order δ. Perhaps other investigators will attempt to find new functional forms which can satisfy (4.2.5). I discuss it here because if these do exist and are found, greater flexibility for real gas modeling will result.

Section 2: Techniques

Accepting the functional form of eq(4.2.1), the model used here is similar to the ideal gas equation of state. For LiH, the functional form used is

$$p = \beta\rho(\varepsilon - \varepsilon_0). \tag{4.2.9}$$

The approach taken is to find the region in (ρ, ε) space in which the propellant is to operate, and is shown schematically in Figure 4.1. This is given by a box in the (ρ, ε) space with boundaries

$$0.01\frac{\text{kg}}{\text{m}^3} \leq \rho \leq 0.2\frac{\text{kg}}{\text{m}^3}$$
$$20,000\frac{\text{kJ}}{\text{kg}} \leq \varepsilon \leq 120,000\frac{\text{kJ}}{\text{kg}} \tag{4.2.10}$$

At the hottest point, where $\rho = .2$ and $\varepsilon = 120,000$ in the units given above, the conditions correspond to a pressure of 40 atm and a temperature of 10,000 Kelvin. These conditions were the Chapman-Jouget conditions for the LSD wave reported by Physical Sciences Inc. at the Laser Propulsion Workshop held at Lehigh University in July, 1989. Within the box described, condensation of the LiH takes place. These points are found in the relatively small subregion described by

$$0.1\frac{\text{kg}}{\text{m}^3} \leq \rho \leq 0.2\frac{\text{kg}}{\text{m}^3}$$
$$20,000\frac{\text{kJ}}{\text{kg}} \leq \varepsilon \leq 25,000\frac{\text{kJ}}{\text{kg}} \tag{4.2.11}$$

The points in this subregion are not considered in development of a gas law. Over a grid of (ρ, ε) points in the propellant operating range, the pressure is found using an equilibrium thermodynamic code from NASA [18]. A least squares fit of the data on the functional form given by (4.2.9) is made, using techniques outlined in [28]. The results:

$$\beta = 0.221$$
$$\varepsilon_0 = 11655\frac{\text{kJ}}{\text{kg}} \tag{4.2.12}$$

Substitution of the form (4.2.9) into the Euler equations was performed with *MACSYMA*, yielding Euler eigenvalues. With the speed of sound c defined by

$$c = \sqrt{\frac{(\beta+1)p}{\rho}}$$

the eigenvalues are $u - c, u, u + c$ for the 1-D Euler equations. The form (4.2.9) is thus equivalent in many respects to an ideal gas form. Here the effective γ is

$$\gamma \equiv \beta + 1 = \quad \Rightarrow \quad c = \sqrt{\frac{\gamma p}{\rho}} \tag{4.2.14}$$

Thus, the model yields a γ of 1.221 for equilibrium LiH. Due to the equation of state used, this γ is identical to the $\bar{\Gamma} = H/E$ seen in the literature on real explosives. In reference [29], the authors point out that $\bar{\Gamma} \neq \gamma$ in general. For an ideal gas, they are equal. For Lithium Hydride, the agreement between the equilibrium speed of sound and the speed of sound calculated using (4.2.14) is quite close, as will be shown. Thus the quantities $\bar{\Gamma}$ and γ are equivalent over the operating propellant range.

Section 3: Results

Two curves are shown, for each the density is $\rho = 0.05\frac{kJ}{kg}$. The internal energy per unit mass, ε, is scanned over its operating range. Figure 4.2 shows the model and the equilibrium values for the pv product, which is simply $\frac{p}{\rho}$. Figure 4.3 shows the model and the equilibrium values for the speed of sound, with the speed of sound for the model calculated from eq(4.2.14). Agreement between the model and the equilibrium data is very close. At other densities, the agreement is also very close.

Despite the occurrence of dissociation and ionization processes in equilibrium LiH, its behavior is well approximated by the simple equation of state in eq. (4.2.9). This is due to the fact that these processes are activated gradually as the temperature of the gas is increased. An understanding of the basic mechanisms within LiH assists in explaining the good agreement between such a simple model with the data. In the evaporated state, LiH consists of Li atoms and H_2 molecules. As the temperature is increased, the H_2 molecules dissociate. After a high degree of dissociation is achieved, the next reaction to activate is the ionization of the Li atoms. These reactions are driven to completion in the case of H_2 dissociation and activated in the case of Li ionization only over a large change of temperature, so the equilibrium data is quasi-linear in the operating propellant range of density and energy. We

74

have

$$H_2 \to 2H : \qquad T : 3000K \to 5000K$$

$$(4.2.15)$$

$$Li \to Li^+ : \qquad T : 5000K \to 10,000K$$
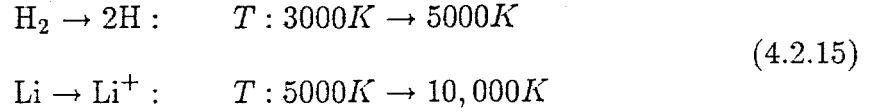
Thus, Figures 4.2 and 4.3 show that for engineering purposes, a simple $\gamma = 1.221$ model of the equation of state for LiH yields good agreement with the behavior of the propellant in equilibrium.

Section 4: Equilibrium Code Testing

The Gordon McBride code is always useful at temperatures below 6000K, for which it was designed, yet it needs to be shown that it can be used to generate correct data at the elevated tempeartures used here. The hydrogen in the LiH is fully dissociated at temperatures below 6000K, and so the chief question is whether or not the Gordon McBride code can correctly predict the Lithium ionization. Fortunately, another data source, *Tables on the Thermophysical Properties of Liquids and Gases*, by Vargaftik[32], contains data on the ionization of Lithium at the high temperatures considered here. Comparison of data generated with the Gordon McBride code and the data in ref[32] shows good agreement, so the Gordon McBride code is validated.

Table 13: Lithium Ion Mole Fraction Data from Two Sources

P=.967 atm			P=9.67 atm	
G.-McB.	Vargaf.	T(K)	G.McB.	Vargaf.
.00733	.00725	4000	.00232	.0023
.136	.135	6000	.0480	.0476
.379	.381	8000	.191	.194
.470	.473	10000	.342	.354
.489	.492	12000	.422	.440

Part 3: Chemically Frozen Lithium Hydride

Section 1: LSD Processing of Ablated Lithium Hydride

The equilibrium constituents of LiH vapor following ablation are not molecules of LiH, but rather Lithium atoms mixed with H_2 molecules at a ratio of 2:1. For LSD waves of interest, the heat addition by laser is sufficient to fully dissociate the H_2 , and to partially ionize the Lithium. Following laser heating, two flow characteristics make it a good engineering approximation to assume that no Hydrogen recombination will take place:

1.) The temperature following the LSD wave is several thousand degrees hotter than that required for recombination to be significant. In the equilibrium gas state for these cases the Hydrogen is fully dissociated, so recombination will not occur.

2.) In laser propulsion the flow time scales are of microsecond order, so there is not sufficient time for recombination to occur.

An analysis of the reaction rate for recombination of the Hydrogen is made in Section 4. Because the recombination reaction in which 3 Hydrogen atoms collide to form 1 molecule of H_2 with the third H acting as a collision partner is fast, some recombination of the Hydrogen toward the equilibrium state is expected over a range of (Φ, ρ_0, τ) which are the main pulse laser flux, ablated gas density, and main pulse laser on time. But there is a large range of these parameters for which Hydrogen recombination will not be significant, and the description of the Lithium Hydride in this region is the primary task of this section.

Section 2: The Model

The Post LSD Lithium Hydride gas has four constituents:

Li	Lithium
H	Hydrogen
Li^+	Lithium Ion
e^-	Electron

The objective of the model is to calculate a γ for the dissociated LiH vapor which has been processed by the LSD wave (Figure 4.4). The end result is the equation

$$p = (\gamma - 1)\epsilon . \tag{4.3.1}$$

where p is the pressure and ϵ is the internal energy per unit volume, given by the density times the internal energy per unit mass. This equation of state a simple approximation to a more complex constitutive relation and so the results generated from it are to be viewed as approximate.

The gas is assumed to be charge neutral, and no diffusion of molecular species is assumed, and so the number density of the mixture is given by

$$n = n_H + n_{Li} + n_{Li+} + n_{e-} \tag{4.3.2}$$

subject to the constraints

$$n_{e-} = n_{Li+} \tag{4.3.3}$$

$$n_H = n_{Li} + n_{Li+} \tag{4.3.4}$$

77

The notation used here is similar to that found in Vincenti and Kruger's *Physical Gas Dynamics* [30]. The ionization is determined by the Saha equilibrium ionization equation, where α, the degree of ionization, is introduced.

$$\alpha = \frac{n_{Li+}}{n_{Li} + n_{Li+}} \qquad (4.3.5)$$

Thus,

$$n_e = n_{Li+} = \alpha n_H \qquad (4.3.6)$$

$$n_{Li} = (1 - \alpha)n_H \qquad (4.3.7)$$

Using the stoichiometric constraints and the values for the molecular weight of each species, the total number density n is computed from the flow mass density ρ and the degree of ionization via

$$n_H = \frac{\rho}{m_{Li} + m_H} \qquad (4.3.8)$$

$$n = n_H(1 + (1 - \alpha) + 2\alpha) = (2 + \alpha)n_H \qquad (4.3.9)$$

The internal energy of each constituent of the gas depends on its temperature. The generalized equation for the energy in terms of the temperature for each constituent depends on its partition function, defined by

$$Q = \sum_j g_j exp(\frac{-E_j}{kT}) \qquad (4.3.10)$$

where

Q is the partition function

E_j is the energy at level j

g_j is the degeneracy factor for level j, given by quantum mechanical selection rules.

k is Boltzman's constant, which is $1.380 \times 10^{-23} J/K$.

For each constituent i, the energy per unit volume is given by:

$$\epsilon_i = n_i kT^2 \frac{\partial}{\partial T}(\ln Q_i) \qquad (4.3.11)$$

Due to the expected temperature range of from 2000K – 10000K for laser propulsion, internal electronic states of the hydrogen atoms and the lithium ions are not significant contributors to their respective internal energies. Thus, the internal energies per unit volume for each constituent are given by:

electron: $\qquad \epsilon_{e^-} = \frac{3}{2}n_{e^-}kT$

Li Ion: $\qquad \epsilon_{Li^+} = \frac{3}{2}n_{Li^+}kT + n_{Li^+}I$

H atom: $\qquad \epsilon_H = \frac{3}{2}n_H kT$

Li atom: $\qquad \epsilon_{Li} = \frac{3}{2}n_{Li}kT + \beta_{el}(T)n_{Li}kT$

where I = 5.39 eV is the ionization energy of the Lithium, and $\beta_{el}(T)$ is a function of the amount of electronic excitation of the Lithium atoms. $\beta_{el}(T)$ can be large, up to 2.4 in some cases, due to the substantial number of electronic energy levels available to the Li atom. In flow calculations, the internal energy per unit volume is readily obtained from the stagnation energy per unit volume, which is one of the flow variables:

$$\epsilon = \sum_i \epsilon_i = e - \frac{1}{2}\rho(u^2 + v^2) \qquad (4.3.12)$$

Thus from the flowfield vector, the values of ρ and ϵ are known. In order to determine T and α an iterative Newton-Raphson algorithm is required. For the first iteration the flow density and an assumed temperature are used, and then α is computed, via the Saha equation

$$\frac{\alpha^2}{1-\alpha} = \frac{2(m_{Li} + m_H)}{\rho}\left(\frac{2\pi m_e kT}{h^2}\right)^{\frac{3}{2}}\frac{Q_{Li+}}{Q_{Li}}exp\left(\frac{-I}{kT}\right) \qquad (4.3.13)$$

in which h is Planck's constant and the lone factor of 2 on the RHS accounts for the up–down spin internal degeneracy for the electron partition function.

With α known, a candidate value for ϵ is calculated. Comparison of the calculated value for ϵ with the flowfield value then produces a new estimate for the temperature, and the cycle is repeated.

After about three of these iterations, agreement between the flowfield value for ϵ with the computed value is within 1 percent, and the correct T and α values are thus found, permitting calculation of the pressure via

$$p = nkT \qquad (4.3.14)$$

With $p(\rho, \epsilon)$ now calculated the γ is found:

$$\gamma = 1 + \frac{p}{\epsilon} \qquad (4.3.15)$$

For Lithium Hydride vapor at its peak operating temperature, the model computes $\gamma \approx 1.2$ with a degree of ionization $\alpha \approx 0.1$. In the cold gas region where $\alpha \to 0$, the model reports the value $\gamma = 1.6667$ which is the correct value for an ideal monatomic gas.

The model has been integrated into the gas-dynamic code *PROP.FOR* written for expansion calculations to produce a new code called *PROPLIH.FOR*. The cost of computing γ at each and every field point for each iteration of a calculation is reduced without much loss in solution quality if a menu file of $\gamma(\rho, \epsilon)$ is generated and maintained in core storage.

Part 4: Reaction Rates for Hydrogen Recombination

A great deal of energy is stored in the H_2 chemical bond. The precise figure is 4.6 eV/bond. In more conventional units of measure, we can estimate the amount of laser energy per pulse which is directed into the dissociation of this bond for a Lithium Hydride propelled vehicle, and it comes out to be roughly 25% of the energy input per pulse cycle. The ablation of LiH is also costly, using another 25% of the energy of the pulse cycle, as shown in Figure 4.4 a. This is a drawback to using LiH, but the material does have other significant merits, as pointed out in section 1 of this chapter. This section estimates under what conditions the recombination of the dissociated H_2 will be significant.

In section 3 of this chapter, a model which assumes that no recombination of the dissociated Hydrogen molecules in the Lithium Hydride propellant takes place. The validity of this assumption will be tested here, and the range of vehicle operating parameters for which it is true will be estimated. First of all, it is only necessary to study the recombination reaction rate for those temperatures and pressures where any significant recombination will occur, because initially, the LSD wave will have fully dissociated the H_2. In the ρ, ε or T, p range where the equilibrium dissociation of H_2 molecules is above 90%, the effect of recombination of the H atoms to form H_2 is only of second order importance. When conditions arise where the equilibrium dissociation of the H_2 is below 90%, reaction rate analysis is necessary. The degree of dissociation is defined by $\bar{\alpha}$ (note $\bar{\alpha}$ is different from the degree of ionization α of eq.(4.3.5))and is

$$\bar{\alpha} = \frac{n_H}{n_{H_2} + n_H}. \tag{4.4.1}$$

Using the same computer code as in Chap.4, Sec.2, to generate equilibrium data for Lithium Hydride, the following table of using pressure as the independent variable was constructed to find the temperature at which the recombination of the H_2 is

81

Table 14: Temperature at which Equilibrium LiH is 90% Dissociated,
with Recombination Reaction Time Scales. *

Pressure (atm)	Temperature (K)	τ_{chem} sec
0.5	3400	5.0×10^{-3}
0.1	3600	2.6×10^{-3}
0.5	4000	1.7×10^{-4}
1.0	4200	5.5×10^{-5}
5.0	4800	6.1×10^{-6}
10.0	5000	2.1×10^{-6}
15.0	5250	1.7×10^{-6}
20.0	5400	1.1×10^{-6}

* The method of calculation for τ_{chem} will follow.

significant.

At these conditions, a reaction time scale can be constructed for the fastest reaction
in the general family of reactions

$$H + H + M \rightarrow H_2 + M \tag{4.4.2}$$

Here M is a collision partner, which may be in the case of dissociated LiH another
H atom, an Li atom, an H_2 molecule, or an electron or a Lithium ion. Because
the ionization is not appreciable until $T \rightarrow 5000K$, the temperatures in Table 14
indicate that the most likely collision partner M will be a charge neutral species;
the charged particles are not considered here, but it is possible that even in small
concentration they affect the recombination due to the high collision cross sections
of charged species and/or the high thermal speed of the electrons.

82

Rate data for $M = H$ and $M = H_2$ show that the fastest reaction partner is H. The equation of recombination is stated and it is bounded from above by disregarding the forward dissociation reaction.

$$\frac{d[H]}{dt} = -k_f[H_2][M] + k_b[H][H][M] \leq k_b[H][H][M] \qquad (4.4.3)$$

Here, using the data in [31], the rate constants are given below

---

Table 15: Rate Data for Hydrogen Recombination

$M = H$ $k_b = 1.3 \times 10^{30} \ T^{-4} \ cm^6 mol^{-2} s^{-1}$

$\qquad\qquad\qquad k_b(5000) = 2.08 \times 10^{15} \ cm^6 mol^{-2} s^{-1}$

$M = H_2$ $k_b = 2.6 \times 10^{18} \ T^{-1} \ cm^6 mol^{-2} s^{-1}$

$\qquad\qquad\qquad k_b(5000) = 5.2 \times 10^{14} \ cm^6 mol^{-2} s^{-1}$

While the k_b values for the two reactions are comparable at 5000 K, the dominant reaction involves M = H because initially the concentration of H_2 is far less than that of H.

A reaction time scale can be constructed by analyzing eq.(4.4.3). We set it up as a linear equation:

$$\lambda \equiv k_b[H][H] \quad \Rightarrow \quad \frac{d[H]}{dt} = \lambda[M]. \qquad (4.4.4)$$

Then, the time it takes to complete the reaction is approximately:

$$\tau_{chem} = \frac{1}{\lambda} \qquad (4.4.5)$$

This analysis, while approximate, can yield significant information. If the flow timescales are substantially faster than the chemical recombination timescales, the flow will remain frozen. Secondly, if the chemistry timescales are substantially

shorter than the flow timescales, the flow may be considered to remain in thermo-chemical equilibrium. Lastly, there is a region where the timescales are similar; here little can be claimed about the state of the gas other than that it is somewhere in between the frozen and equilibrium extremes. Using the rates in Table 15, the recombination time scales presented for the T, p conditions in Table 14 were calculated. The predictions for the LiH propellant using the laser parameters of the benchmark CO_2 laser system are as follows:

1. In the far field of the expansion, recombination will be insignificant.

2. Close to the base of the thruster, there will be some recombination of the Hydrogen in the propellant to its equilibrium value.

Thus, more work needs to be done to completely describe the state of the propellant at the thruster base as the gas expands away from it. A kinetic code is the answer, but it will not be constructed here. The frozen code *PROPLIH.FOR* or the equilibrium code *PROP.FOR* with the value of γ set to 1.22 can be used to calculate an expansion under either the frozen or equilibrium assumption. It should be emphasized that the principal objective of *PROP.FOR* is the estimation of 3-D expansion losses, and while *PROPLIH.FOR* can be used for that purpose, it is prohibitively costly for any but the largest computer time budgets at the present state of computing in 1990. Much can be learned about the effect of chemical reactions in a 1-D coding of the thruster conservation laws. An acceptable solution might be achieved if the chemistry is worked out in 1-D to estimate the frozen flow losses and calculate an efficiency η_{chem}, This, when multiplied with the expansion efficiency η_{expand} and all other system efficiencies will yield the desired final efficiency of the laser propulsion system.

Part 5: Real Gas Runs

Section 1. Equilibrium Runs

In the work of the original AVCO team which calculated the performance of an ideal 1-D thruster, the propellant was assumed to be H_2O vapor with $\gamma = 1.2$ While the fate of H_2O as a propellant is now questionable, due to the difficulty in igniting an LSD wave in it, the fate of the $\gamma = 1.2$ constitutive law is far safer. In 1988 at the Laser Propulsion Workshop held at Dartmouth College, Weyl and others at Physical Sciences Incorporated stated that although the emphasis had shifted to LiH from H_2O for a propellant, the $\gamma = 1.2$ constitutive law would also hold for LiH. The work of section 2 of this chapter yielded a $\gamma = 1.221$ for equilibrium LiH, and so the thrust performance calculations performed for an ideal gas with $\gamma = 1.2$ in chapter 3 are virtually identical to equilibrium LiH calculations. The difference in γ between the ideal runs and the equilibrium value was deemed small enough that a repeat of the calculations with the value of $\gamma = 1.221$ instead of $\gamma = 1.2$ would be unnecessary; these runs would have provided little new information.

Section 2. Expansion Profile for Frozen Runs

Having constructed a model for frozen LiH, the next task at hand is to generate the profile of the gas behind the LSD wave. The absorption model and the hydro-dynamics interior to the LSD wave are due to Physical Sciences, Inc. (hereafter called PSI). Behind the LSD wave, the gas expands to meet the hard wall boundary condition. Figure 4.5 shows the regions in the flow and the codes used to simulate them.

The PSI approach uses the wave-fixed coordinate system often used in the literature on detonations. The coordinate system used for computational simulation of the

Table 16: Compatibility of Ionization Model with PSI model of LSD Wave at the Chapman-Jouget Point for D=8500 m/s.

Quantity	PSI	Ion Model
$\rho\ (\frac{kg}{m^3})$	.1547	.1547
u (m/s)	3000	3000
c (m/s)	5500	5366
p (atm)	33	33
γ	(1.2)	1.35
T (K)	8480	8980

thruster is thruster fixed, and so the wave fixed coordinate system is translating at speed D away from the thruster base. In all runs performed by PSI, the computational domain begins just prior to the shock front and ends at the Chapman–Jouget point, at which the velocity of fluid equals its speed of sound in the wave fixed coordinates (Figure 4.7) The expansion wave is modeled using the joint assumptions of frozen chemical reactions and equilibrium ionization that are outlined in section 3. Compatibility between properties at the CJ point, where the PSI code terminates, and the Ion model begins is shown in Table 16, and pictured in Figure 4.6. The PSI coordinate system is shown in Figure 4.7.

In order to generate the expansion wave, it was easiest to work in the wave fixed coordinate system. Here, the CJ point is used as the entrance condition to the computational domain, which is the analogue of a 1-D tube. Piston-type boundary conditions are enforced on a surface which moves away from the CJ point at the constant speed D. The pressure, temperature and density at this piston point are the base conditions. The velocity at the piston is D in the wave fixed coordinate

system and therefore 0 in the vehicle fixed coordinate system.

The PSI wave is not equivalent to an ideal gas wave. This has a profound effect on the structure of the rarefaction wave behind it. For an ideal gas, At the CJ point, which is identical to the shock front we have the following results

$$u = \frac{D}{\gamma + 1} \quad , \quad c = \frac{\gamma D}{\gamma + 1} \tag{4.5.1}$$

For a detonation speed $D = 8500 \ m/s$, these equations predict that $u = 3863 \ m/s$ and $c = 4636 \ m/s$ at the CJ point when $\gamma = 1.2$. For $\gamma = 1.35$, the equations yield the values $u = 3617 \ m/s$ and $c = 4882 \ m/s$ The PSI values are substantially different. The higher speed of sound in the PSI model is the main cause of the difference. At the CJ point, in thruster fixed coordinates, we have that $u + c = D$. Since c is far greater in the PSI simulation than in a comparable ideal gas wave, the value of u is substantially reduced at the wave front as a result. These differences at the CJ point change the value of the pressure and density experienced at the base at the tail end of the rarefaction. For an ideal gas, the base pressure is computed from the CJ value by

$$p_{base} = \beta p_{CJ} : \quad \beta = \left(\frac{\gamma + 1}{2\gamma}\right)^{\frac{2\gamma}{\gamma - 1}} \quad (\gamma = 1.2 \Rightarrow \beta = 0.35) \tag{4.5.2}$$

It turns out that this value is virtually insensitive to changes in γ. For $\gamma = (1.4, 1.67)$ we find that the multiplier β is $(.340, .328)$. In the expansion wave modeled here, we obtain $p_{base} = 0.47 p_{CJ}$. Thus, the base pressure is about 50% of the CJ value for the real gas, while it is only 35% of the CJ value for an ideal gas.

This significant finding will be verified to be the effect of the difference at the CJ point and not an artifact of the chemistry model used in the expansion wave. The approach used will be to assume an ideal gas expansion with the PSI CJ conditions and compute the base pressure.

Again using the Riemann invariant method of construction for the expansion wave following the LSD wave, an ideal gas with $\gamma = 1.2$ and $\gamma = 1.35$ was studied with PSI's CJ conditions at the wave front: $u = 3000 \ m/s$ and $c = 5500 \ m/s$. The Riemann invariants, using eq. (2.1.1) and the convenient technique to switch to the always > 0 P, Q are:

$$J^+ = u + \frac{2c}{\gamma - 1} \equiv P$$
$$J^- = u - \frac{2c}{\gamma - 1} \equiv -Q$$

(4.5.3)

The case of $\gamma = 1.35$ will be shown here. At the wave front, the invariants are $(P, Q) = (34429, 28429) m/s$. In the expansion, Q is held constant and P is decreased until the condition u=0 is met. Here, $P = Q$ and this state is constant until the base is reached. We find the speed of sound at the base from

$$c_{base} = \frac{(\gamma - 1)Q}{2} = 4975 m/s$$

Since c is known at the wave front, the ratio of the speed of sound between the post expansion value and the CJ value is used to calculate the pressure at the end of the expansion, which is the base pressure. This is due to the isentropic relation

$$\frac{p_{base}}{p_{CJ}} = \left(\frac{c_{base}}{c_{CJ}}\right)^{\frac{2\gamma}{\gamma-1}} = 0.461$$

(4.5.4)

The pressure profile in the expansion computed for the case of an ideal gas with $\gamma = 1.35$ is compared with the ion model generated computationally in Figure 4.8. Agreement is very close, because the value of γ in the ion model is within 0.05 of the 1.35 value throughout the expansion. The ion model does not duplicate the discontinuous slope of the ideal data generated from the Riemann invariants, but the agreement in slope elsewhere is close.

When the case $\gamma = 1.2$ was run, $\frac{p_{base}}{p_{CJ}}$ was found to be 0.51 . Thus, when an ideal gas equation of state is assumed for the rarefaction using the CJ conditions from

88

the PSI code for the LSD wave, the pressure at the base is roughly insensitive of γ and is approximately 50% of the CJ value. The ion model also computes a pressure which is about 50% of the CJ value, and so it is consistent with the ideal gas result for these particular CJ conditions. The value of the pressure at the base is thus primarily due to the CJ conditions, and not an artifact of the particular gas model used in the rarefaction wave.

Section 3. Results in One Dimension

For these runs, the evaporated gas density prior to the passage of the LSD wave is $\rho_0 = 0.1 kg/m^3$ and the detonation speed achieved is $D = 8500 m/s$. The ideal gas thruster is assumed to operate at $\gamma = 1.2$, using the Taylor wave as the initial condition. The real gas thruster uses the ion model and the expansion profile generated by computer with it as the initial condition; the operating γ interior to the expansion is approximately 1.35. The main pulse duration of the laser is $\tau = 1\mu s$. The condition $t = 0$ corresponds to the initiation of the LSD wave. Figure 4.9 shows the base pressure as time is increased. This is called the core pressure because it would be the pressure experienced at the core of an axisymmetric thruster while the flow remained 1-D there. The core pressure is initially 11.5 atm for the ideal gas while it is 15.5 atm for the real gas using the ion model, so the real gas thruster acquires more impulse in the early stages than its ideal counterpart. After 20 microseconds, Figure 4.10 shows that the real gas thruster and the ideal have acquired about the same impulse, with the ideal thruster lagging behind by approximately 5%. In terms of the normalized impulse f, which is defined in eq. (2.4.5) the ideal gas thruster is superior, as shown in Figure 4.11. The slope $\frac{df}{dt}$ for the normalized impulse curves has decayed to approximately 0.05 for the real gas thruster at $t = 20\tau$ while the slope is 3 times as great for the ideal gas at $t = 20\tau$, indicating that in the future, the ideal gas value of the impulse will equal or better

89

the real gas. However, the performance of the real gas thruster is superior to the ideal gas thruster in the first 20 microseconds, which is due to the higher initial value of its base pressure. It is in the first 10 to 20 microseconds that the bulk of the impulse is acquired, favoring an LSD wave with the CJ conditions that provide for a low value of β as defined in eq.(4.5.2)

Conclusions

The gasdynamics of a thruster powered by laser supported detonation waves can be idealized as a one-dimensional flow, but this leads to estimates of thrust performance which are inadequate. Using the method of characteristics to describe the 1-D expansion, together with the assumption of zero pressure outside of the 1-D core flow yields excessively conservative thrust estimates. Computational simulation of the flow is essential in the range of Aspect Ratio (eq.(1.2.2)) $A < 40$, where the simplifying assumptions used in Chapter 2 predict a thrust efficiency below 60%. Computational simulation is especially important in the range $A < 24$ shown on Figure 3.17. The thrust efficiencies computed for $A = 10$ and $A = 20$ using the axisymmetric code *PROP.FOR* are 55% and 65%, respectively. The comparable estimates using the techniques of Chapter 2 are 21.7% and 41.6%. There are two significant conclusions which can be drawn from these computational solutions which were not obvious at the initiation of this research.

First, the operating Aspect Ratio for flight hardware need not be in the hundreds to achieve good expansion performance. Using laser beam sizes and pulse-durations which result in $A \geq 50$ yields performance which is close to the 1-D limit. Acceptable performance is achieved at $A = 24$. This finding leads to can change the way in which people think about a laser thruster. Small scale operation is possible. For a 1 cm thick LSD wave, the beam required to achieve $A = 24$ is indeed 24 cm in diameter, which is just under one foot. While this is still a big beam, it is far smaller in area than the 1 meter sized beams which are an eventual goal. Large payloads and lasers to drive them are the long term objective of the laser propulsion program, but to get off the ground, a small scale system, which is far less expensive than a large scale device, will also work.

91

The possibility of small scale operation will offer designers increased flexibility. The Aspect Ratio is dependent on fundamental quantities such as laser pulse duration, laser beam diameter, and propellant chemistry, each of which has to be tailored precisely to achieve the best performance for the money. Operation at small Aspect Ratio may be unavoidable, but it is not catastrophic to do so, and may even prove to be advantageous. Also, it simply may not prove to be feasible to tailor and propagate a uniform laser beam of the size required to operate at high Aspect Ratio. To reliably ignite and successfully propagate the LSD wave, the laser spot may well need to be kept small, and so the thrust performance will suffer somewhat, but not catastrophically.

Second, the data generated at laboratory scale at small Aspect Ratios can now be rationally scaled up using the results of *PROP.FOR* and *SPOT.FOR*. Because the laboratory equipment used is of smaller scale than that expected for flight hardware, The impulse measured by these systems is often far below that which would be received by a 1-D system. And, as shown in Chapter 3, Section 5, the impulse received by a target which is larger than the beam diameter is greater than the impulse received when the target is the same size as the beam, but still less than the 1-D value. Exploitation of this in the laboratory will yield better results. In cases where operation at low Aspect Ratio where $A < 10$ is unavoidable, the use of a skirt nozzle to contain the gas has been shown to provide much better performance. The 45° degree skirt simulated here also increases the area against which the gas can push the vehicle forward, which is quite useful.

A more detailed discussion of the first conclusion is in order. The relationship between the absorption depth of the laser in the propellant to the length of propagation of the LSD wave will be established below, and then connected to the desirable beam diameter through the Aspect Ratio. In reality, the laser flux required to initiate an

LSD wave is substantially greater than the flux required to sustain one. Initiation of an LSD wave involves the buildup of ionization, density and gasdynamic pressure at the LSD wave front and is achieved at a considerable cost of energy. Once the LSD wave has been initiated at a high flux, the best way to recover this initiation energy penalty is to process a sizeable amount of gas at the lower flux required to maintain the wave. This is achieved by driving the LSD wave through the gas over a distance which is several times greater than the absorption depth. The absorption depth has been calculated to be 0.1 cm in LiH by Physical Sciences for the laser flux and ablated gas density at which the system will likely operate. For this particular absorption depth, then, an LSD travel distance of from 0.5 cm to 1 cm would yield good performance. To expand the gas with 65% efficiency then, operating at $A = 24$, the laser spot diameter required would be from 12 cm to 24 cm.

At the present time, it is believed that the first flight vehicle to use laser propulsion will be powered by a laser designed for other purposes. Time from this laser oscillator will be borrowed for proof of concept flight testing. Levitation or launch of even a 1 kg object would be a significant achievement, if one considers that Robert Goddard's first chemical rockets were only a few feet long. This vehicle may well operate with a small Aspect Ratio. Later vehicles will strive for 1-D performance, and this will be achieved at a far lower Aspect Ratio than the worst case calculations of Chapter 2 predict.

If the propellant Lithium Hydride is used, it has been shown to be quite effectively modeled in the equilibrium state as an ideal gas with $\gamma = 1.2$. Nevertheless, this propellant will exhibit frozen flow losses which are substantial, due to the fact that in the evaporated state the gas is not LiH molecules but rather a mixture of Li atoms and H_2 molecules. The laser must supply the 4.6 eV per H_2 bond if the propellant temperature is to be raised to the high values desired for a high I_{sp}.

This frozen loss is in the range of 20% to 40% of the total energy input. Still, the high rate of recombination of the collision in which 3 Hydrogen atoms collide to form H_2 + H with a release of energy shows that some of the frozen losses will be recovered. Recovery of frozen losses requires time, favoring a longer timescale in the flow. However, the available laser pulse duration is not always that flexible for a given oscillator. The Induction Linac Free Electron Laser, according to ref[1], p.125, presently has achieved a pulse width of 15 nanoseconds, which is 67 times shorter than the desirable pulse of 1 microsecond. In this case the propellant would be well modeled as frozen. The Radio Frequency Linac Free Electron Laser (RF Linac FEL) produces still shorter pulses, according to ref[1], p.125, the duration is 20 picoseconds. Perhaps by combining several of these pulses in a macro pulse, a quasi-steady delivery of energy to the propellant might be achieved over a few microseconds, but in general suitability of the RF linac FEL for Laser Propulsion is unlikely. Use of FEL's will result in frozen propellant operation. The longer pulse of the CO_2 laser will result in some recombination.

Another important finding of Chapter 4 is that the Chapman-Jouget condition which is achieved in the propellant has a substantial effect on the profile of the expansion behind the wave front that leads to the still, high pressure gas condition at the thruster base. The greater the base pressure achieved, in general, the better the thruster. The higher base pressure in a real gas wave than in an ideal gas wave is due to the fact that the ideal gas has a higher kinetic energy of mean motion at the time of blast onset than its real counterpart. In the long run, this kinetic energy is recovered as thrust, but there is considerable merit acquiring the blast impulse quickly, before the mechanisms of viscosity, heat conduction, radiation, and of course, lateral expansion are able to rob the flow of a sizeable amount of energy. Even though the latter loss mechanism is the prime concern of this thesis,

if each of the other three costs the flow just 5% of its thrust, that is 15% and a lot of thrust.

Time accurate simulation of axisymmetric flow in the blast phase of a LSD Wave thruster has been achieved for an inviscid and ideal gas blasting into near vacuum ambient condtions. The vehicle simulated is a 45° semivertex angle cone with the LSD launched from its base in the code *PROP.FOR*, and a disk in the code *SPOT.FOR*, which is really a simple extension of the cone code. The effect of lateral blast is significant. The flow must be directly simulated to correctly estimate it. The final achievement is the code *PROPLIH.FOR*, which simulates the flow of chemically frozen Lithium Hydride in ionization equilibrium in 1-D, 2-D, and 2-D axisymmetric flow. Even though it was constrained to 1-D operation by its wildfire-like consumption of computer time, the code *PROPLIH.FOR* contributed significantly to the research, because the extreme sensitivity of base pressure and 1-D thruster performance on the CJ conditions was established.

At this writing, there is good news and bad news to report on the status of laser propulsion. The Isp's of 800-1000 sec reported by Hale[9] and Reilly[10] in July, 1989 are the good news. The bad news is that these experiments were performed at small length scales, and that initiation of the LSD wave at large length scales, with a nearly plane detonation front, has yet to be achieved. In the author's opinion, the best system thus far demonstrated in hardware is Kare's breakdown scheme, shown in Figure 1.4. Even this technique is not fully debugged, because the plasma cores emanating from each focal point in the array do not merge into a plane front, but this is perhaps the seed of another dissertation. For the ablation-LSD wave method due to Kantrowitz under study here, it is virtually certain that planar initiation will be achieved on a repeatable basis if a laser beam of sufficient power and and coherence can be built.

95

The advantage of Kantrowitz's concept over all others is that it permits the design of exceptionally simple and cheap vehicles. The disadvantage is that it requires a large planar LSD wave to work. Should a vehicle be built which is based on Kare's method or some other method, lateral blast of the propellant will still have to be reckoned with. The Blast Wave Aspect Ratio will again be formed, only using a different set of system parameters, and the code *PROP.FOR* or a variant thereof may again be used.

Appendix 1.

Sample Thrust Calculation for a Two Pulse Laser Thruster In each millisecond, the system will go through the following cycle. and the cycle will be repeated at 1000 Hertz.

> 10 microsecond ablation pulse
> 5 microsecond expansion interval
> 1 microsecond main pulse
> 984 microsecond blast of propellant

We assume that the total impulse due to blast and detonation phases will be 5 times that of just the detonation phase. This is due to the force exerted on the base of the thruster by the hot expanding gases in the aftermath of the LSD wave.

Detonation Base Pressure: 10 atm = $10^6 \mathrm{N/m^2}$

Detonation Total Impulse per unit area: 1 $\mathrm{Ns/m^2}$

Total Impulse per cycle per unit area: 5 $\mathrm{Ns/m^2}$

Total Impulse in 1000 cycles: 5000 $\mathrm{Ns/m^2}$

Average Pressure over 1 second: 5000 $\mathrm{N/m^2}$

Since a 500 kg mass has a weight of about 5000 N, A pulsed laser system which performs as above could levitate a 500 kg thruster with a 1 $\mathrm{m^2}$ beam. The power required to do this would make the laser very costly, but the point is that with a reasonable base pressure of 10 atm and a sufficiently high pulse repetition rate, the force that a laser thruster can generate is quite high.

Appendix 2. Non-Dimensionalization Procedure for the Axisymmetric Euler Equations

The system parameters are used to non dimensionalize the space and time variables.

$$T = \frac{t}{\tau} \qquad\qquad \frac{\partial}{\partial t} = \frac{1}{\tau}\frac{\partial}{\partial T}$$

$$Z = \frac{z}{D\tau} \qquad\qquad \frac{\partial}{\partial z} = \frac{1}{D\tau}\frac{\partial}{\partial Z}$$

$$R = \frac{r}{D\tau} \qquad\qquad \frac{\partial}{\partial r} = \frac{1}{D\tau}\frac{\partial}{\partial R}$$

$$V = \frac{v}{D} \qquad\qquad \frac{v}{r} = \frac{V}{R\tau}$$

The reference values for (ρ, u, e) will be (ρ_r, D, e_r), Using these we define the non-dimensionalizing matrix $\mathbf{N}$ via:

$$\mathbf{N} = \tau \times \mathbf{diag}(\ \frac{1}{\rho_r},\ \frac{1}{\rho_r D},\ \frac{1}{\rho_r D},\ \frac{1}{e_r})$$

Beginning with the Axisymmetric Euler Eq.

$$
\begin{bmatrix} \rho \\ \rho u \\ \rho v \\ e \end{bmatrix}_t
+
\begin{bmatrix} \rho u \\ \rho u^2 + p \\ \rho uv \\ (e+p)u \end{bmatrix}_z
\begin{bmatrix} \rho v \\ \rho uv \\ \rho v^2 + p \\ (e+p)v \end{bmatrix}_r
= -\frac{v}{r}
\begin{bmatrix} \rho \\ \rho u \\ \rho v \\ (e+p) \end{bmatrix}
$$

or, more simply

$$U_t + F_z + G_r = -\frac{v}{r}S(U)$$

The substitutions for r, z, t ,and v together with matrix multiplication by $\mathbf{N}$ yield:

$$\mathbf{N}\left[\frac{1}{\tau}U_T + \frac{1}{D\tau}F_Z + \frac{1}{D\tau}G_R\right] = -\frac{V}{R\tau}\mathbf{N}S(U)$$

From which the result is a fully non-dimensional set.

$$
\begin{bmatrix} \frac{\rho}{\rho_r} \\ \frac{\rho}{\rho_r}\frac{u}{D} \\ \frac{\rho}{\rho_r}\frac{v}{D} \\ \frac{e}{e_r} \end{bmatrix}_T
+
\begin{bmatrix} \frac{\rho u}{\rho D} \\ \frac{\rho u^2 + p}{\rho D^2} \\ \frac{\rho uv}{\rho D^2} \\ \frac{(e+p)u}{e_r D} \end{bmatrix}_Z
+
\begin{bmatrix} \frac{\rho v}{\rho D} \\ \frac{\rho uv}{\rho D^2} \\ \frac{\rho u^2 + p}{\rho D^2} \\ \frac{(e+p)u}{e_r D} \end{bmatrix}_R
= -\frac{v}{RD}
\begin{bmatrix} \frac{\rho}{\rho_r} \\ \frac{\rho}{\rho_r}\frac{u}{D} \\ \frac{\rho}{\rho_r}\frac{v}{D} \\ \frac{e+p}{e_r} \end{bmatrix}
$$

Notes and References

Citations:

[1] SDI Technology, Survivability, and Software. Office of Technology Assessment. Princeton University Press, 1988. unclassified version. p 151.

[2] It is probably easier because the propulsion target is benign whereas an incoming RV certainly is not.

[3] Kantrowitz, Arthur. "Propulsion to Orbit by Ground Based Lasers," Astronautics and Aeronautics 10(5),74 (1972).

[4] Razier, Yu P. "Heating of a Gas by a Powerful Light Pulse" Soviet Physics JETP, Vol. 21, No. 5, 1965, pp. 1009-1017.

[5] Kare, Jordin. Laser Supported Detonation Waves and Pulsed Laser Propulsion. Presented at 17th International Symposium on Shock Waves and Shock Tubes. July, 1989.

[6] Kantrowitz, Arthur. "Laser Propulsion to Earth Orbit: Has its time Come?" Proc. SDIO/DARPA Workshop on Laser Propulsion, LLNL, 7-18 July 1986 V. 2 pp. 1-12

[7] Rollins, Lo, Resendes and Weyl,"Issues for Laser Propulsion Progress in Theory, Modeling, and Experiment." Presented to: Workshop on Laser Propulsion, Lehigh University, 21-22 July 1989. Physical Sciences, Research Park, P.O. Box 3100, Andover, MA 01810- 7100

[8] Hyde, Roderick A. "One Dimensional Modeling of a Two-Pulse LSD Thruster" Proc. SDIO/DARPA Workshop on Laser Propulsion, LLNL, 7-18 July 1986 V. 2 pp. 79-88.

[9] Hale, Mike. Spectra Technology Lehigh Worksop Report,1989.

[10] Reilly, Dennis. AVCO Everett Lehigh Workshop Report, 1989.

[11] CJ Analysis using Rayleigh lines and Hugoniot curves shows that in v-p space, the Rayleigh line slope $(dp/dv)_R$ decreases with increasing detonation speed. Its slope is always negative, so it gets steeper with increasing detonation speed. The positive curvature of the Hugoniot Curve $(d^2p/dv^2)_H$ means that there is only one slope which touches a given H curve at one point. In order for a double intersection to occur, which corresponds to a strong, high pressure solution and a weak, low pressure solution, the Rayleigh line must have a slope which is steeper than that for a single intersection. thus the detonation speed must be faster for a double intersection . Assuming total absorption of the incident flux, an LSD's Hugoniot is fixed, leaving the CJ speed as the minimum.

[12] Chapman, Douglas-Hamilton, and Reilly. "Investigation of Laser Propulsion", Avco Research Report, V.1 Nov. 1977.

[13] Thompson, Compressible Fluid Dynamics. New York, McGraw Hill, 1971.

[14] Leipmann & Roshko, Elements of Gasdynamics. New York, Wiley, 1957.

[15] Fickett and Davis, Detonation. Berkeley, University of California Press, 1979. ISBN 0-520-03587-9 Stanford Library: Engineering QC 168.85 .D46 .F53 ENG

[16] Schmalz, R.F. New self similar solutions for the unsteady one-dimensional expansion of a gas into a vacuum. Phys Fluids v.28. (9) Sept 1985, p 2923

[17] Taylor, G.I. The Dynamics of Combustion Products behind Plane and Spherical Detonation Waves. Proc Roy Soc. **A 200** 235-247 (1950)

[18] Gordon and McBride, Computer Program for the Calculation of Complex Chemical Equilibrium Compositions, Rocket Performance, Incident and Reflected Shocks, and Chapman-Jouget Detonations. NASA SP-273, Interim Revision, March 1976.

[19] Jumper, Jackson, Coulick, McKee, Bohn, and Crawford. Mechanisms for Thermally Enhanced Target Coupling by Repetitively Pulsed Lasers. Journal of Thermophysics, v.1 (3), July, 1987.

[20] Steger, J.L. and Warming, R.F. Flux Vector Splitting of the Inviscid Gasdynamic Equations with Applications to Finite-Difference Methods. Journal of Computational Physics, v.40, pp 263,293(1981).

[21] MacCormack, R. Numerical Computation of Compressible Viscous Flow. This text was used as the course notes for the Stanford CFD series, AA214b & AA214c, 1988; written 1986.

[22]: Courant and Friedrichs, Supersonic Flow and Shock Waves. ew York, Springer-Verlag, 1977,c1948.

[23] Sedov, L.I. Similarity and Dimensional Methods in Mechanics. 4th ed. GITTL, Moscow, 1957. Eng. Transl., Academic Press, New York, 1959. : The Original Russian manuscript was used by the author.

[24] Korobienkov, V.P. Problems in the theory of point explosion in gases. Procedings of the Steklov Institute of Mathematics #119, 1973. American Mathematical Society, 1976. Stanford:Math, QA 1 A413 v.119.

[25]. Note These solutions required 1000 sec on a *Cray Y-MP*.

[26] Stull, Prophet, et. al. JANAF Thermochemical Tables. U.S. National Bureau of Standards, NSDRS-NBS 37, 1971.

[27] Weyl, Guy. Private Communication.

[28] Strang, Linear Algebra and its Applications. Academic Press, New York, 1976,1980.

[29] Gruschka and Wecken, Gasdynamic Theory of Detonation. Gordon and Breach Science Publishers, Inc. New York, 1971.,

[30] Vincenti and Kruger, Physical Gas Dynamics. New York, Wiley, 1965.

[31] Baulch, Drysdale, Horn, Lloyd. Evaluated Kinetic Data for High Temperature Reactions. London, Butterwoths. Stanford: Chemistry QD 502.E85 v.1

[32] Vargaftik,N.B. Tables of the Thermophysical Properties of Liquids and Gases. 1975, Hemisphere Publishing Corp., Washington-London.

Background References not Cited:

Bdzil, J.B. Steady-state two-dimensional detonation. J. Fluid Mech (1981) v.108, pp.195-226.

Emery, Dahlburg, and Gardener, The Rayleigh-Taylor insatbility in ablatively accelerated targets with 1,1/2, and 1/4 micrometer laser light. Phys Fluids, v.31 (5), May 1988.
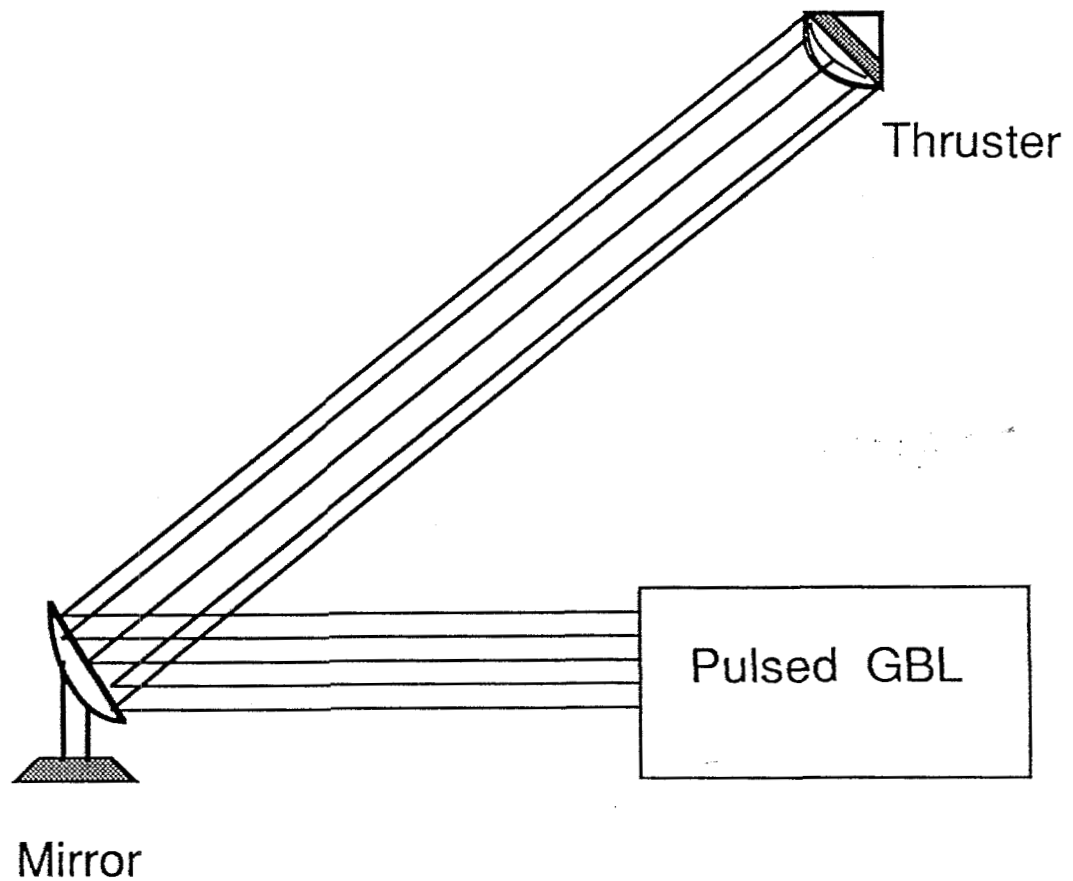
Figure 1.1   Overall Concept of Laser Propulsion

This application of pulsed Ground Based Lasers (GBL's)
was advanced by Kantrowitz in 1972.   Pulsed laser energy
is directed from the ground to a thruster which is
coated with an ablative propellant. Buildup of exhuast
gas in the beam path is avoided because there is a
comparatively long time between pulses. Unlike a
chemical rocket, the energy of propulsion is remotely
supplied.
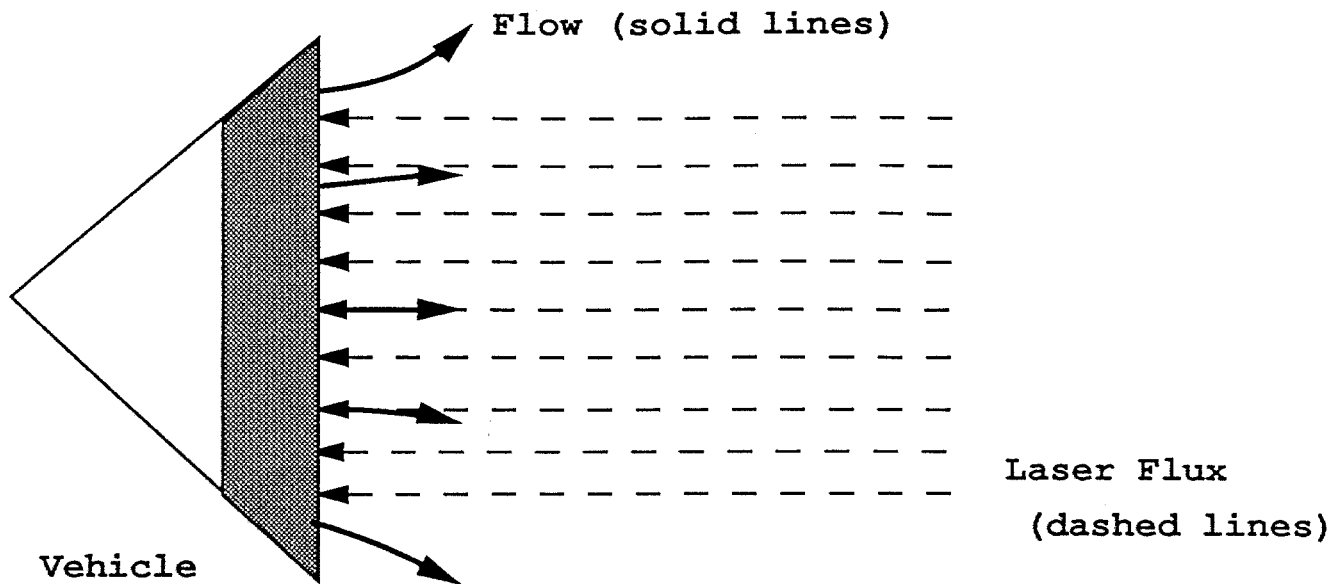
Figure 1.2 Direct Ablation Method

This is the most straightforward approach to laser
propulsion. However, the Isp that can be achieved is not
expected to exceed that for a chemical rocket. Direct
transmission of the laser to the propellant surface on
the vehicle causes propellant to be ablated and ejected
at high speed, in the range of 3-4 km/sec, yielding Isp's
of from 300 - 400 sec. The advantage of this system is
its energy efficiency and design simplicity.
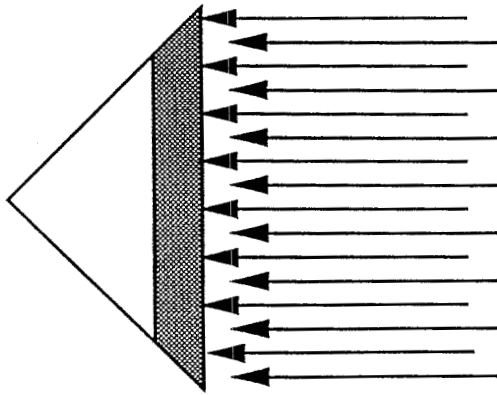
1. Ablation

Use Moderate Power.
Laser Boils Gas off
the Surface.
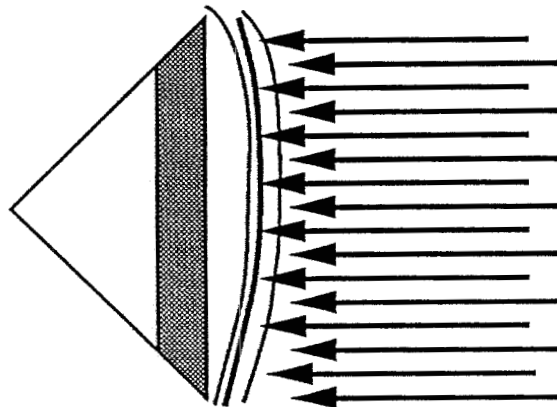
2. Detonation

Use High Power.
Laser Driven Detonation
Wave superheats the
ablated gas.

D : 5 - 10 km/sec
Isp : 500 - 1000
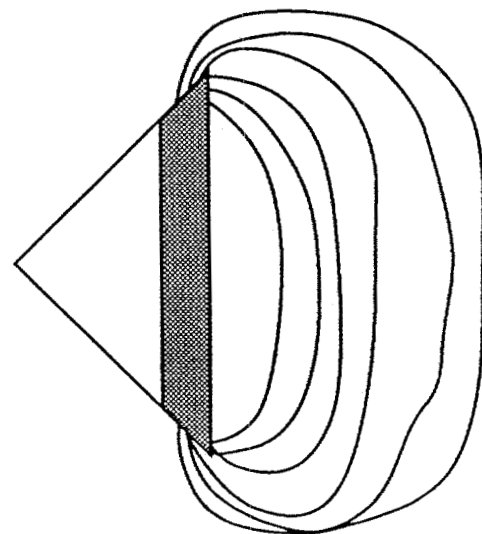
3. Blast

Laser Off.
Hot gas expands and
generates much more
thrust: Up to 8.5 x
(Detonation thrust).

**Figure 1.3   Double Pulse Laser Propulsion Technique
Under Investigation**

The Isp of this system is higher than the Isp of a
direct ablation system, because the energy per unit
mass of propellant is greater.
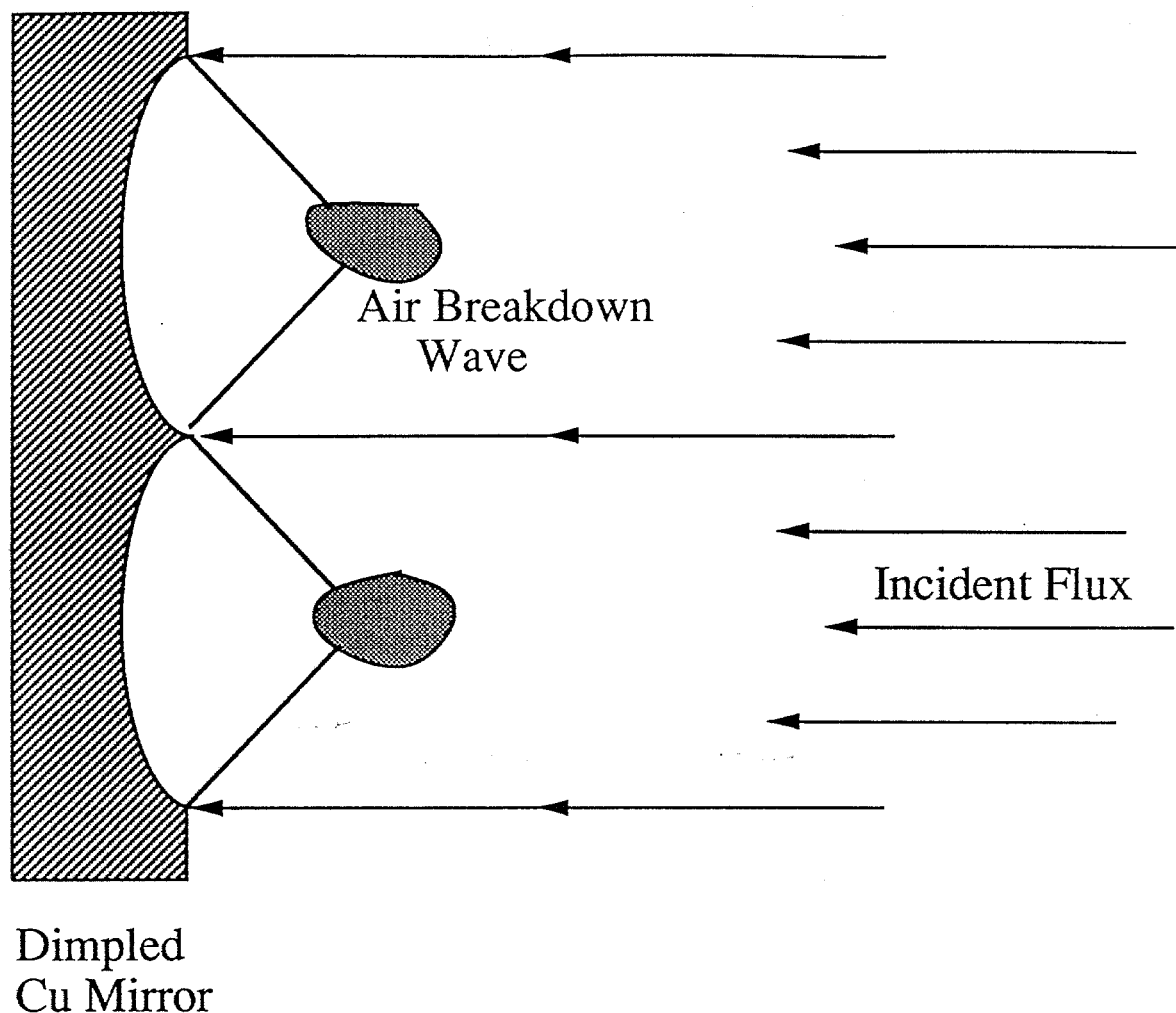
Figure 1.4 Kare's Breakdown Scheme in Air.

Kare at LLNL uses a Copper Mirror to focus the incident
plane wave of IR light to a point. At the focus, the flux
is strong enough to initiate an LSD wave in air,
overcoming a significant obstacle to a workable system.
The dimples are many in number, about 0.1 cm in diameter,
and hexagonally packed on the copper surface. Other
investigators have suggested a single mirror to
concentrate the flux; a major advantage here is that
each dimple acts independently of the others, yielding
a robust system.
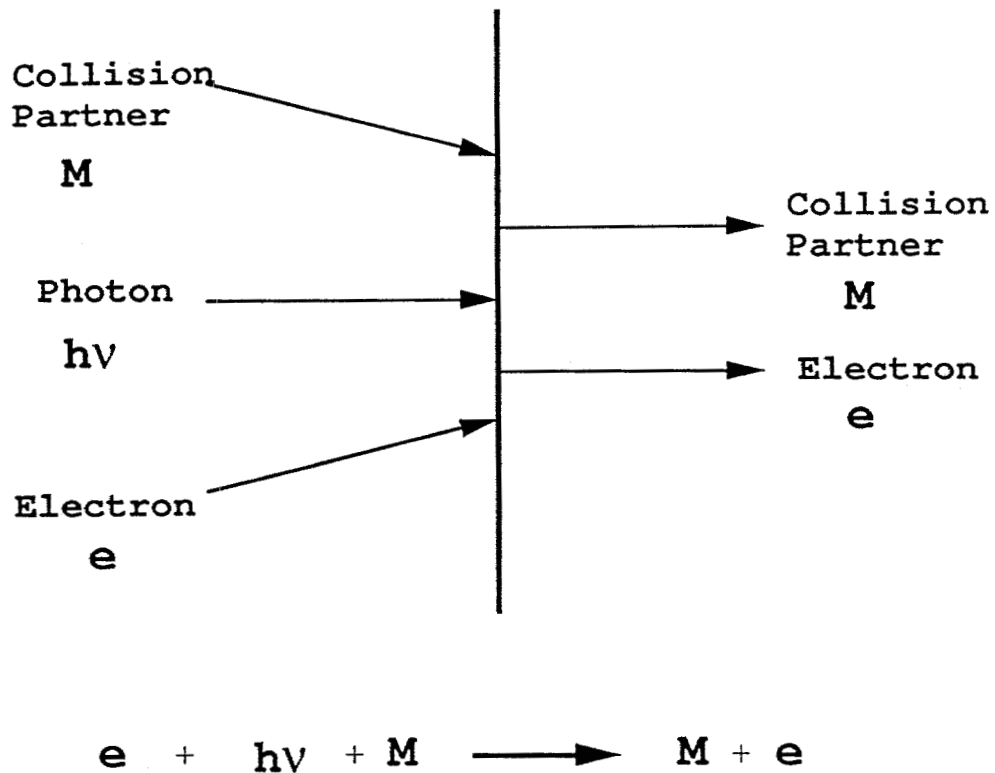
Figure 1.5   Inverse Brehmstrahlung.

This is one of the principal mechanisms by which laser energy is absorbed within the LSD wave. Here the energy of the photon is absorbed by the electron and a collision partner. The photon is annihilated in the collision, and the collision partner insures the conservation of momentum.

$$\rho$$

Constant
State

Gas
Expands

D

Ablated
Gas

Φ

X

Absorption
Front

Parameters
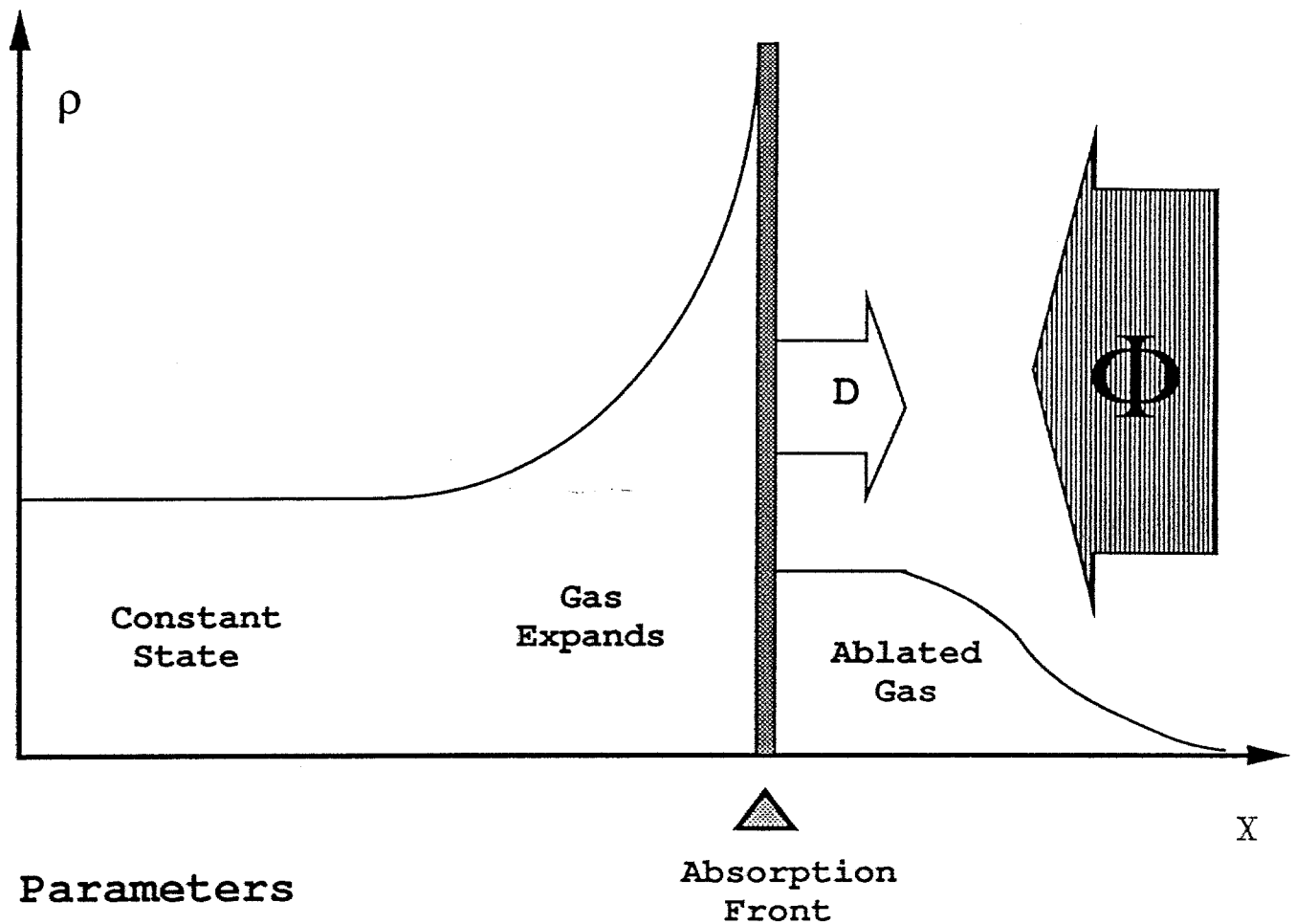
Main Pulse Laser Flux	$\Phi \sim 10^7 \ W/cm^2$
Ablated Gas Density	$\rho_0 \sim 0.1 \ kg/m^3$
Main Pulse on Time	$\tau \sim 1 \ \mu sec$
Detonation Speed	$D = \left[2(\gamma^2 - 1) \Phi/\rho_0 \right]^{1/3} \sim 10 \ km/sec$

Figure 1.6   Laser Supported Detonation Wave

Pictured shcematically is a 1-D LSD wave. Gas is
superheated by absorption of the incident laser flux.
The equation for the detonation speed D is due to
Razier.
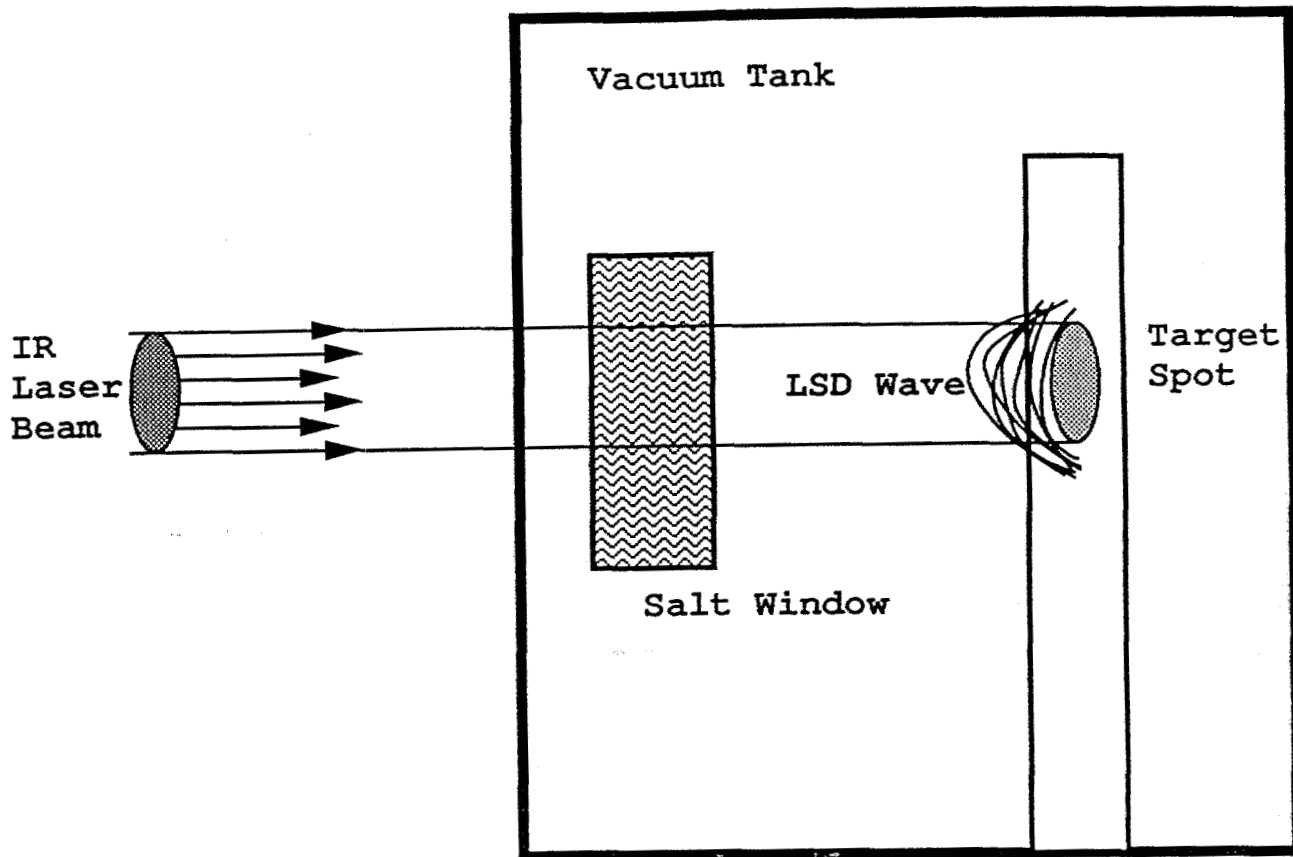
Figure 1.7 Experimental Set Up

Laser Propulsion has been tested by a number of
investigators in this manner. An infared laser, often
using CO_2 as the gain medium, is used as the light source.
Introduced into an evacuated test chamber, the beam
drives an LSD wave or, in other cases, directly ablates
propellant. In all experiments thus far reported, the
length and time scales of the experiment are different
from those expected in flight. Use of non-dimensional
scaling parameters such as the aspect ratio A defined
in eq. (1.2.2) makes it possible to compare computer
results with experimental results.
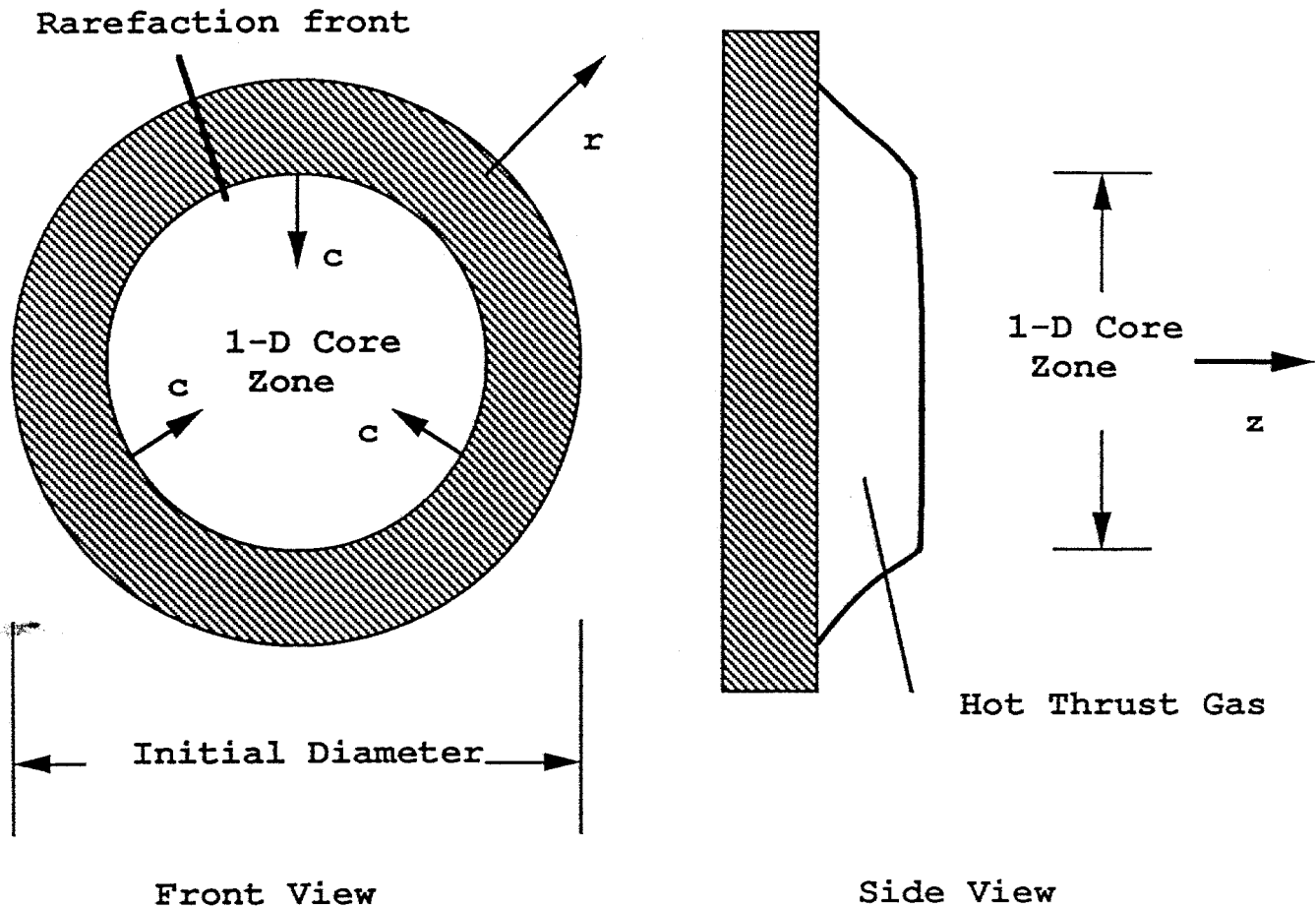
Figure 2.1 Circular Thruster and Rarefaction Wave

The flowfield is has a one-dimensional core flow which
diminishes in size with time. For a circular thruster,
the flow on the base is one dimensional inside a circular
rarefaction wave which propagates inward at the local
speed of sound.
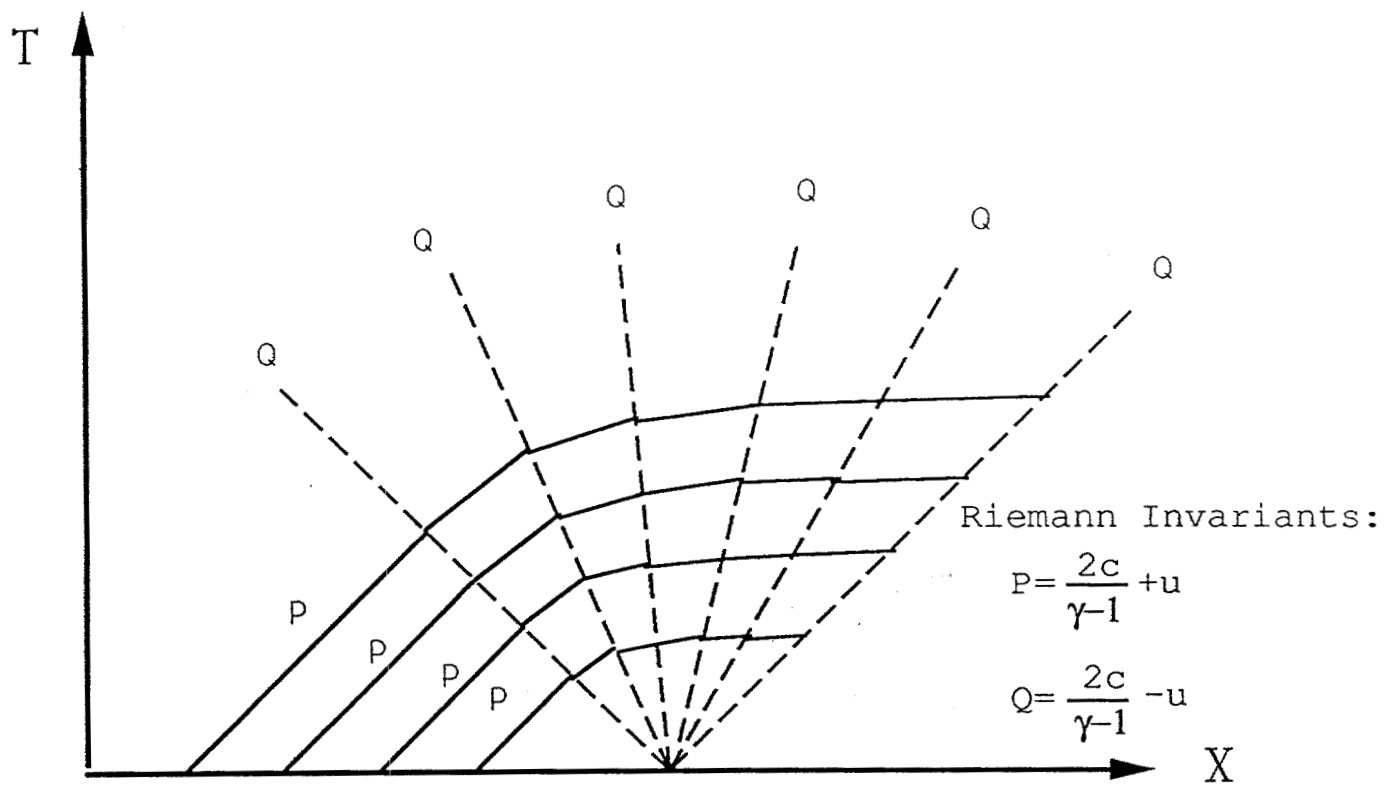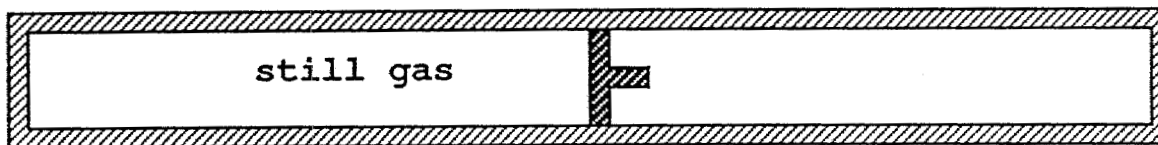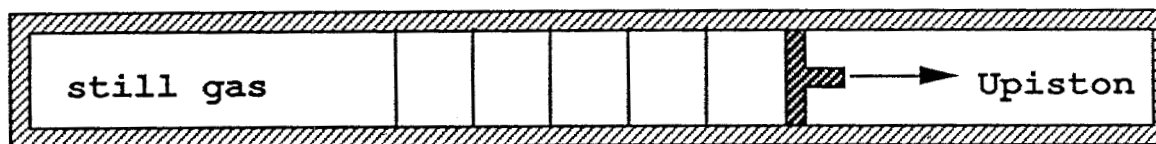
Figure 2.2 Method of Characteristics for the Centered Rarefaction Wave: an Initial-Boundary Value Problem.

This flow is simple enough to be used to illustrate the method of characteristics. The initial condition behind the piston is a still gas, and so P=Q. At time 0, the piston is withdrawn at a constant specified speed Upiston. The origin of the (x,t) space is a singular point, from which emanate Q characteristics. Due to the initial conditions, the value of P does not change throughout the solution until the Q trajectory at the far left reaches the endwall.
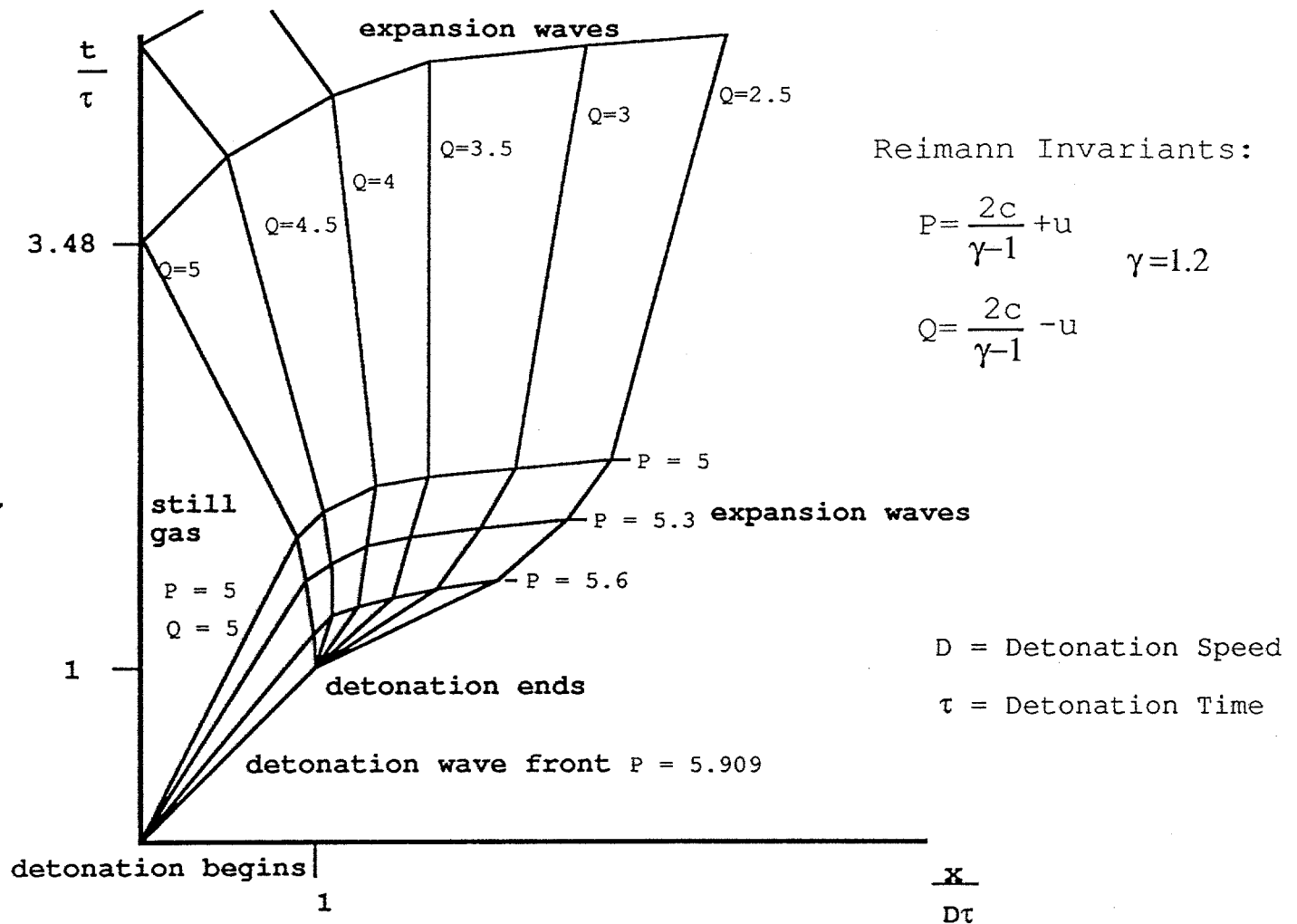
Figure 2.3 x-t Diagram for Detonation and Blast

Unlike the centered rarefaction wave, the characteristic
map of the flow in laser propulsion has two singular
points. At the origin, the LSD wave has just started to
propagate, leaving behind it a P rarefaction fan in which
the flow velocity is decreases from its wave front value
to zero. When the laser is turned off, at (1,1), a new Q
rarefaction fan begins. The solution on the base surface
$x/D\tau = 0$ thus depends on the interaction between the two
fans. Using the method of characteristics to construct
the field, the Reimann Invariants P and Q are traced
along the rays with slopes dx/dt=u+c for P and dx/dt=u-c
for Q. Finally, note the large still gas region at the
base surface. Information that the laser has been turned
off does not reach the base until t=3.48 τ.

Since at the end of detonation, $T \, (= t/\tau) = 1$, we have a normalization factor I(1) for the impulse, which is the product of the base pressure at time 0, called p_{0b}, with the base area and the detonation time τ.

$$I(1) = p_{0b}\tau \int_{base} dA \qquad (3.4.5)$$

The normalized impulse is then $f(T) = I(T)/I(1)$ and its development curve is traced in time. Often of interest is the core base pressure, also called the centerline base pressure. A good measure of the quality of the calculation is the agreement between the computational simulation for the core pressure with the solution for a 1-D thruster provided by the method of characteristics. Enhanced solution quality is achieved by the 1-D core routine until $T = 3.48\tau$. After that time, only the finite difference algorithm can be used. The agreement continues until the rarefaction wave from the outer edge of the thruster reaches the core, at which time the core pressure decays much faster than the 1-D solution.

Impulse curves for a variety of vehicle aspect ratios are given in Figure 3.15. In additon, core pressure plots are provided in Figure 3.16. The impulse values predicted by this code are much greater than those achieved via the worst case assumptions used in Chapter 2, as can be seen when the thrust efficiency curve is generated from the data. The thrust efficiency is defined by

$$\eta_T = \frac{\text{Axisymmetric Impulse}}{1 - \text{D Impulse}} = \frac{f_{ax.}}{f_{1-D}} \qquad (3.4.6)$$

These CFD calculations, unlike their 1-D counterparts, are constrained by the availability of computer time, and so the efficiency is often truncated at $T = 10\tau$ or 20τ. Ideally, the calculations are terminated for a given run when the impulse no longer continues to develop due to expansion. For small aspect ratios this phenomenon occurs quite early. A check of the solution is made for the slope of the impulse curve to discontinue the calculation, yielding dI/dT. The solution is terminated at

T_{stop} either when the impulse curve has rolled over, or when the budgeted computer time, T_{budget} is reached, whichever comes first. We have:

$$T_{stop} = min \left(T : \frac{dI}{dT} < .01, \ T_{budget} \right) \tag{3.4.7}$$

A much rougher estimate of the thrust efficiency is then the truncated version at $T = 10\tau$.

$$\eta_{T \ (10\tau)} = \frac{f_{ax.}(10\tau)}{f_{1-D}(10\tau)} \tag{3.4.8}$$

When $A < 24$, this quantity is generally considered to be sufficient for engineering purposes, and is plotted in Figure 3.17. A converged impulse is truly calculated only when the solution is terminated due to the decay in impulse aquisition– $\frac{dI}{dT} \rightarrow 0$ – that occurs in the range of from $4\tau - 50\tau$. Again, this is no problem for vehicle aspect ratios $A < 16$, but it becomes very costly as A is increased above these values.

Part 5. Experimental Scale Up. SPOT.FOR and Results.

One of the prime objectives of this research has been the scale up of experimental data. Figure 3.18 shows a typical laboratory set-up for a laser blast experiment. The target is a disk, either made of the ablative propellant material or coated with it. The laser spot diameter is smaller than the target diameter. Along the target surface, then, there is a great deal of extra area to push against. Impulse is measured ballistically, the same way that rifle bullet impulse is measured, using the elementary mechanics of the simple pendulum. The momentum imparted to the target impels it tangentially on its pendulum support, so the amount of vertical displacement achieved indicates the initial velocity of the target. The mass differential is measured with a balance.

For these runs, the system parameters were changed to correspond to runs performed at AVCO by D. Reilly. and are listed in Table 11. While the

Table 11: AVCO System Data Base for SPOT.FOR Simulations

τ: Laser On Time	50 ns
Laser Spot Diameter	0.33 cm
Target Diameter	1 cm
Propellant	Lithium Hydride
Energy Fluence	20 J/cm^2
D: LSD Speed	10 km/sec (assumed)

system parameters in this case are far different from those expected for a thruster, the dimensionless aspect ratio is $A = 6.66$ when the data in Table 11 is used, so this class of flow geometry is of small aspect ratio and must be simulated by computer to obtain accurate results. With initial conditions modified for a smaller LSD wave diameter than the vehicle diameter, the code $PROP.FOR$ was used to generate the

data. Again, the Aspect Ratio of the LSD wave is an important parameter which determines the degree of one-dimensionality in the flow, and a second parameter, Z, which is the ratio of the target diameter to the LSD diameter comes into play.

$$Z = \frac{\text{Target Diameter}}{\text{LaserSpotDiameter}} \qquad (3.5.1)$$

Figure 3.18 also illustrates these quantities graphically and Figure 3.19 shows impulse development for Z=1,2,3,4, and 6 for an aspect ratio of 6.15. This value of A was chosen because the scale-up experiments at AVCO are expected to be in the range of A=4-10. The chief finding is that the impulse received by the thruster is increased by up to 35% with increasing Z. The Impulse Advantage,Υ, is defined as the increase in impulse received by a large target over a conventional target.

$$\Upsilon(A, Z) = f(A, Z)/f(A, 1) \qquad (3.5.2)$$

For A=6.15, in Figure 3.20 the Impulse advantage is plotted as Z is varied, yielding a peak figure of 1.35, which is the origin of the 35% figure quoted above.

As expected, the extra target area leads to improved thrust performance. The limiting value of impulse for a 1-D thruster at 10τ is $f = 5.9$, and so all curves up to Z=6 are bounded from above by the 1-D impulse development curve. Note from Figure 3.20 that

$$Z \to \infty \qquad \Rightarrow \qquad \frac{d\Upsilon}{dZ} \to 0 \qquad (3.5.3)$$

In fact, we see that as Z is increased from 4 to 6, the value of Υ hardly increases; so the effect is finite in extent. Further increase of Z above 4 leads to little increase in f. Based on the convergence of the impulse development curves in Figure 3.19, the assertion that

$$\text{For all}(A, t): \qquad \lim_{Z \to \infty} f(A, Z, t) < f(\infty, 1, t) \qquad (3.5.4)$$

57

Figure 2.4 Core Base Pressure vs. Time for 1-D Thruster
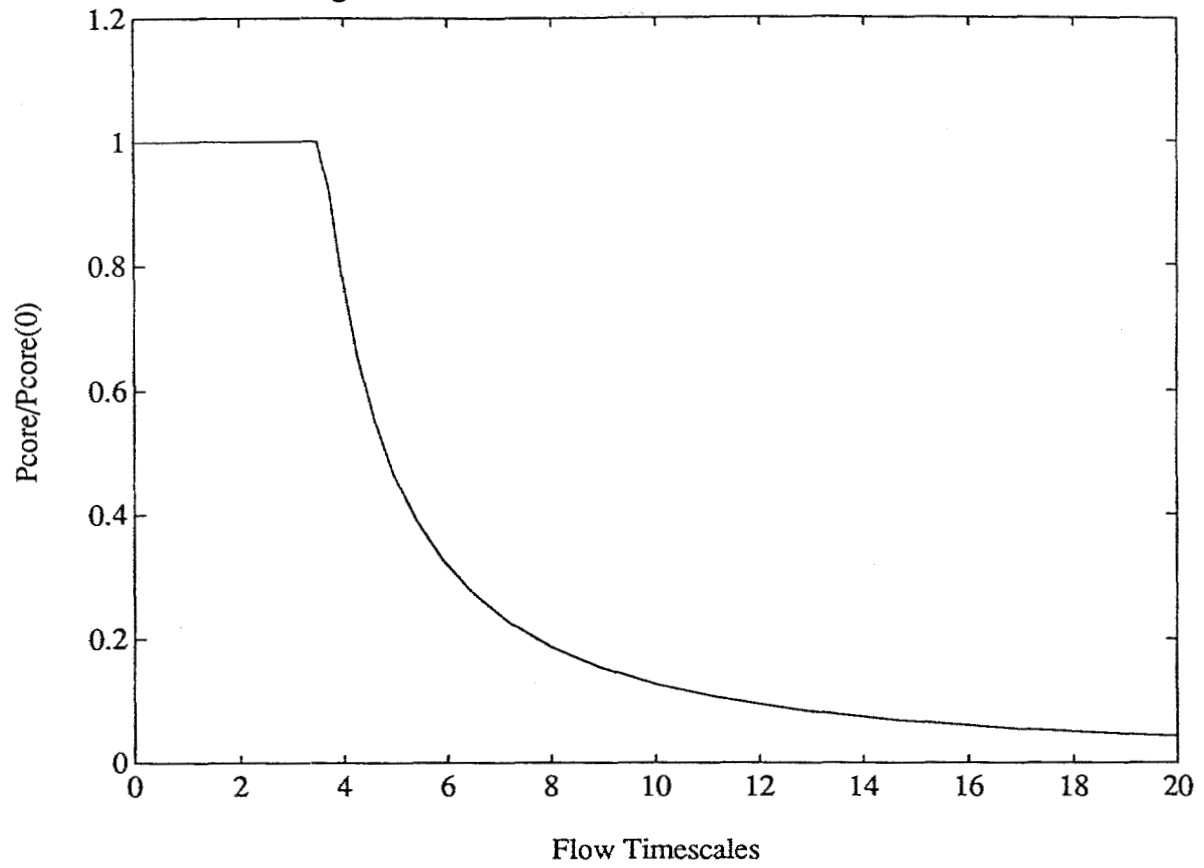
Figure 2.5 Normalized Impulse vs. Time for 1-D Thruster
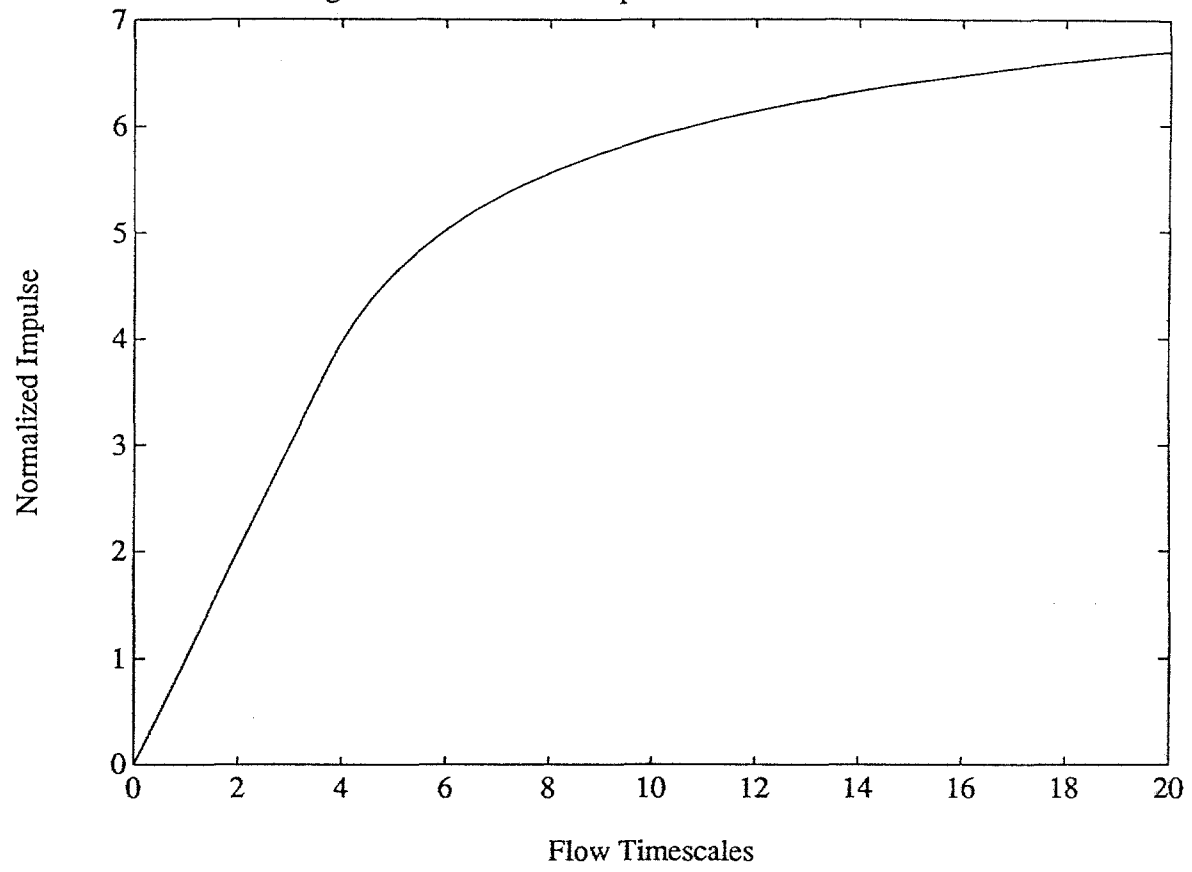
Figure 2.6 Worst Case 3-D Thruster Efficiency vs. Aspect Ratio
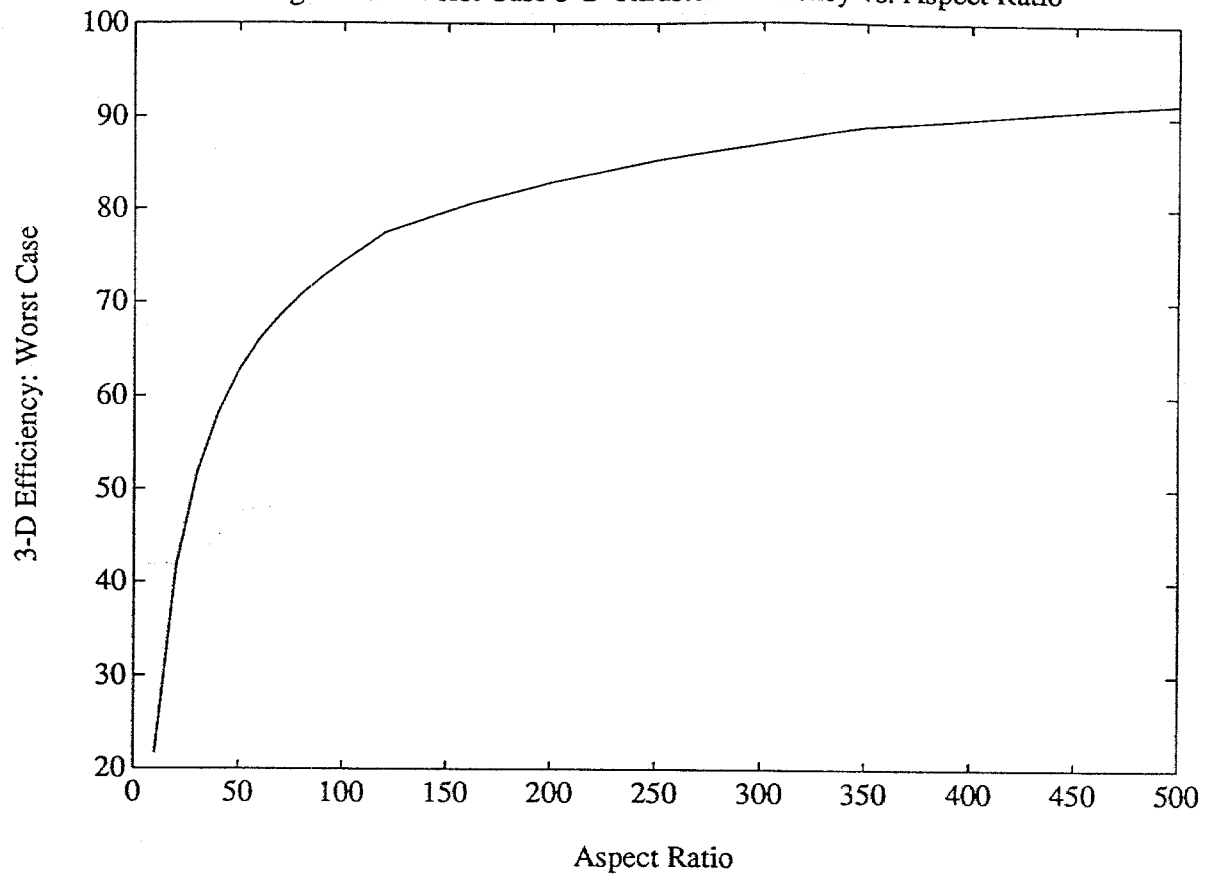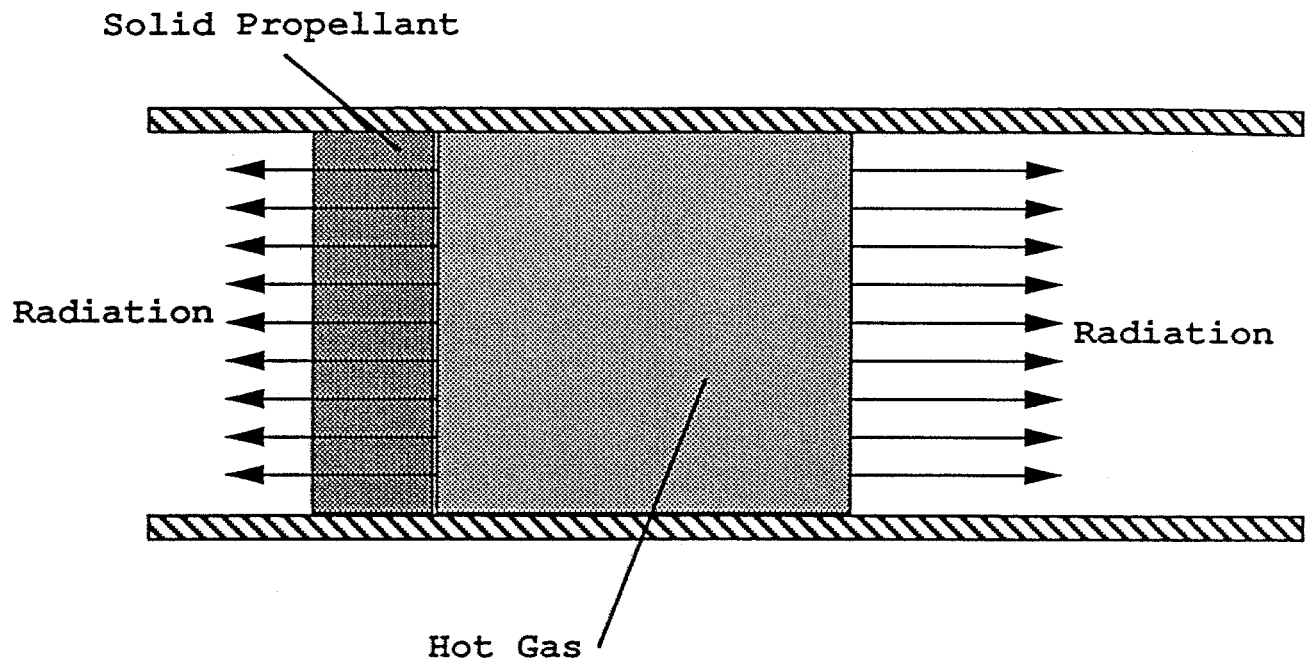
$$q = \varepsilon \ \sigma \ T^4$$

$$\varepsilon = .18$$

Figure 3.1 Radiation Calculation Schematic

Energy is allowed to escape the hot gas as radiation. The total forward and rearward losses are estimated to be less than 2.5% of the heat supplied to the gas by the laser. The emmisivity of 0.18 is the same as used by Jumper et. al in studies of LSD waves in aluminum vapor. The calculation is 1-D. For an axisymmetric system there will be losses to the sides as well, in an amount that depends on the Aspect Ratio of the LSD wave.

Figure 3.2a: Base Gas Temperature vs. Time for RAD.BAS
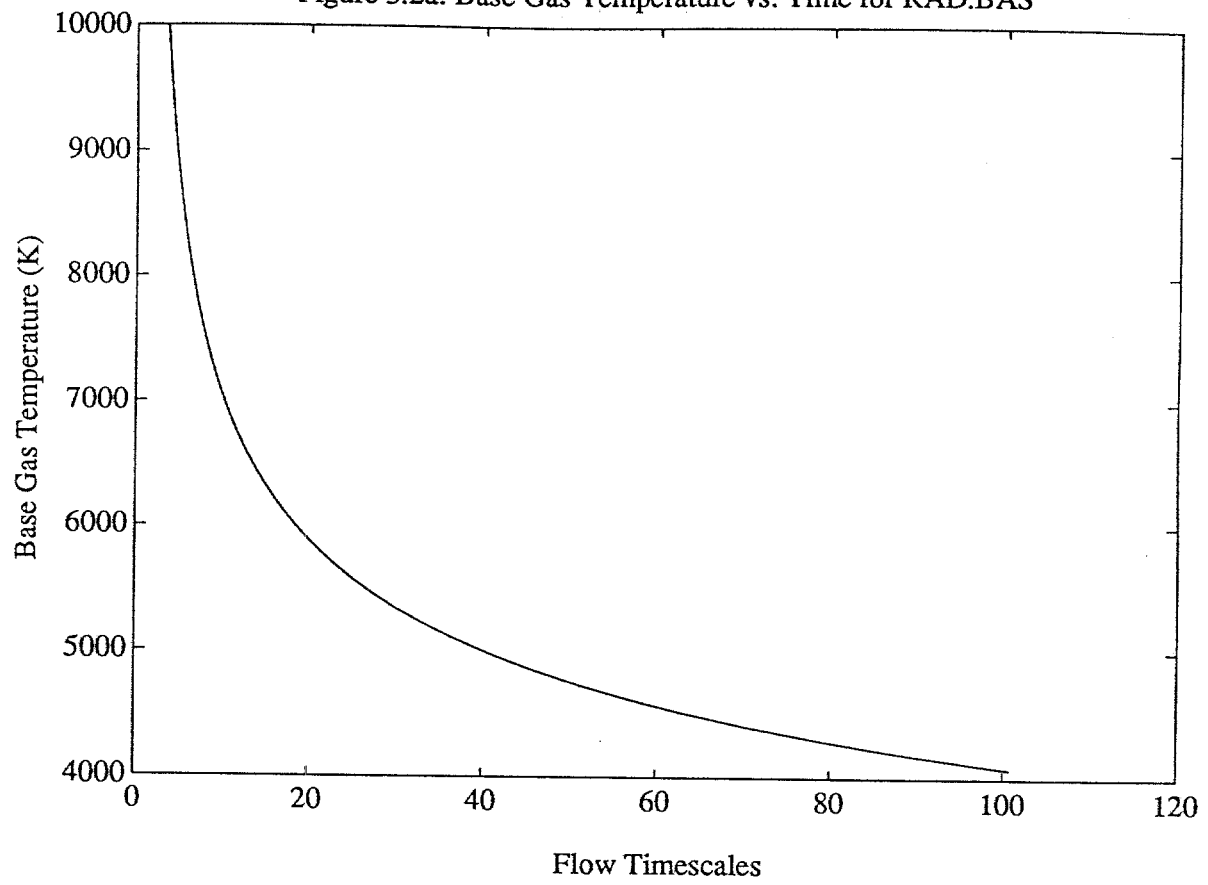
Figure 3.2b: Base Gas Radiative Flux vs. Time for RAD.BAS
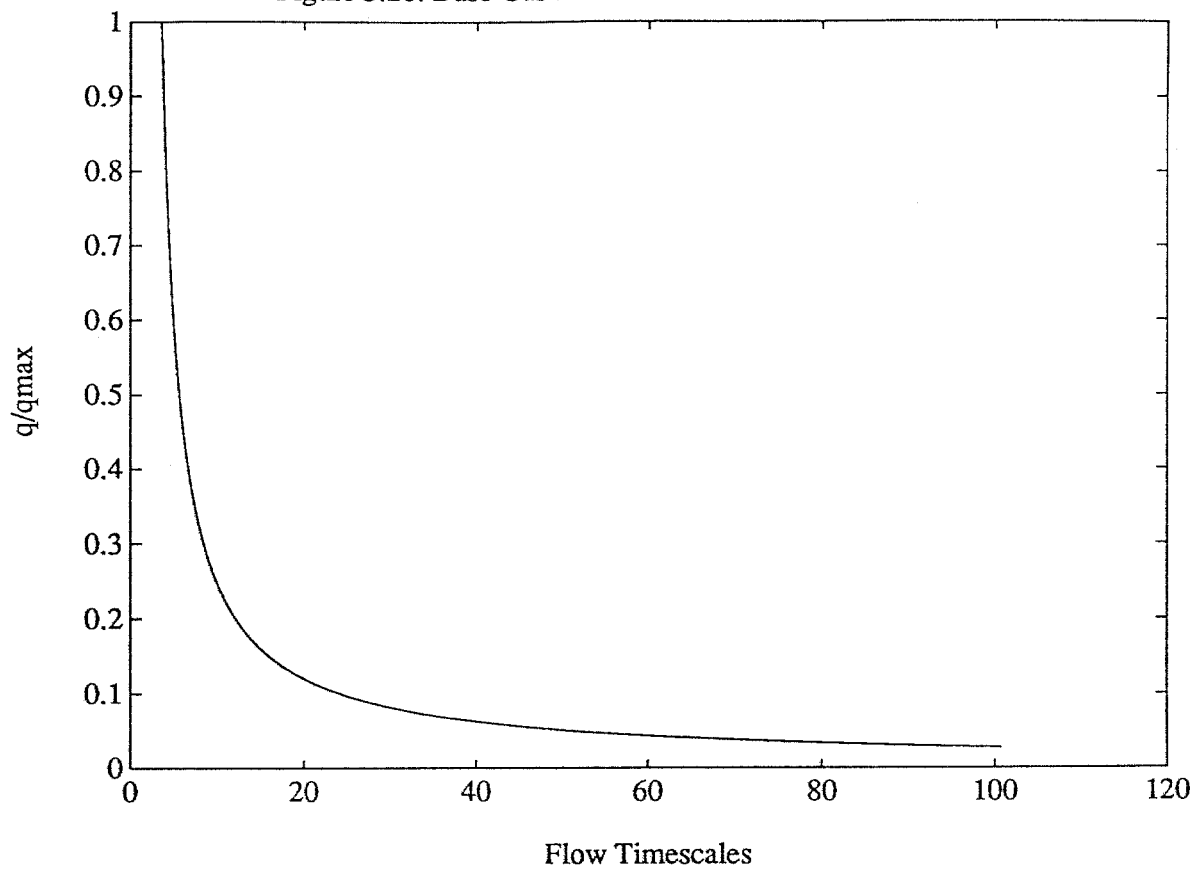
Figure 3.3: Integrated Heat Loss by Radiation vs. Time
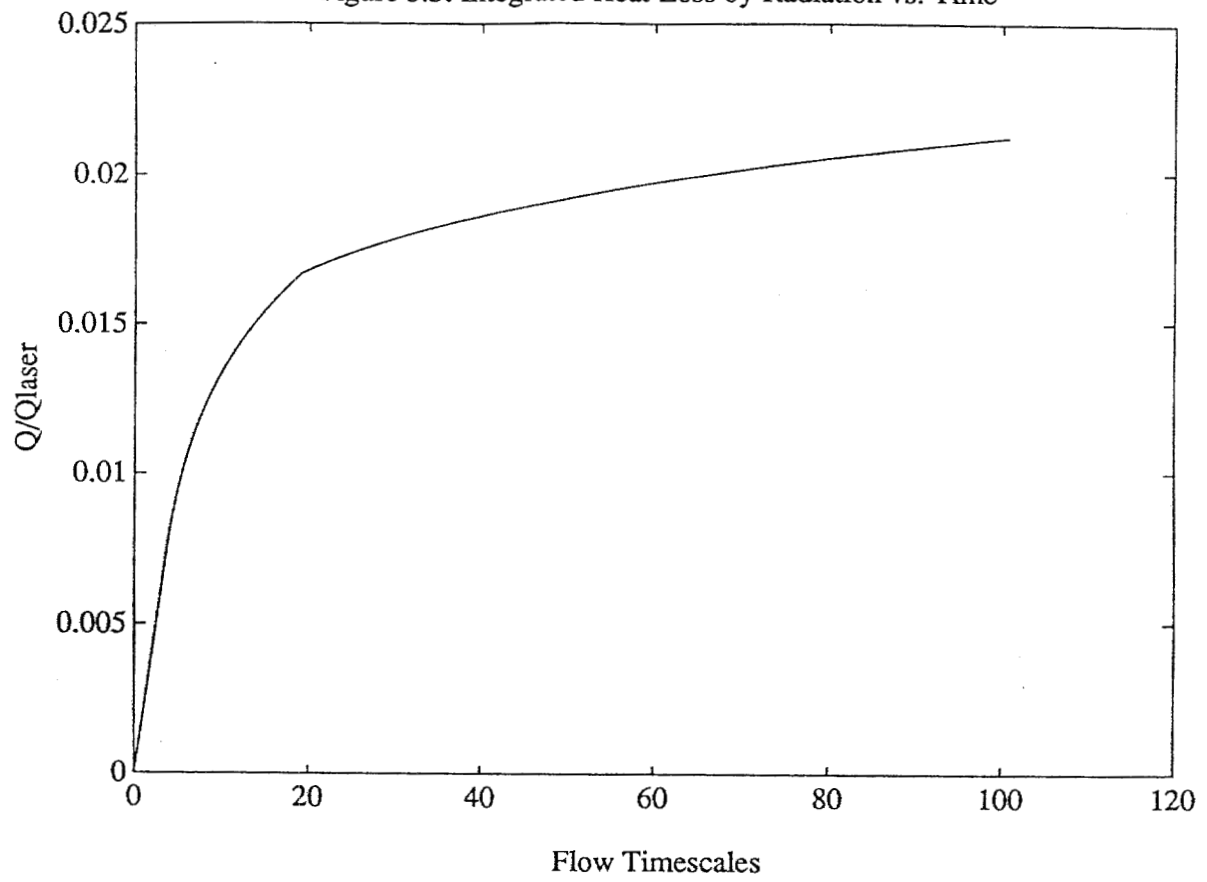
Vacuum Technique

Consider the Simple Wave Equation

$U_t + U_x = 0$ Solution $U(x,t) = f(x-t)$

The B.C.'s $U(0,t) = 1$ $U(x,0) = 0$ for $x>0$

Solution: A Right Propagating Square Wave.

At sufficient time into solution, each numerical method used to solve the problem will change the wave shape. The solutions shown are staggered to see them better.
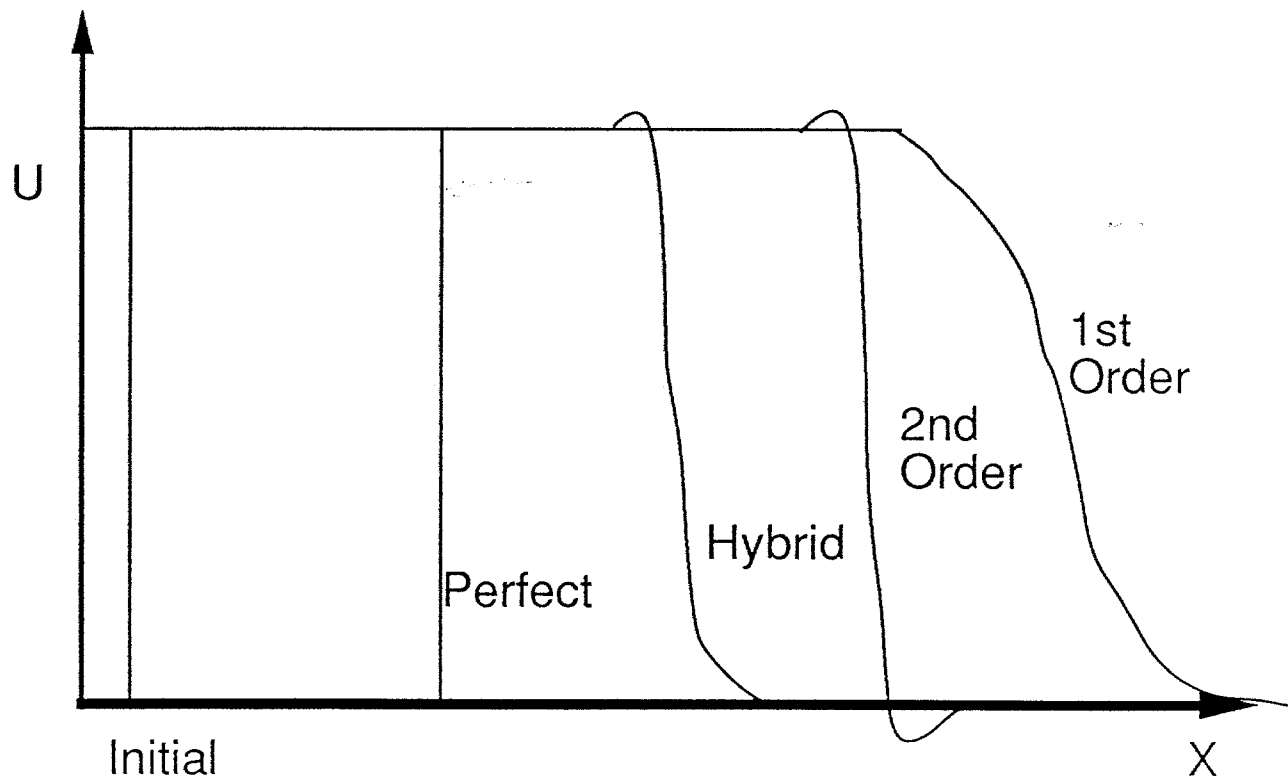
At the Vacuum Interface, 2nd Order Method Undershoots the density and pressure, yielding $\rho<0$. The 1st Order solution is used there: Hybrid Method.

Figure 3.4: Vacuum Technique

A

M = 2.5

B

F

X
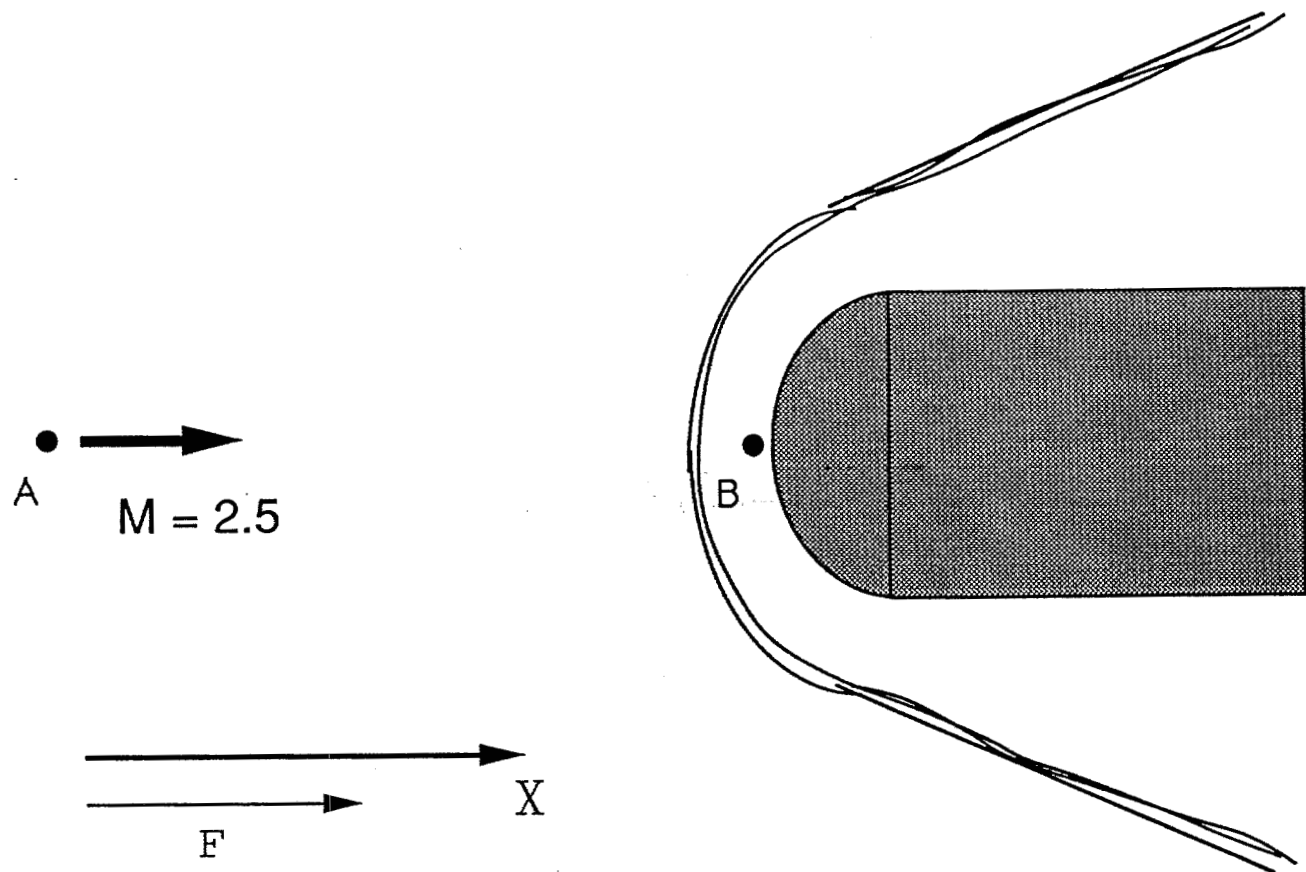
$$F = F^+ + F^-$$

at A: $F^- = 0$

at B: $F^+, F^- \neq 0$

Figure 3.5: Flux Splitting Concept.

A practical example from aerodynamics illustrates the
concept of flux splitting. In this case, the flow about
a bullet traveling at M=2.5 is shown. The fluxes of mass,
momentum, and energy will have fully positive
characteristic speeds at point A, because the flow is
supersonic there. At the stagnation point B, the
characteristic speeds will be of mixed sign, giving rise
to a flux with positive and negative terms.
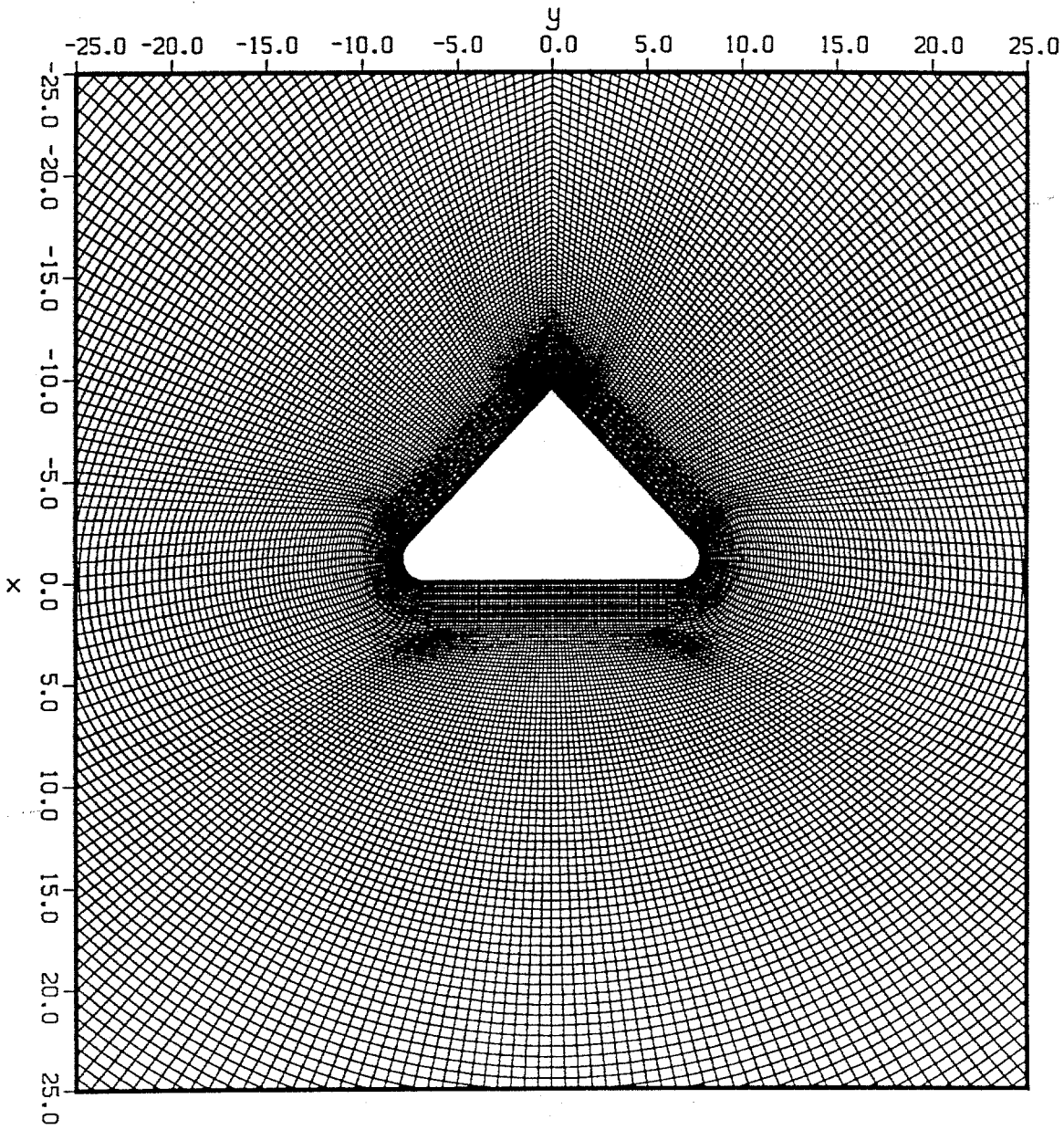
GRID
Figure 3.6 : C grid

128×255   GRID
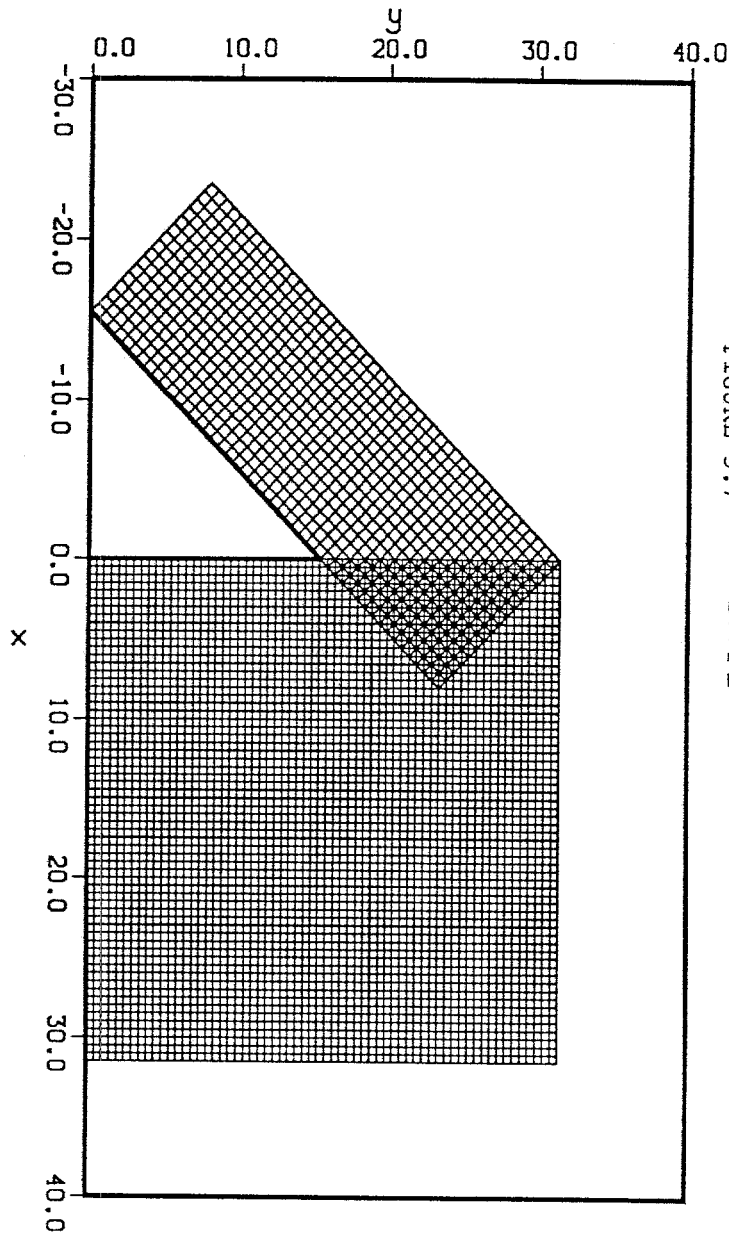
FIGURE 3.7   GRID

64×64   —   GRID 1
48×17   GRID 2

FIGURE 3.8   GRID

Square Wave: Square Grid

PRESSURE
Square Wave: Square Grid
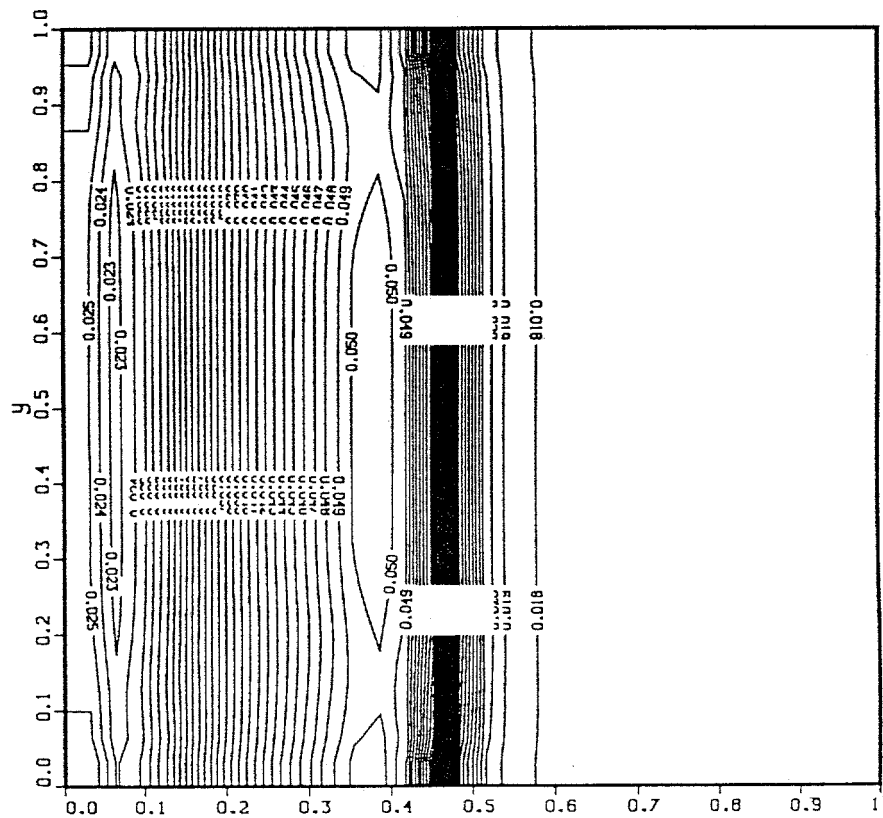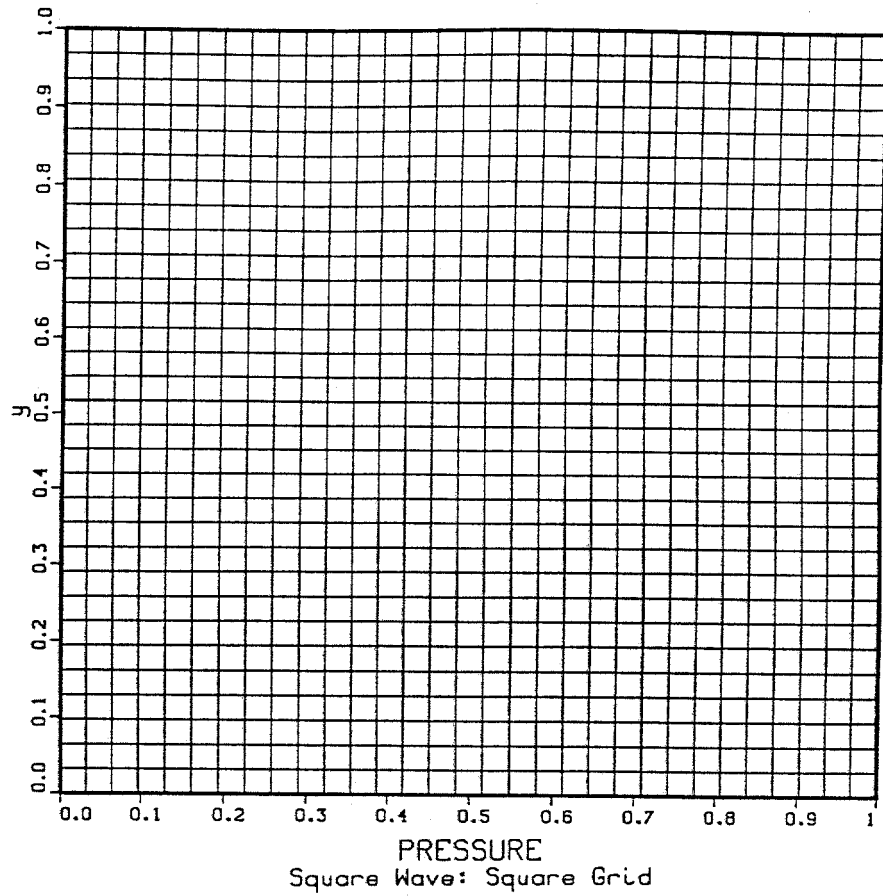
FIGURE 3.9   GRID

Plane Wave Test: Curved Grid
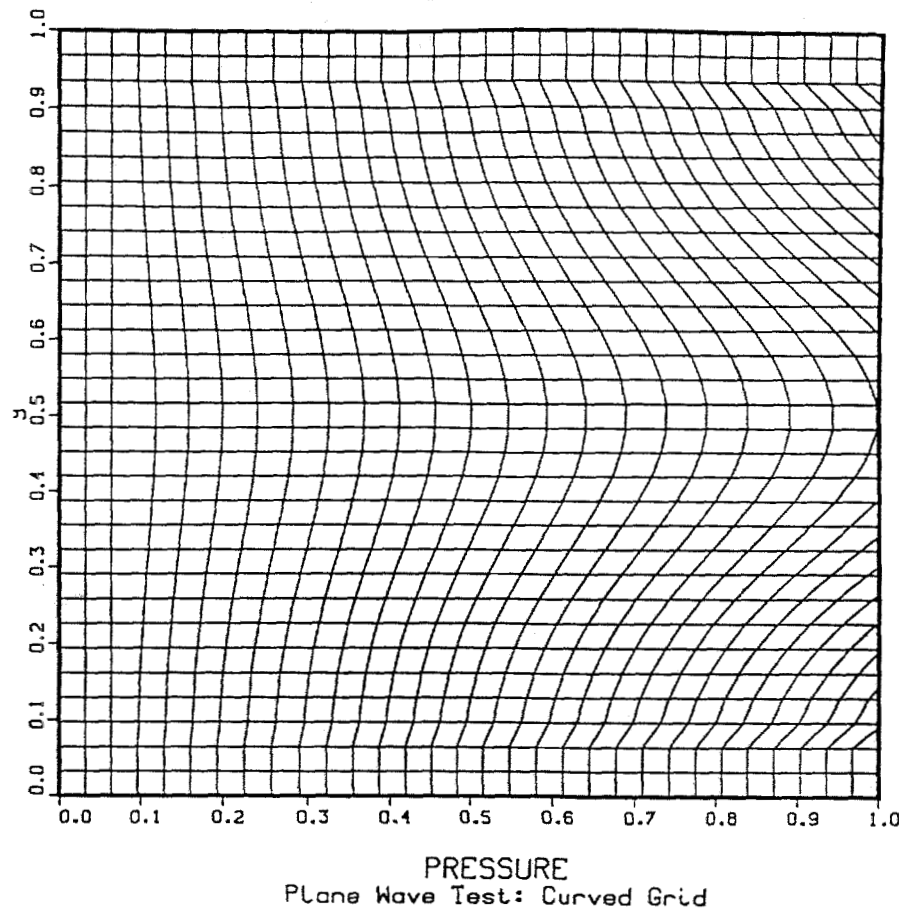
PRESSURE
Plane Wave Test: Curved Grid
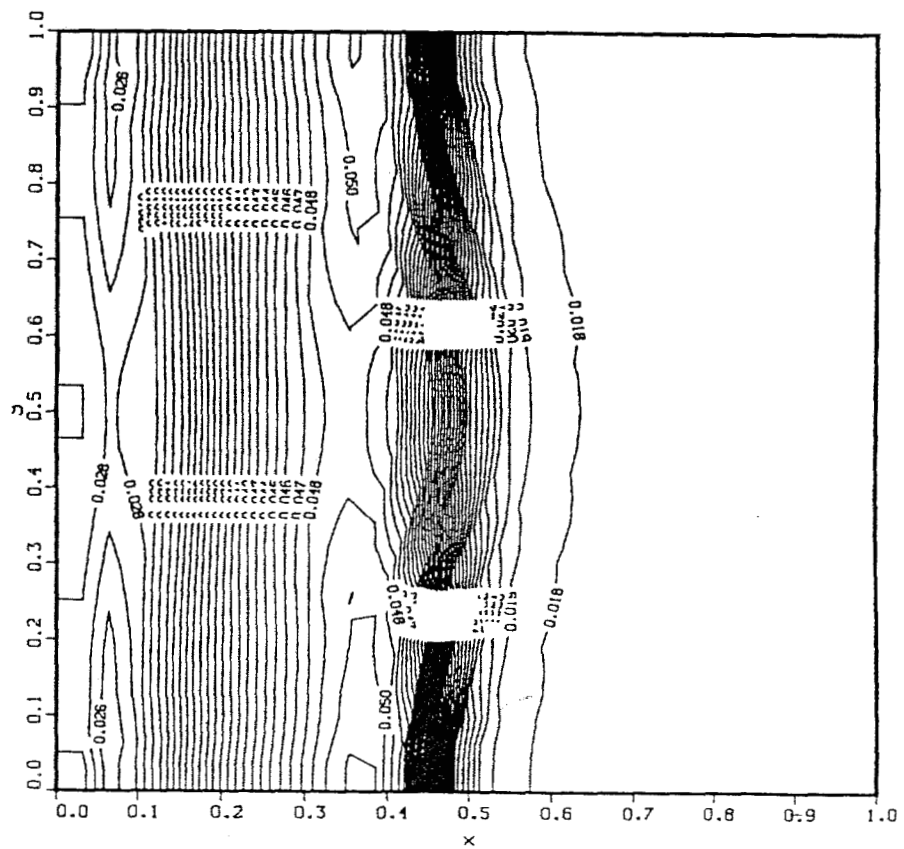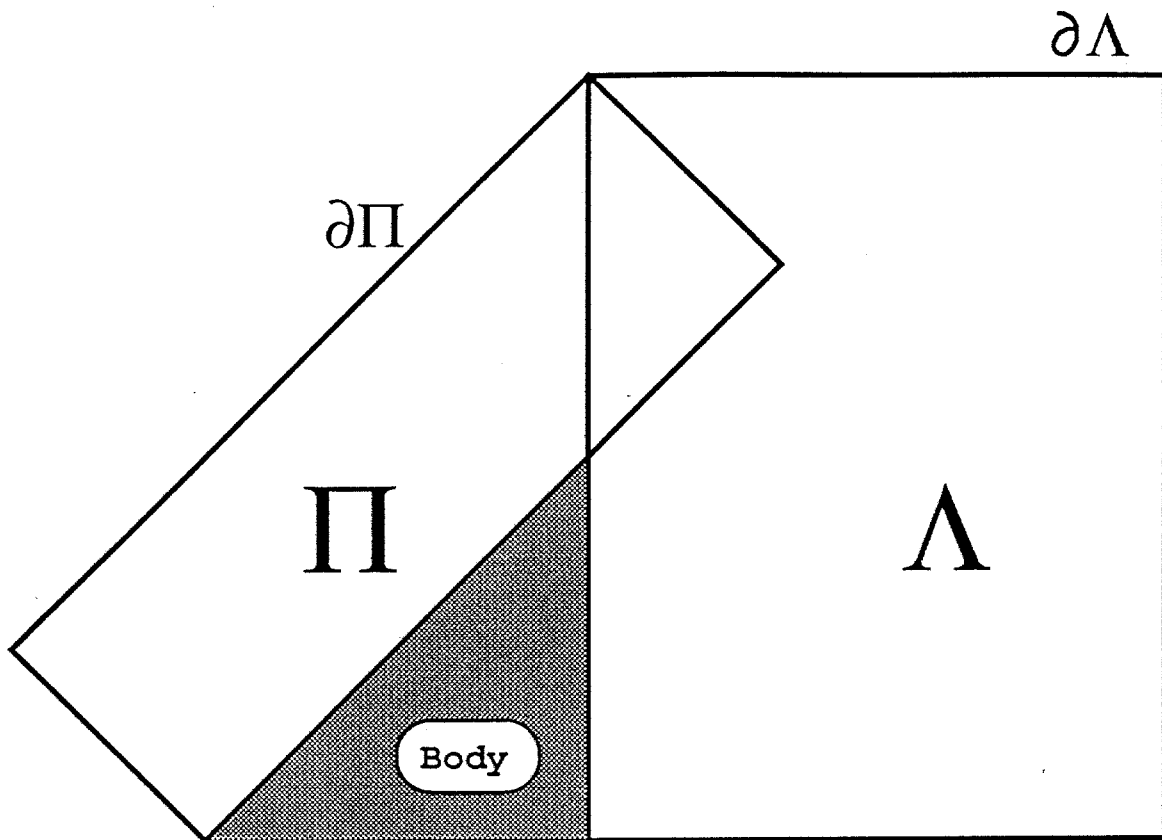
Figure 3.10: Π **and** Λ **Regions for Coverage of Domain**

In order to cover the 2-D space around a half cone with equispaced meshes, two grids are used. The solution is advanced globally by the same time step, and compatibility between the two regions is enforced. The surfaces $\partial\Lambda$ and $\partial\Pi$ are the boundaries of their respective domains.
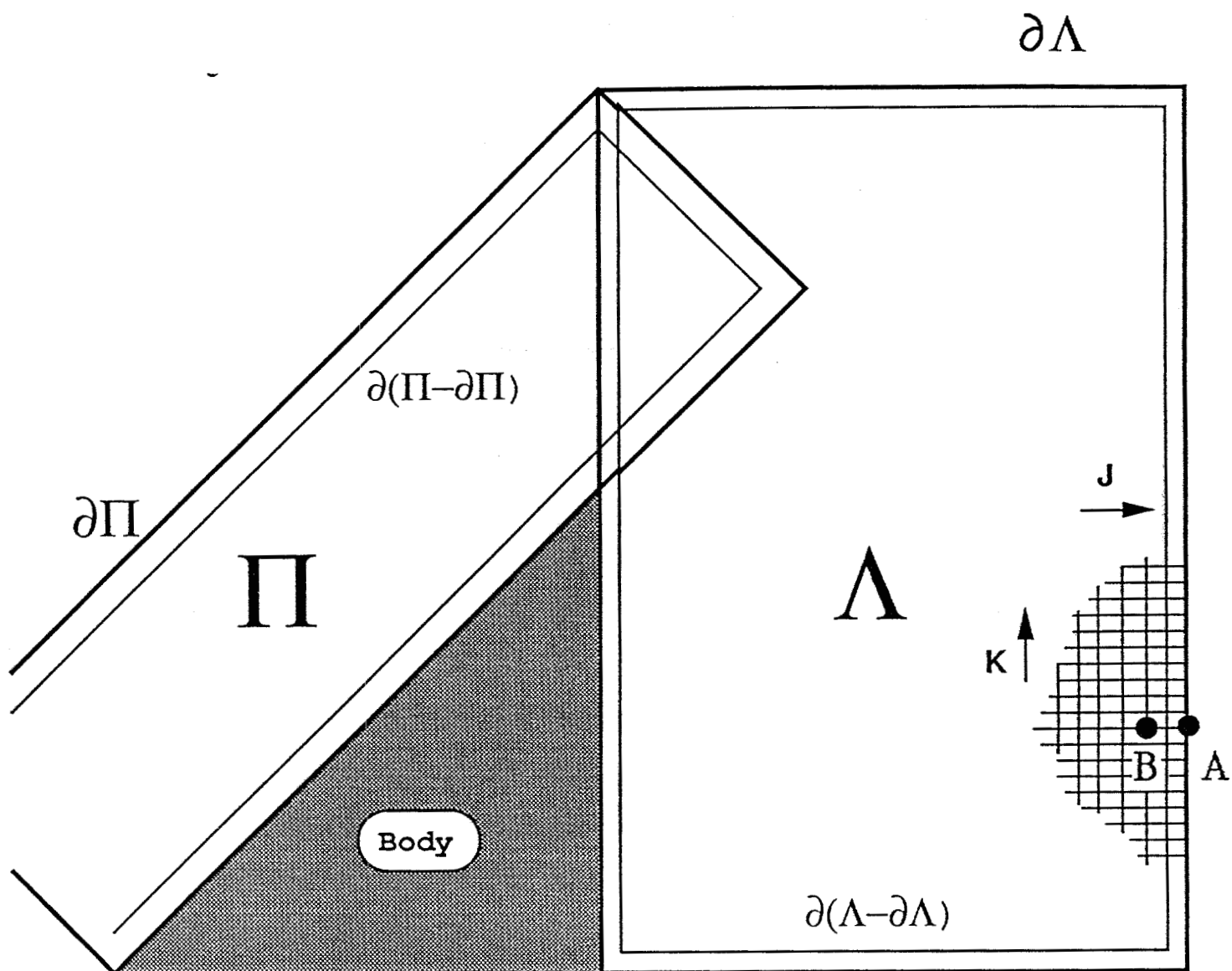
Figure 3.11 Boundaries and Discussion

Since Π and Λ cover the 2-D region of the flowfield, it is necessary to properly impose boundary conditions on the outer surfaces $\partial\Pi$ and $\partial\Lambda$. However, the second order accurate method requires data from two adjacent field points in all directions, so the solution is second order accurate only interior to the surfaces $\partial(\Lambda-\partial\Lambda)$ and $\partial(\Pi-\partial\Pi)$. On a grid, this means that if the point A shown has coordinates (Jmax, k) then the solution at B, which has coordinates (Jmax-2, k) will be second order accurate.
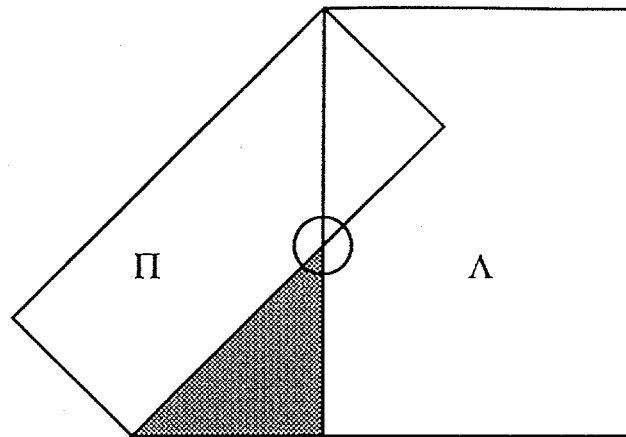
Blow Up of Corner:
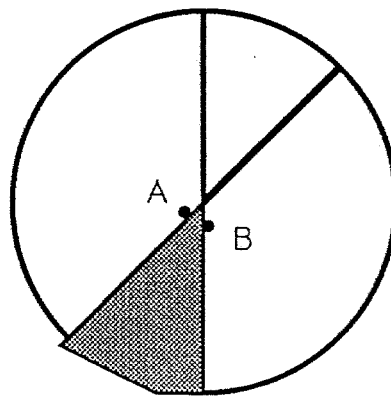
Figure 3.12. Corner Assumption

The flow at the corner, where the two grids meet is singular. The location in the grid of points A and B is identical, but for boundary conditions, each point is assumed to be displaced an infinitessimal amount along the surface away from the corner. Thus A takes its information from

Π and B takes its information from Λ. Tests of the assumption, including a shock-wave Prandtl-Meyer expansion run around the corner have proven successful.

DENSITY
45 DEGREE CONE.   M-2.89   Cp/Cv-1.4
STEADY BENCHMARK FOR 2 GRID SCHEME
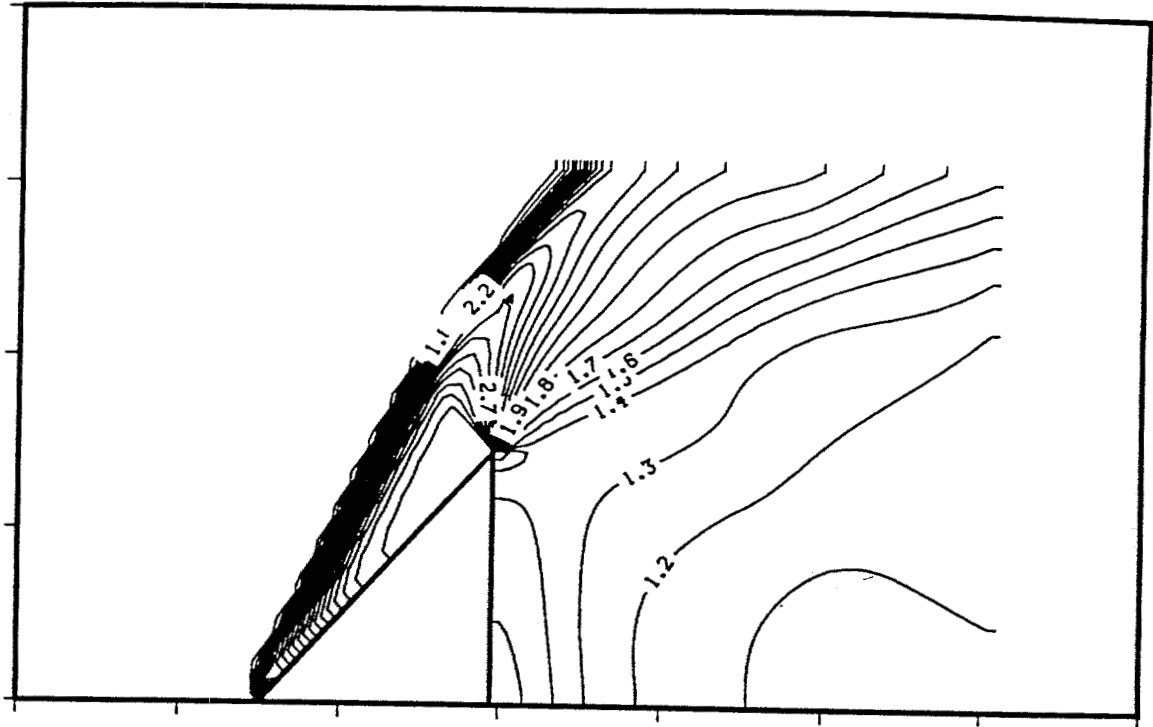
GRID
MAIN GRID: 64 × 64
SECOND GRID: 47 × 18
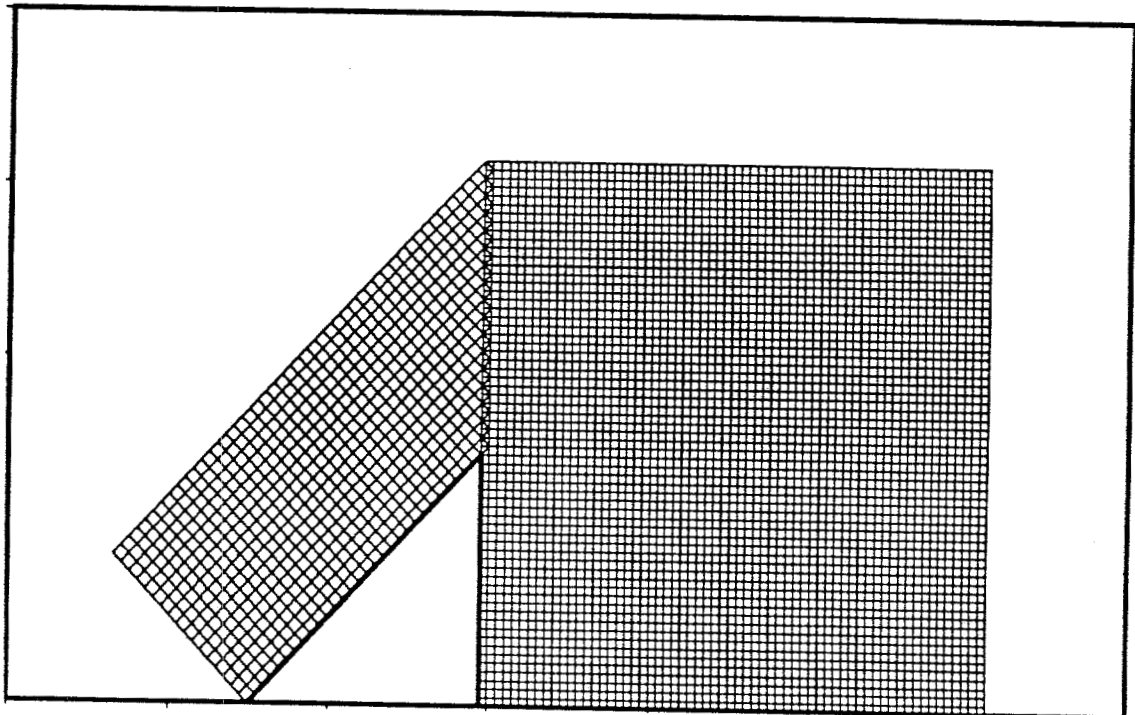
FIGURE 3.12 a: Shock-Expansion Test of Double Grid Plan.
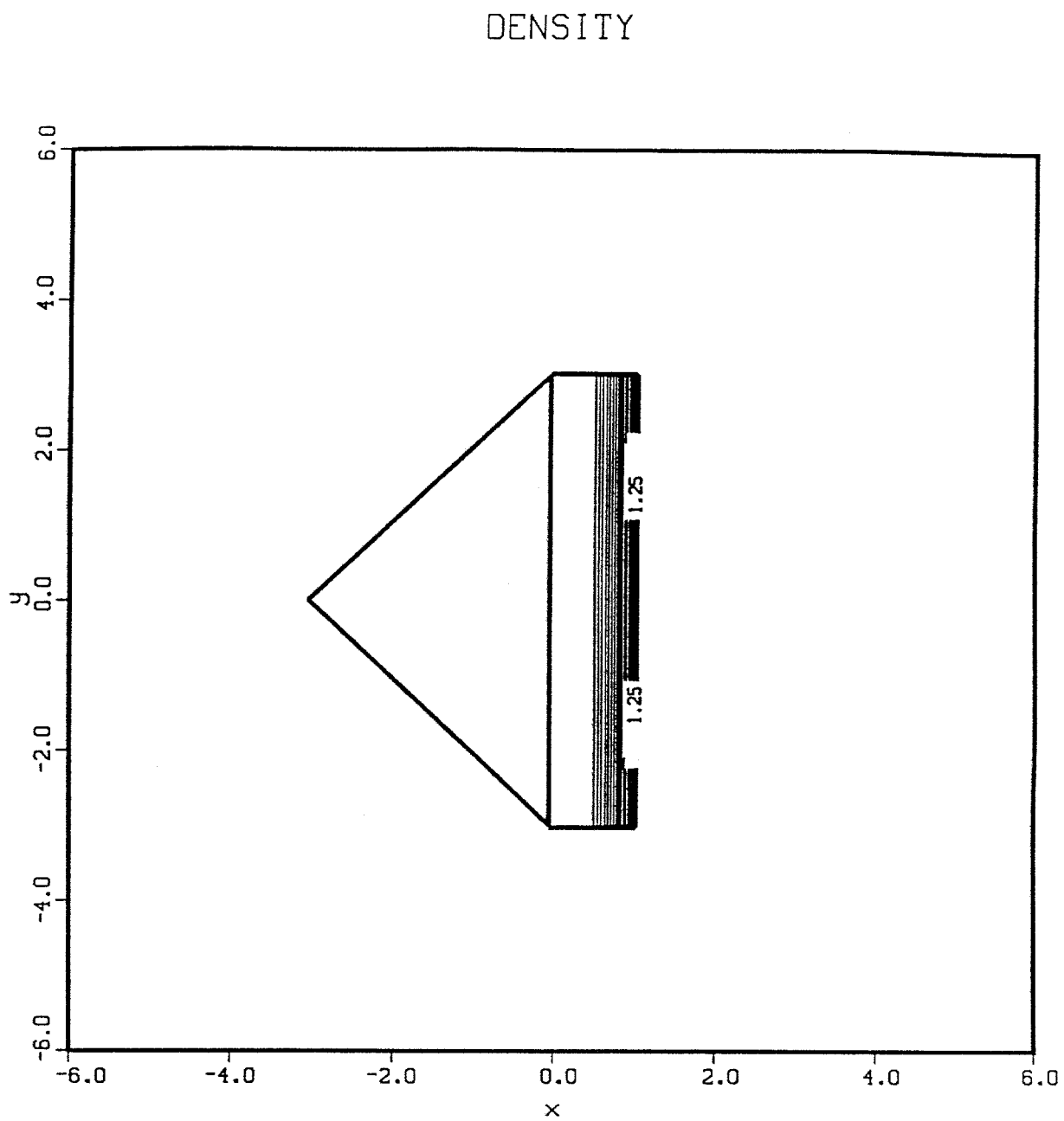
DENSITY

Figure 3.13: Initial Conditions for Blast Runs

Pictured is the initial condition supplied to the code *PROP.FOR*. The Aspect Ratio is $A = 6$.
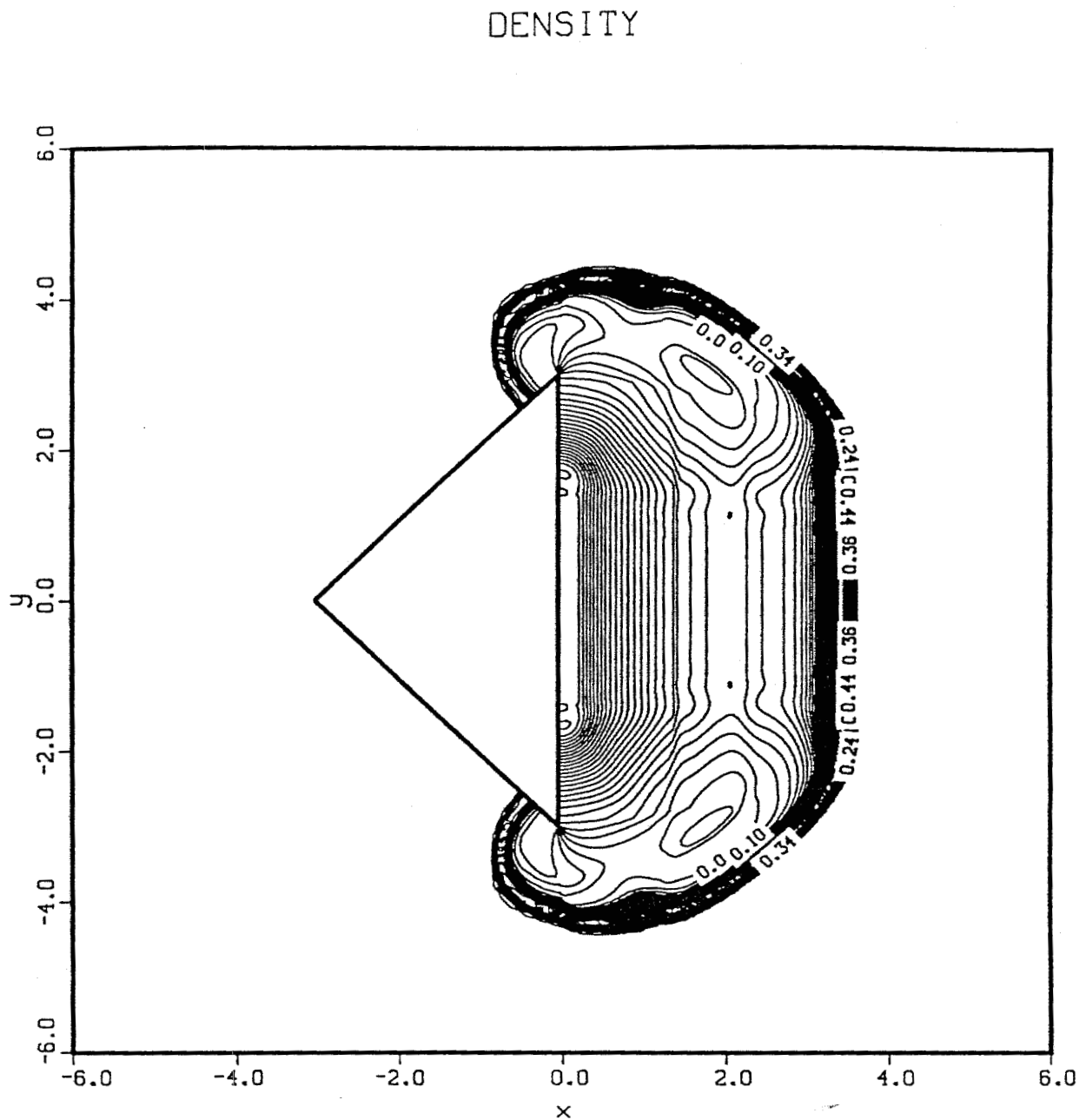
Figure 3.14a: Blast Wave Propagating into Thick Ambient Gas

In this case, the ambient density is increased by a factor of 10 over the usual amount. A strong shock wave is formed, which has a containing effect on the expansion. Some distortion of the density contours is observed interior to the shock; this is where the flow mach number becomes supersonic and is an artifact of the characteristic based upwind numerical scheme used. The solution has been advanced 2τ and the Aspect Ratio is 6. The ratio of density at the base to the ambient is 10.

DENSITY
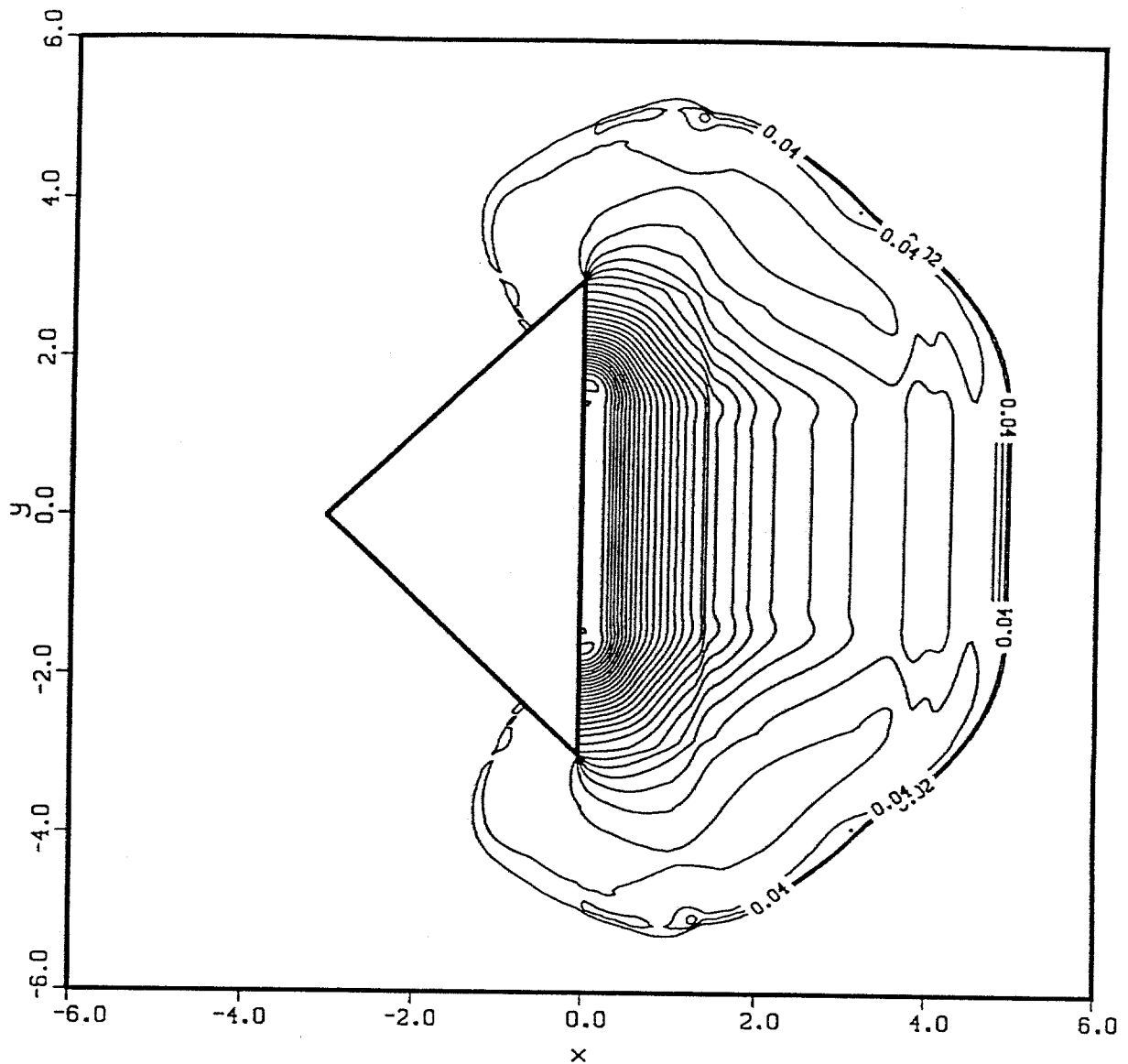
Figure 3.14b: Blast Wave Propagating into Thin Ambient Gas

At the lower ambient density used here, the gas freely expands into a larger volume. Comparison with Figure 3.14a shows a marked difference in the solution, although all other parameters except the ambient density are the same. At the transition to supersonic flow, there is still some distortion of the contours, but it is relatively minor. The time into the blast is again 2τ and the Aspect Ratio is 6. The ratio of density at the base to the ambient is 100.

Normalized Impulse vs. Time as Aspect Ratio, A, is Varied.

Total Impulse Recieved / Impulse from Detonation Alone

A = ∞
A = 24
A = 16
A = 12
A = 8
A = 4
A = 2

Time (μ sec)
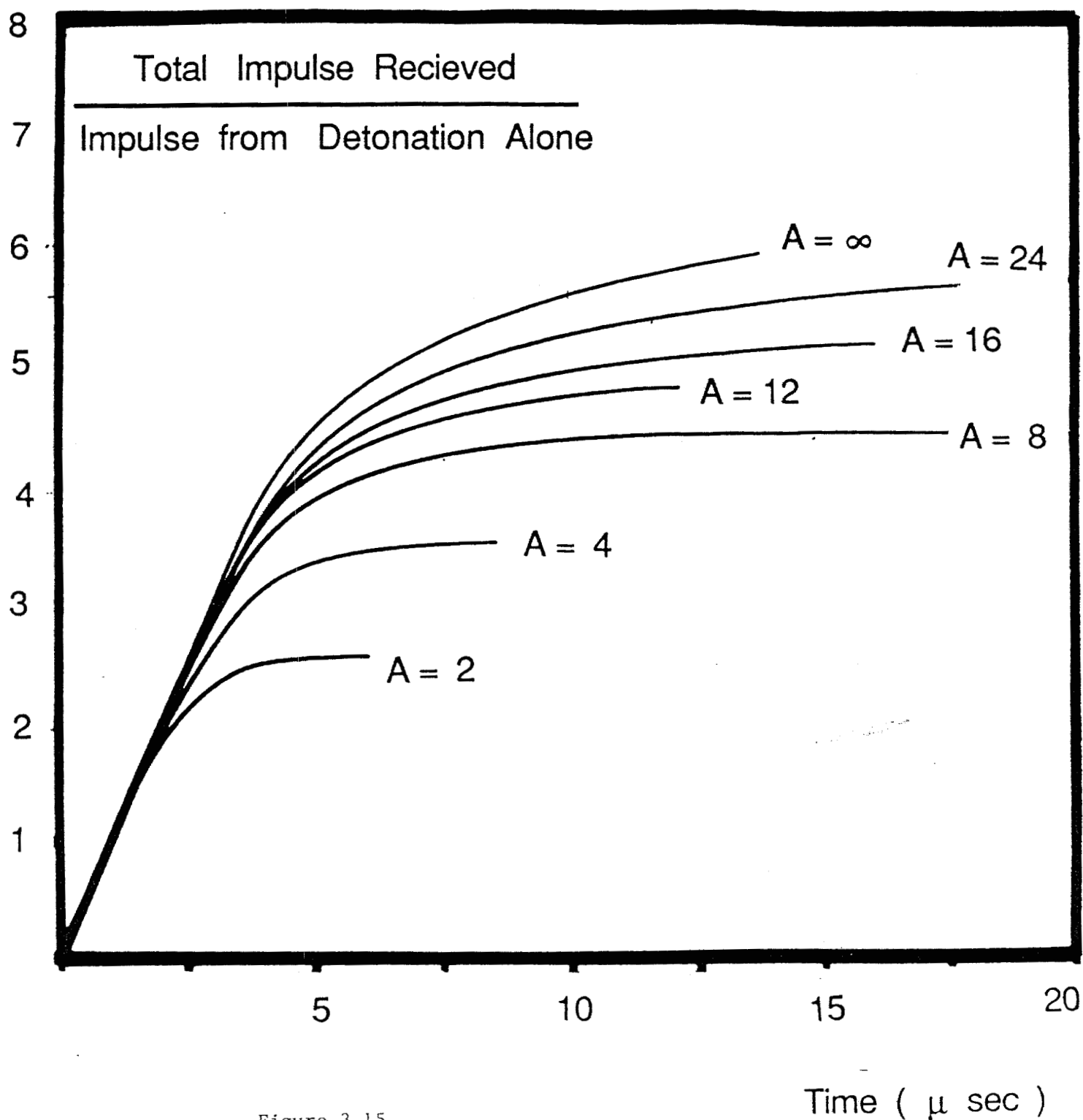
Figure 3.15

FIGURE 3.16

Core Base Pressure vs. Time for PROP.FOR

Pcore / Pcore(0)

1.0

0.9

0.8

0.7

0.6

0.5

0.4

0.3

0.2

0.1

A = 2

A = 4

A = 16, 24, ∞

A = 8

A = 12

2.5   5   7.5   10   12.5   15   17.5   20

Flow Timescales
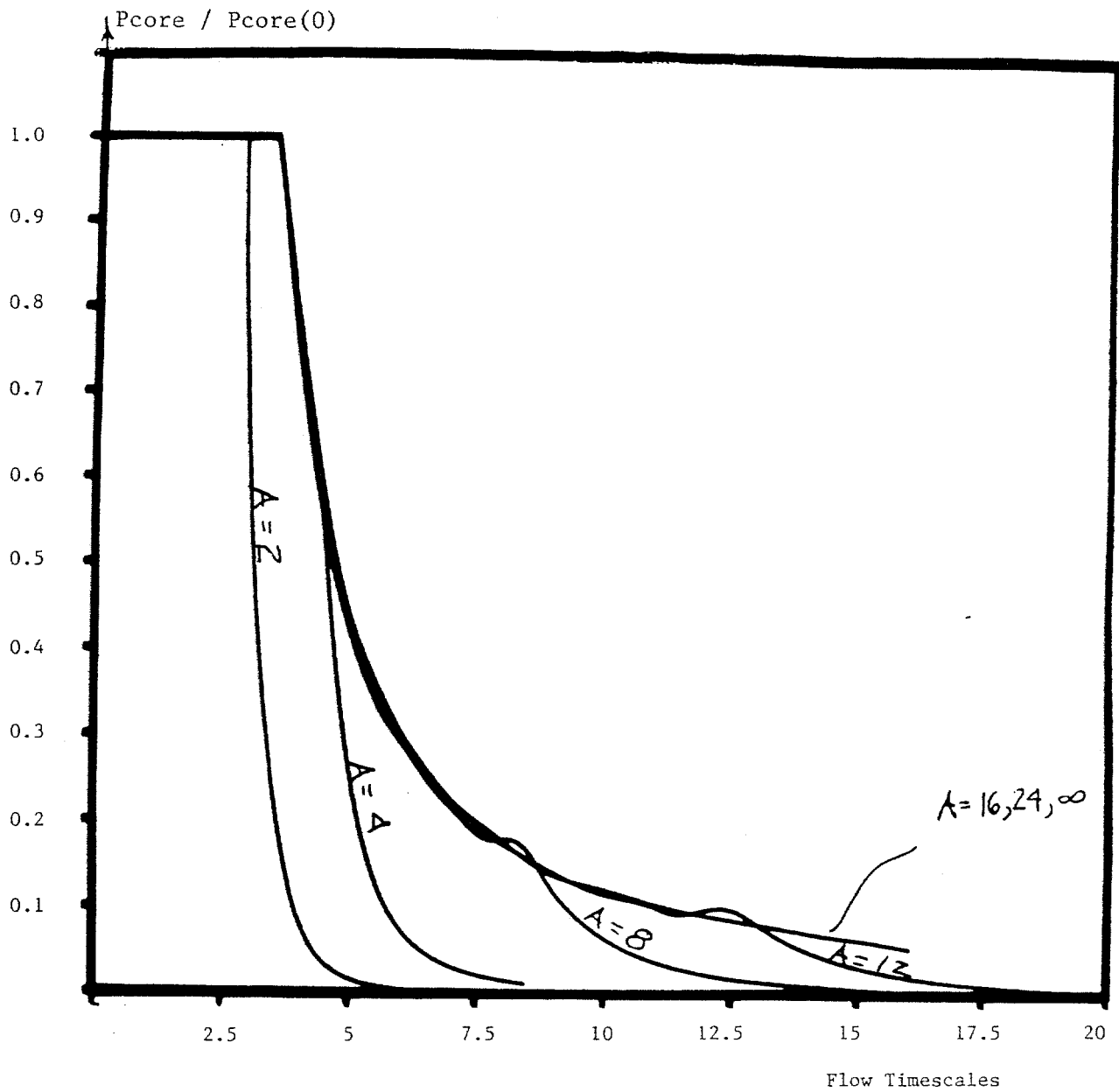
Propulsive Efficiency vs. Aspect Ratio
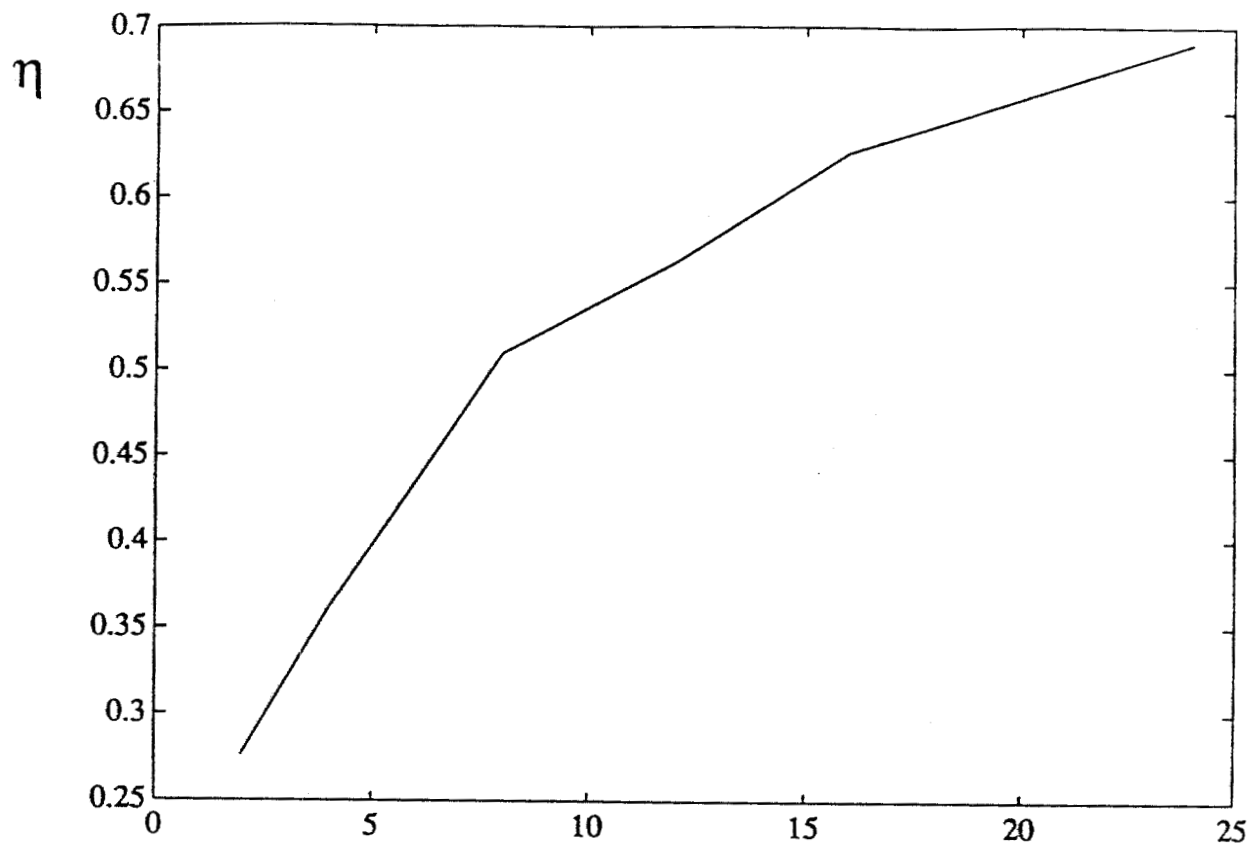
$$\eta = \text{Efficiency} = (\,3d\ \text{Impulse}\,) / (\,1\,d\ \text{Impulse}\,)$$

$$A = \text{Aspect Ratio} = \frac{\text{Base Diameter}}{\text{LSD Travel Distance}}$$

Figure 3.17

Effect of Larger Target Size than Laser Spot Size

Target

LSD Wave   d1   d2

d3
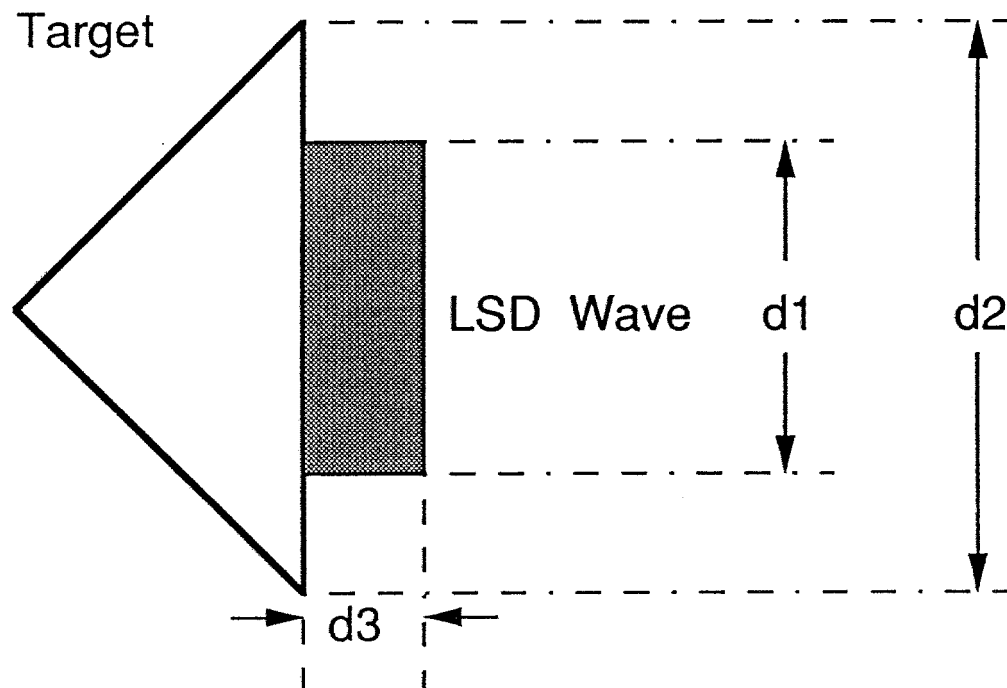
Significant Parameters:

A : Blast Wave Aspect Ratio = d1 / d3

Z : (Target Diameter) / (Laser Spot Diameter) = d2 / d1

Finding:

For A = 6.15, as Z is increased the total thrust produced

by the system increases by up to 35%

Figure 3.18

Impulse Development as Target Size is Increased for Fixed LSD Size

y-axis: (Blast+Detonation Impulse)/(Detonation Impulse)

Time Units: 1 unit = 50 ns
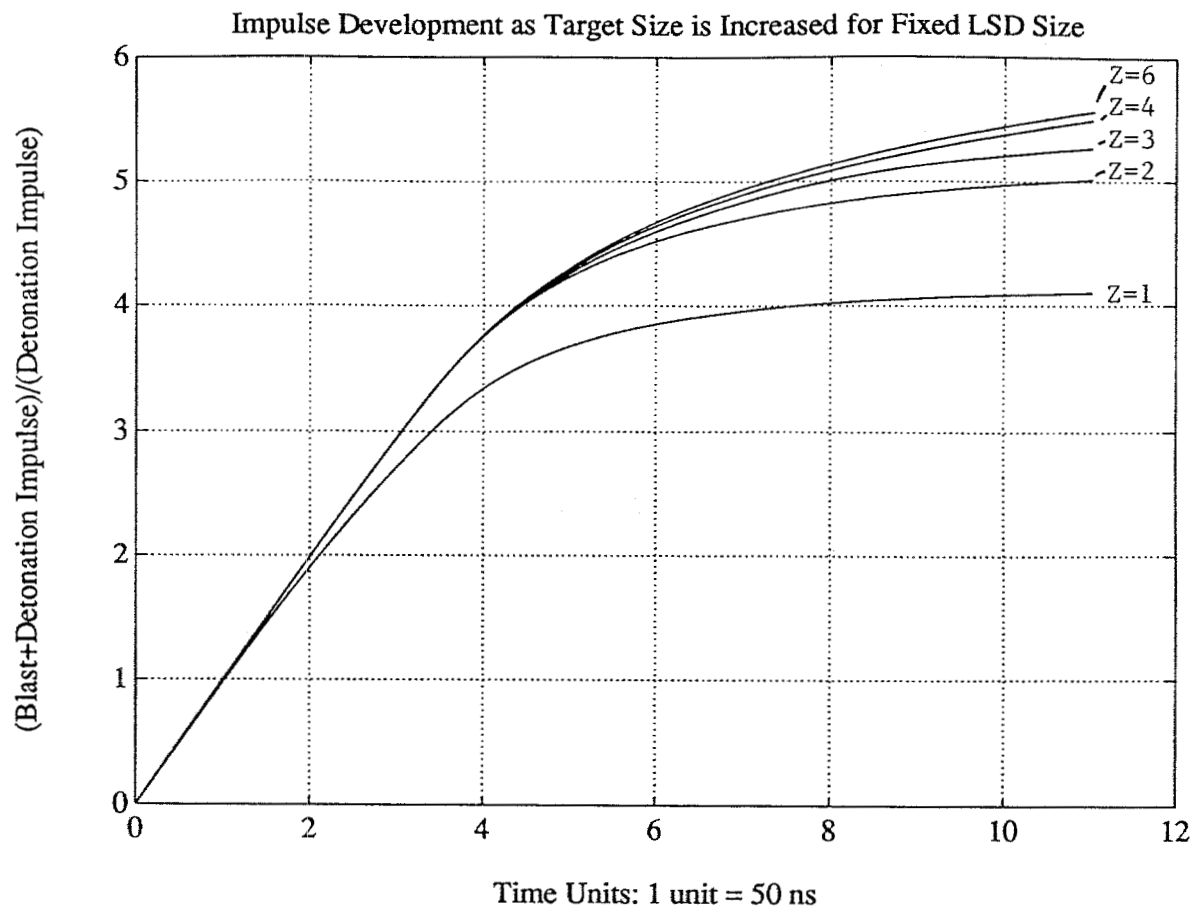
Code: SPOT.FOR

Date: 10/9/89

Aspect Ratio: 6.15 = (LSD Wave Diameter)/(LSD Wave Thickness)

Z : (Target Diameter)/(Laser Spot Diameter) : 1,2,3,4,6

Figure 3.19

Impulse Advantage as Target Size is Increased for Fixed LSD Size

Y-axis: Impulse Advantage : (Impulse Received)/(Impulse for Z=1)

X-axis: Z : (Target Diameter)/(Laser Spot Diameter)
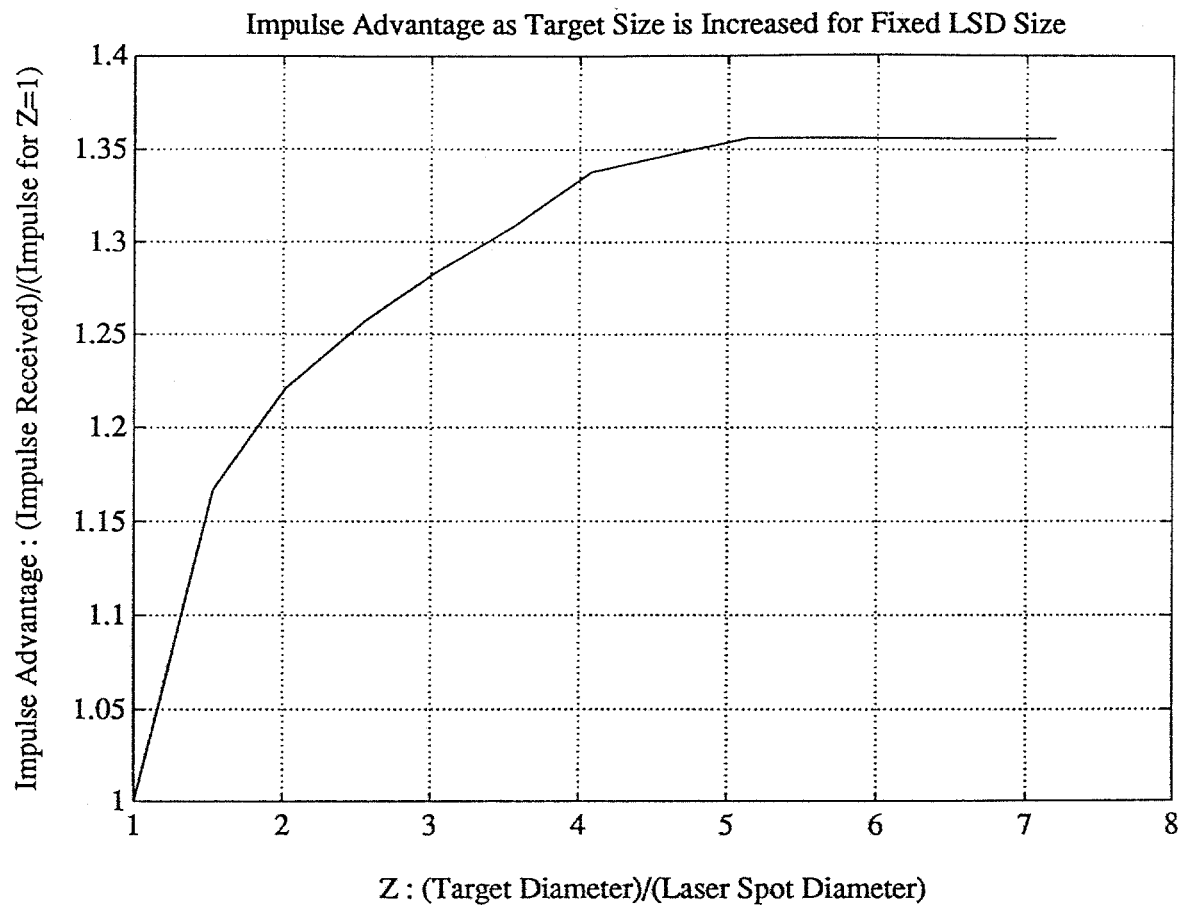
Impulse Received = Impulse received 10 characteristic timescales
                   into the blast phase of the flow, for a total
                   of 11 timescales including detonation phase.

Aspect Ratio: 6.15 = (LSD Wave Diameter)/(LSD Wave Thickness)

Code: SPOT.FOR
Date: 10/9/89

Figure 3.20

Skirt Configuration
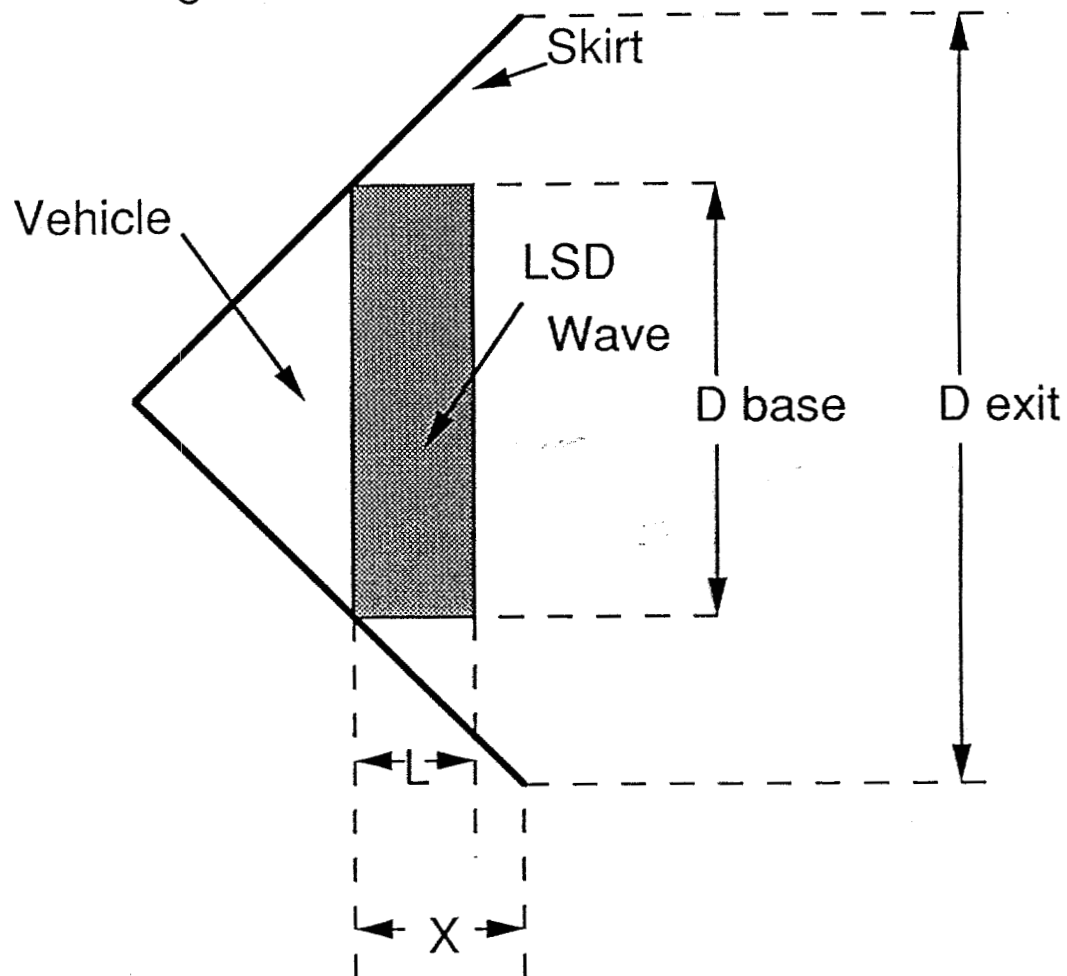
Geometric Parameters:

L = LSD Wave Thickness
X = Skirt Length
D base = Vehicle Base Diameter
D exit = Nozzle Exit Diameter

A = Aspect Ratio = D base / L
S = Skirt Ratio = X / L
AR = Area Ratio = (D exit / D base)^2

Vehicle Perfromance Parameter:

f = (Blast + Detonation Impulse) / (Detonation Impulse)

Figure 3.21

Figure 3.22

$$Z = \frac{Skirt\ Length}{LSD\ Length}$$

Aspect Ratio

Nozzle Exit Area / Entrance Area

Z = 0

Z = 1

Z = 2

Z = 3

Z = 4

Area Ratio of The Skirt Nozzle vs. Aspect Ratio and Skirt Length
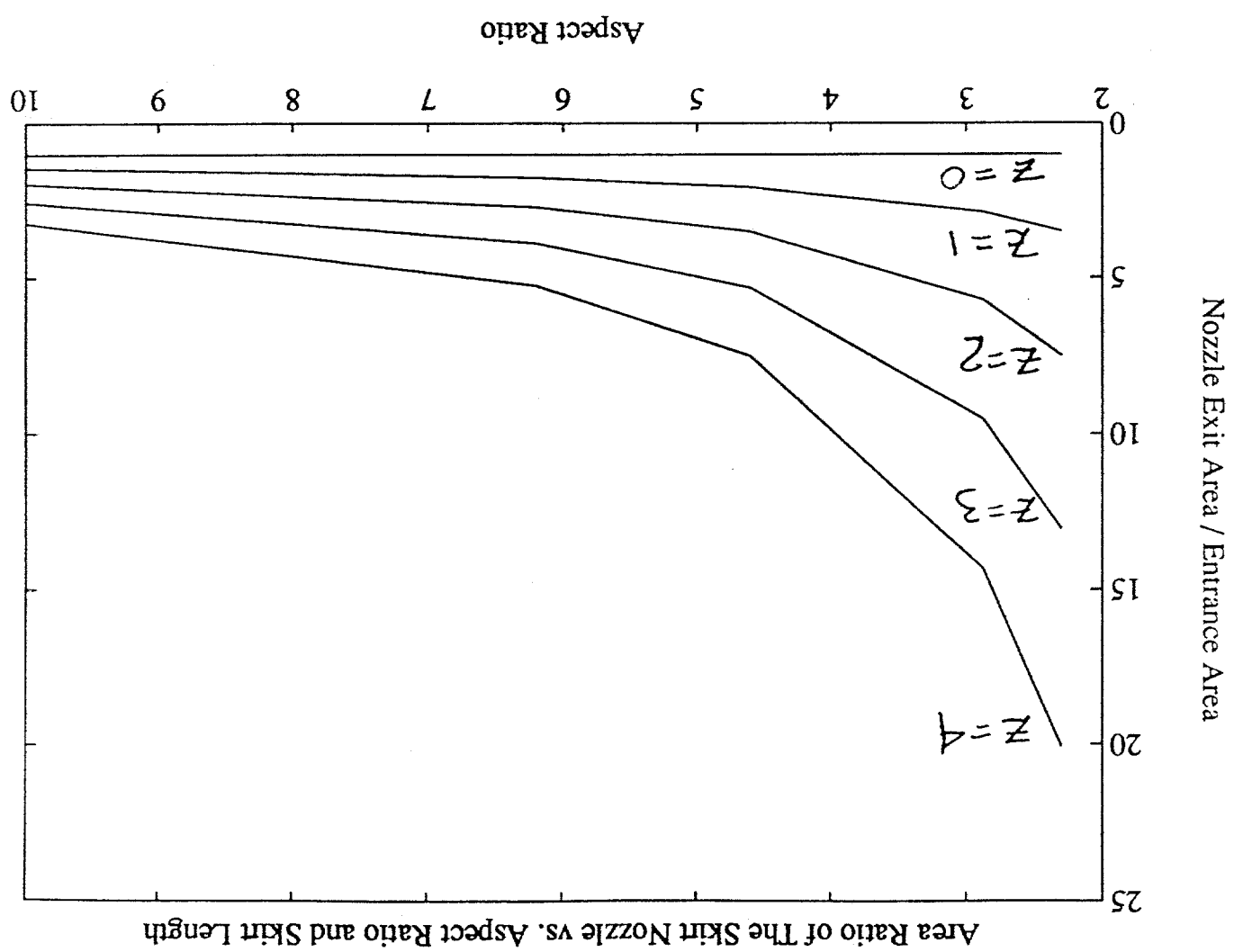
Figure 3.23 Impulse vs. Time For Skirt of Z=2 and No Skirt for A=9.4

Impulse Performance vs. Aspect Ratio for Different Skirts
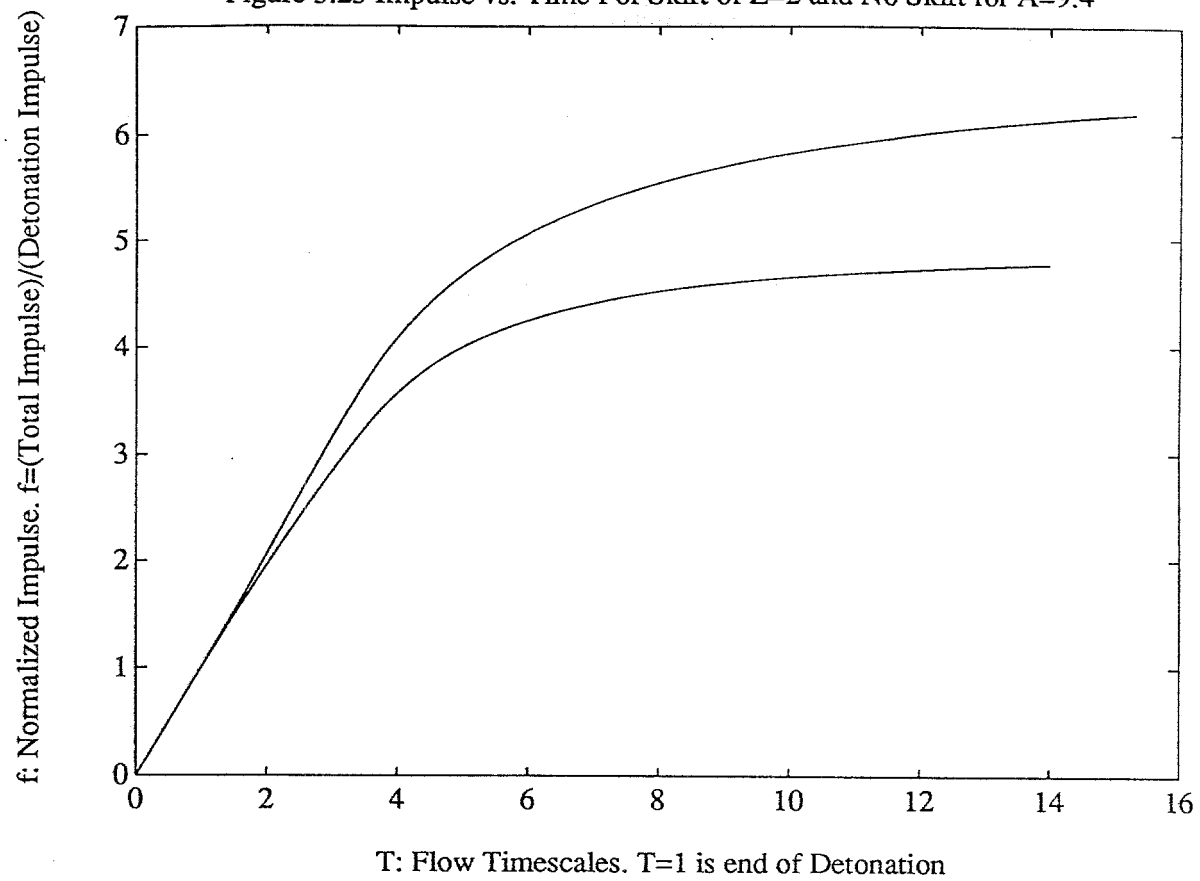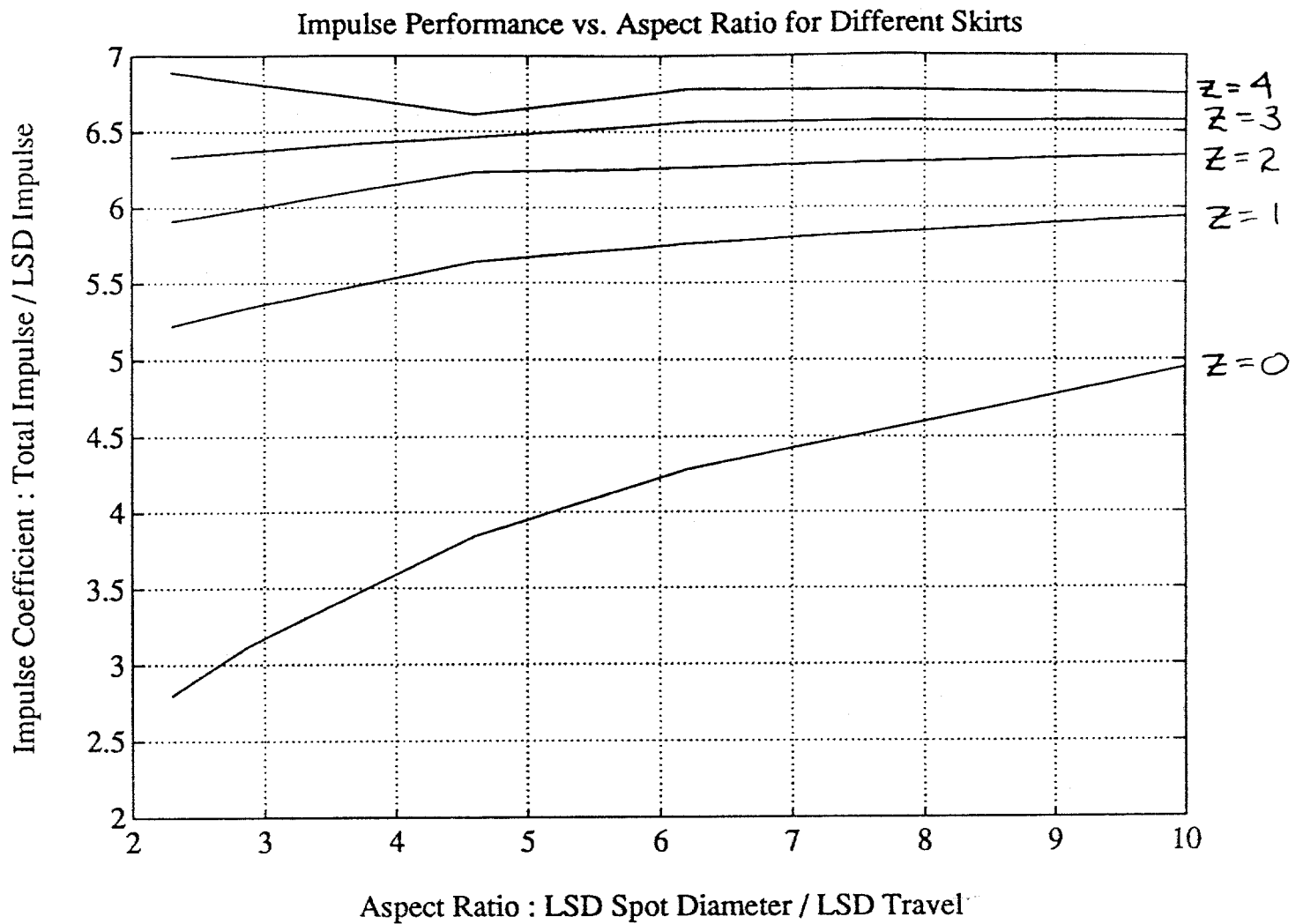
$$Z = \frac{Skirt\ Length}{LSD\ Length} = 0, 1, 2, 3, 4$$

$$Z = 0, \quad No\ Skirt$$

Figure 3.24

Sedov Series of Calibration Runs
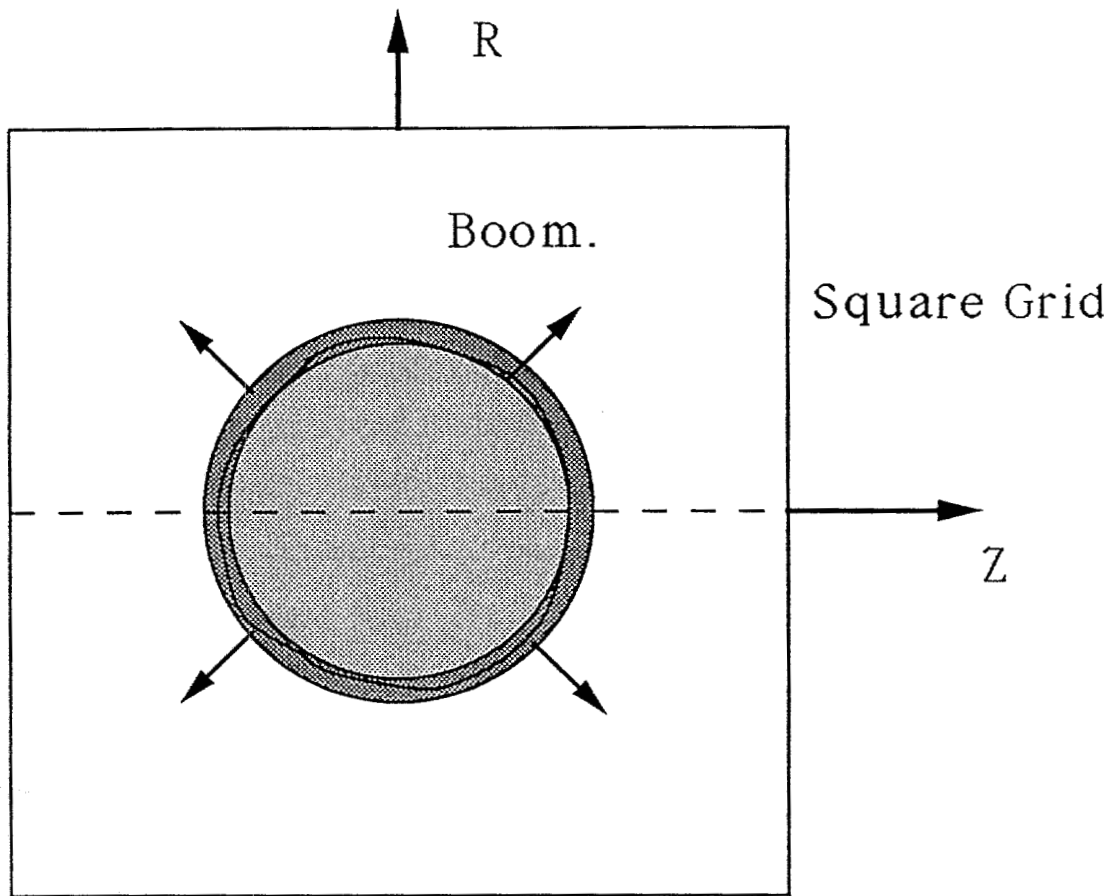
Impose a Spherically Symmetric Blast on a Square Grid as a Test of Axisymmetric Non-Steady Euler Algorithm.

Solution for Rwave: Rwavefront $= C \, t^{2/5}$

Solution for Field Behind Wave front: Sedov.

Figure 3.25

FIGURE 3.26a   Fit of Wave Trajectory with R=T**2/5

Smooth: T**2/5   Jagged: R/Rmax

Smooth: T=Time/TimeMax   Jagged: T-0.05 to Fit

Smooth: T**2/5   Jagged: R/Rmax
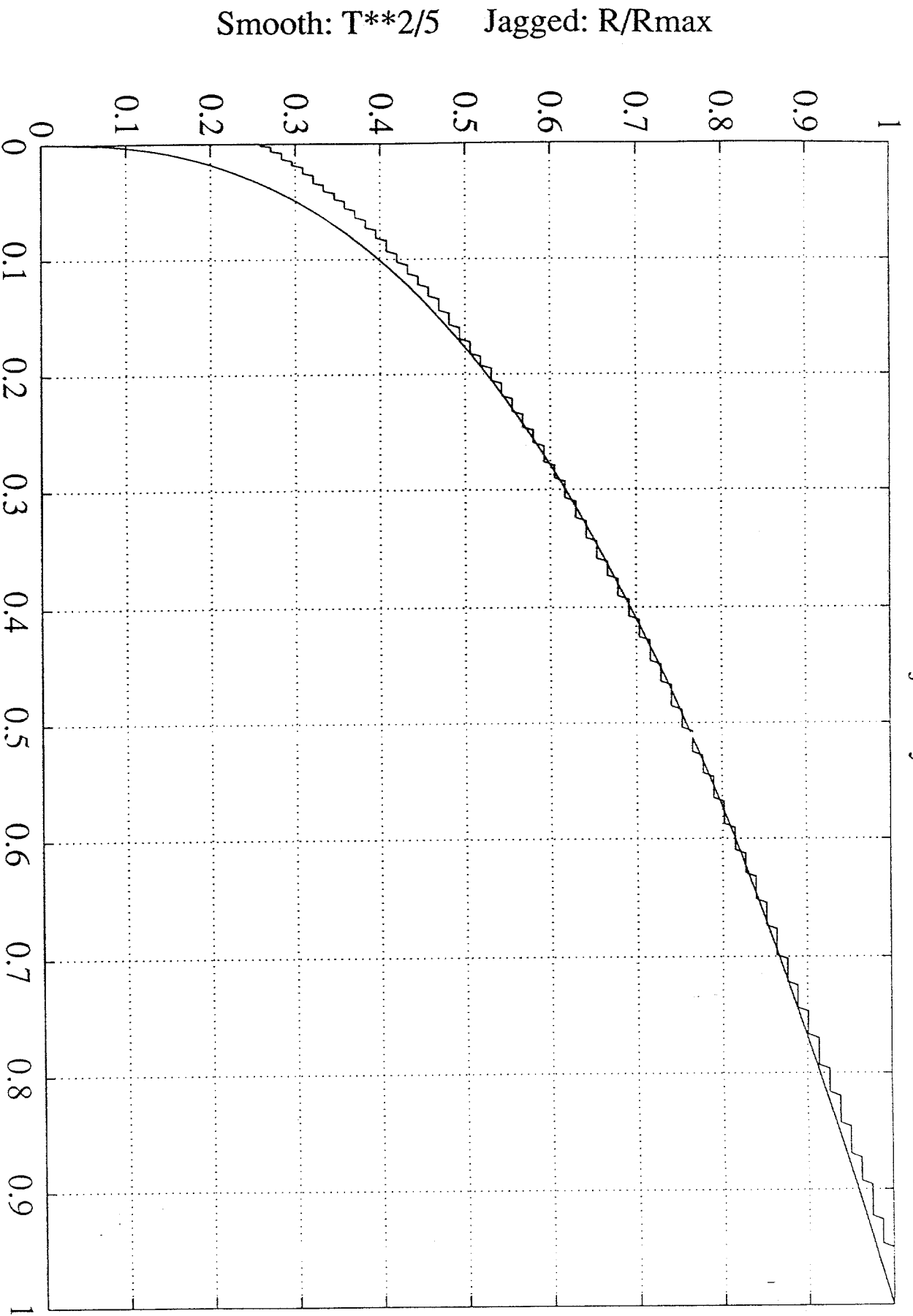
FIGURE 3.26b   Fit of Wave Trajectory with R=T**2/5
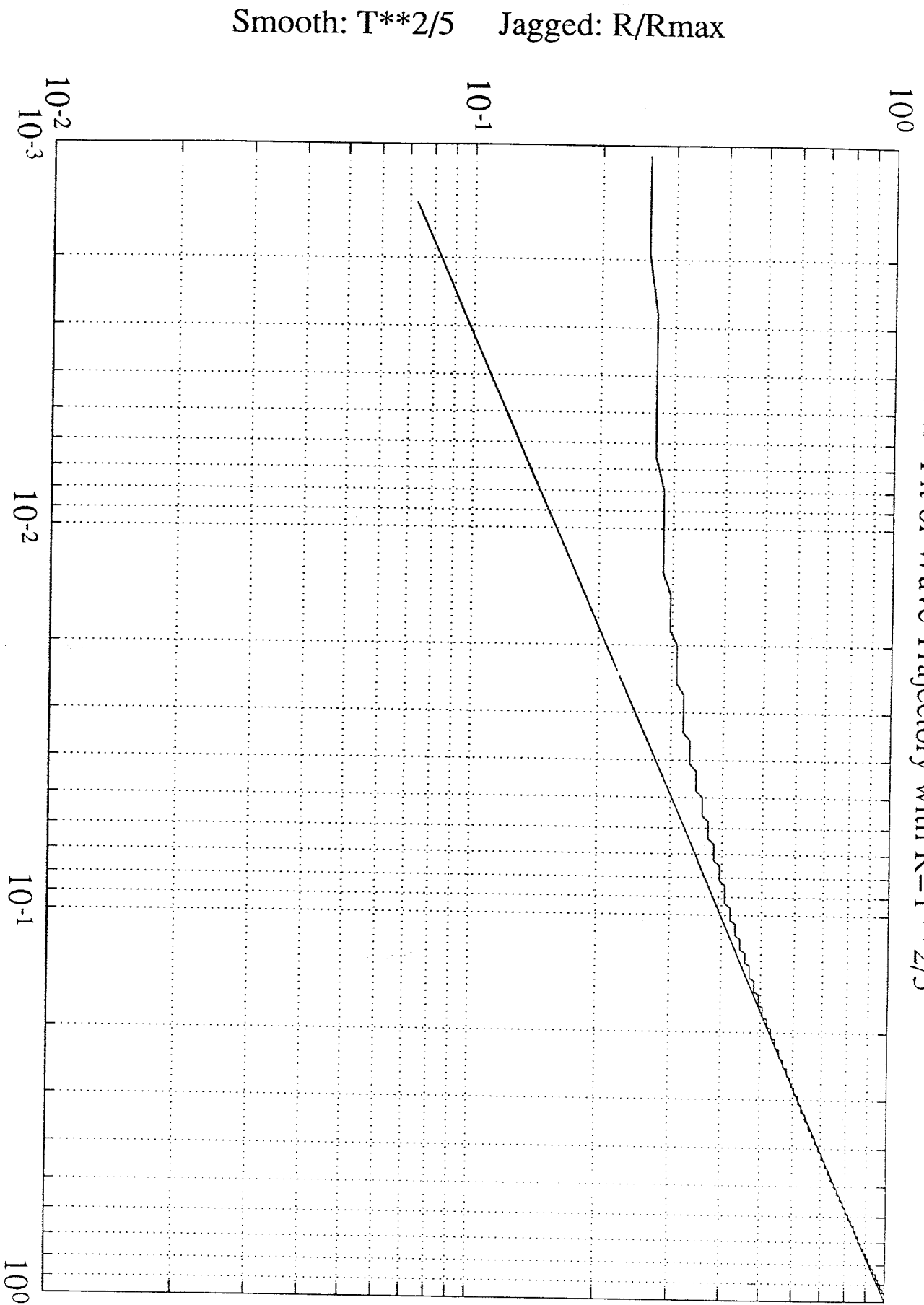
Smooth: T=Time/TimeMax   Jagged: T-0.05 to Fit

x10⁵ FIGURE 3.27 Pressure vs. Radius at Stations 0,1,2,3. Pambient=1
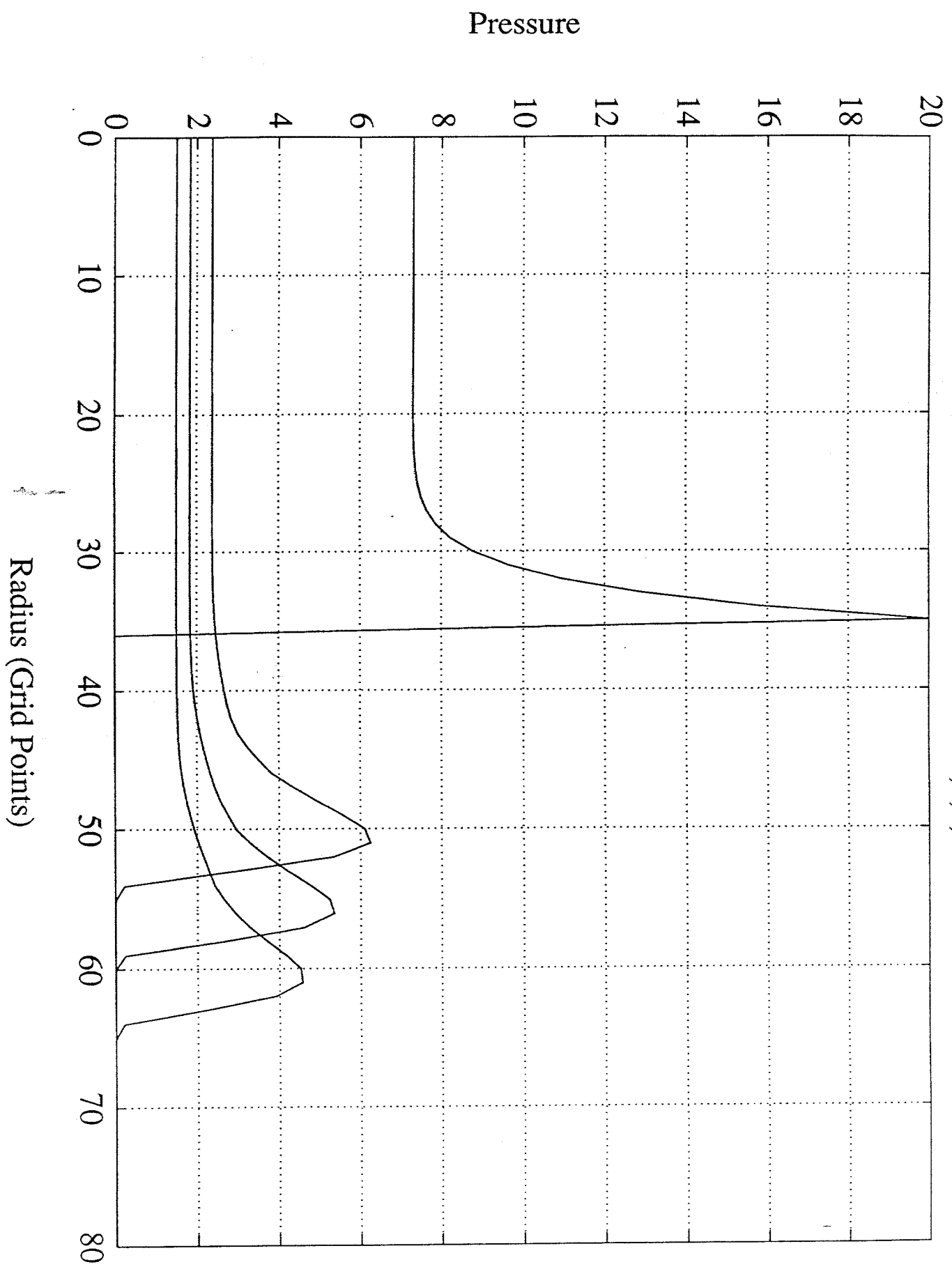
FIGURE 3.28 Density vs. Radius at Stations 0,1,2,3.
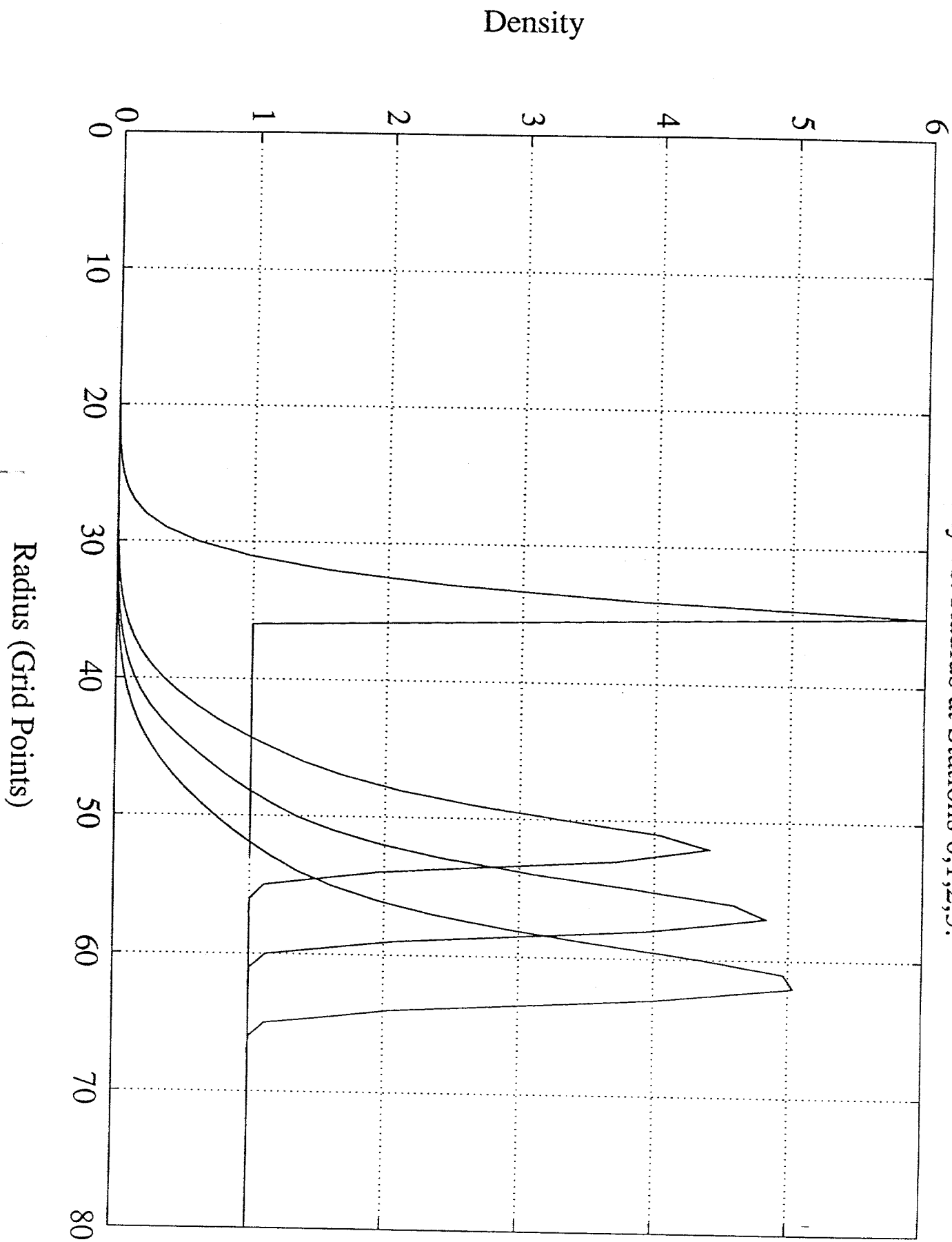
FIGURE 3.29   Nondimensional (r,P) Plot for Stations 0,1,2,3 : -, *, o, X
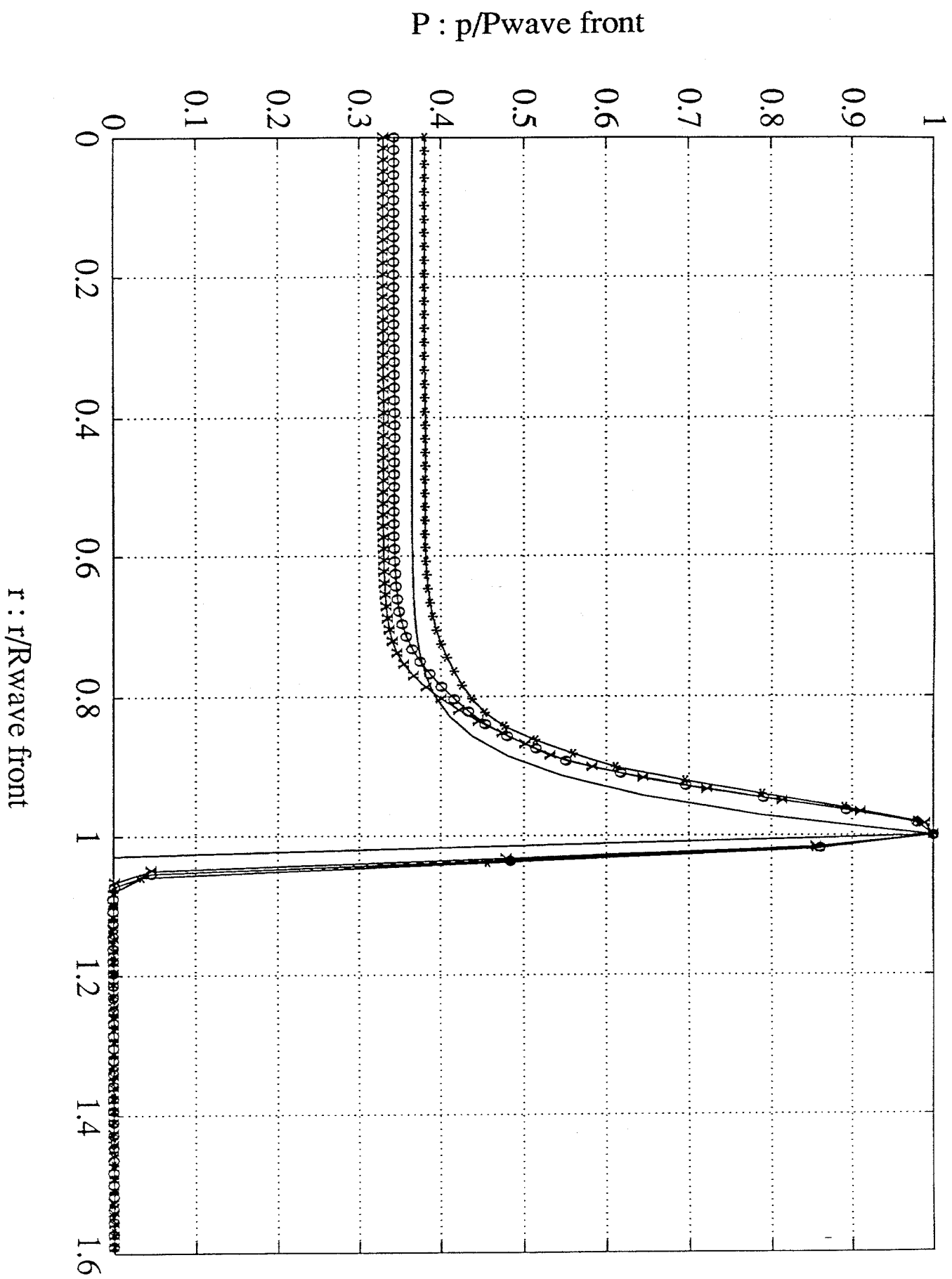
FIGURE 3.30 Density vs. r/Rwave for Stations 0,1,2,3 : -, *, o, x

Equilibrium Lithium Hydride

ε

kJ/kg

Laser
Propulsion

Gas State is within
a (ρ,ε) box with the
borders:

$20000 < \varepsilon < 120{,}000$

$.01 < \rho < .2$

ρ

kg/m^3
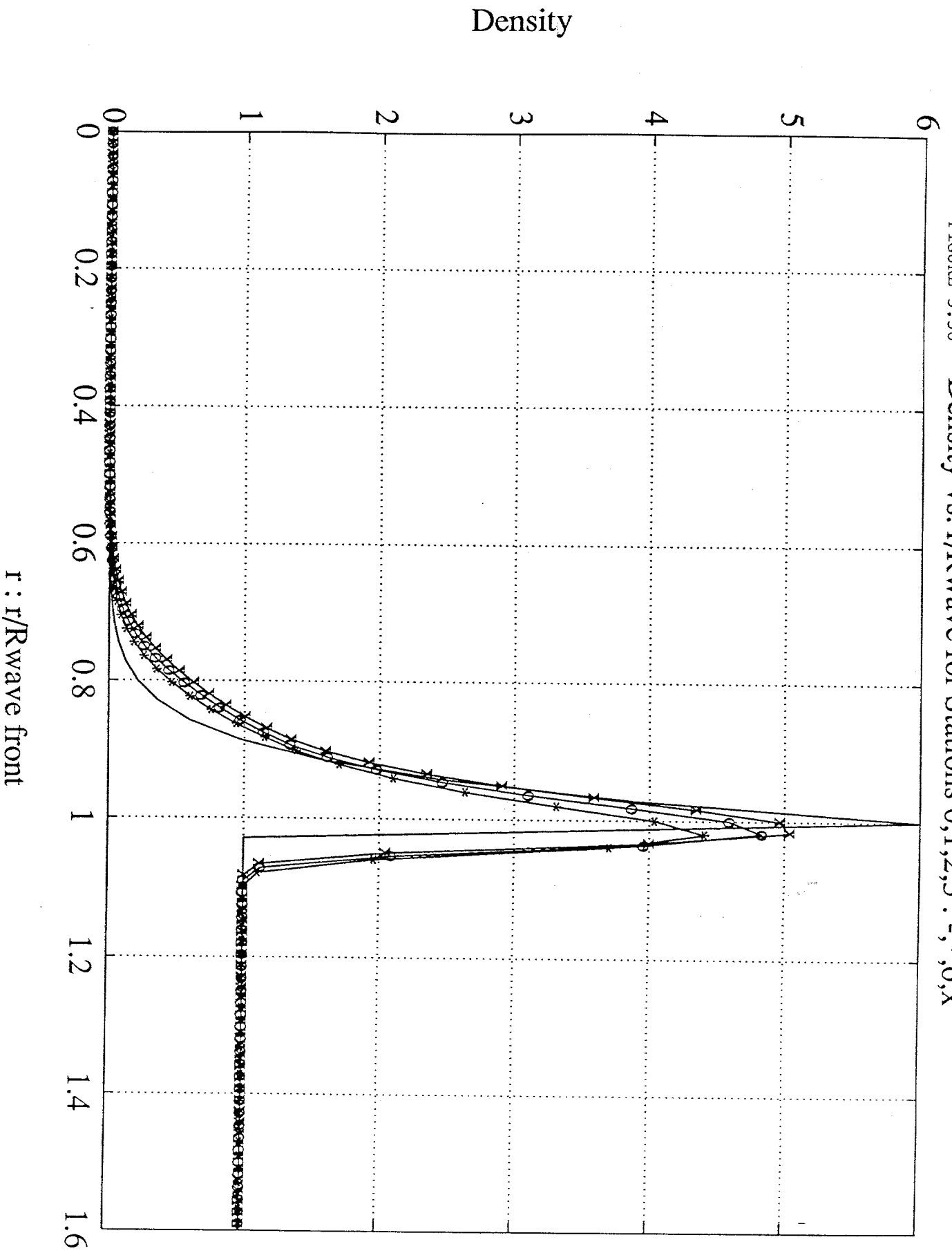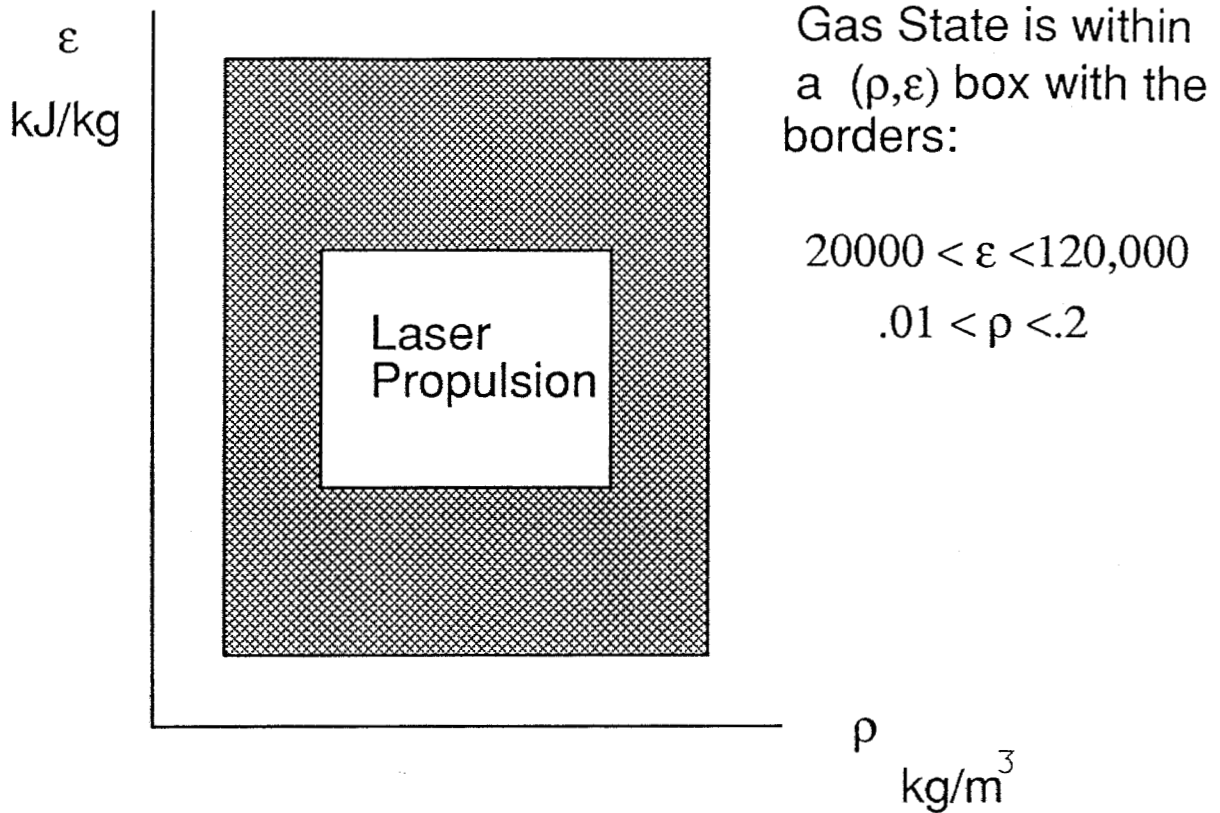
An Equilibrium Thermodynamic Package, borrowed
from NASA, which considers dissociation and ionization,
was used to generate a data-base covering the LiH laser
propulsion region above. The pressure data was modeled
using the functional form:

$$p = \rho \; f(\varepsilon)$$

The result: Equilibrium LiH behaves like a perfect gas with

$$\gamma = 1.2$$

Figure 4.1 Equilibrium Modeling Approach for LiH

Equilibrium and Model Pv product for LiH at rho = 0.05 kg/m^3

Internal Energy : kJ/kg

x10

Pv product : kJ/kg
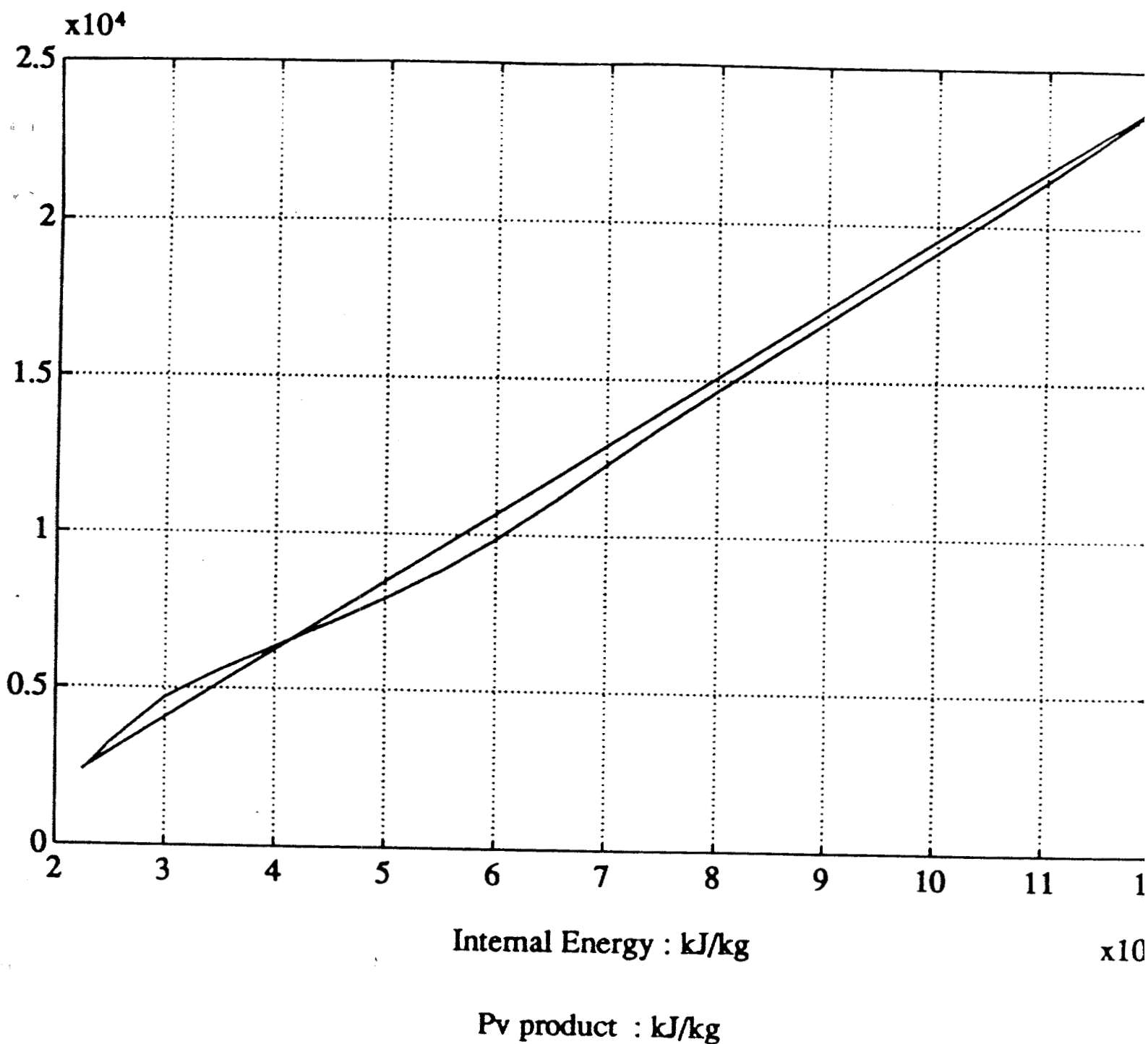
Figure 4.2

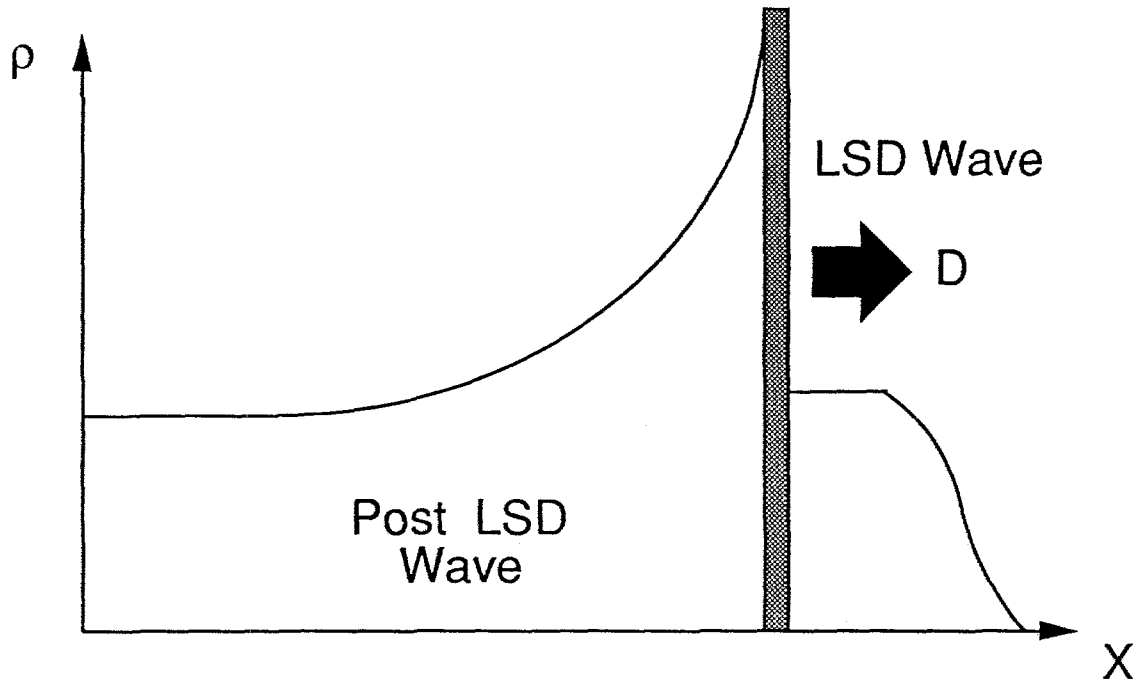Equilibrium and Model Speed of Sound for LiH at rho = 0.05 kg/m^3
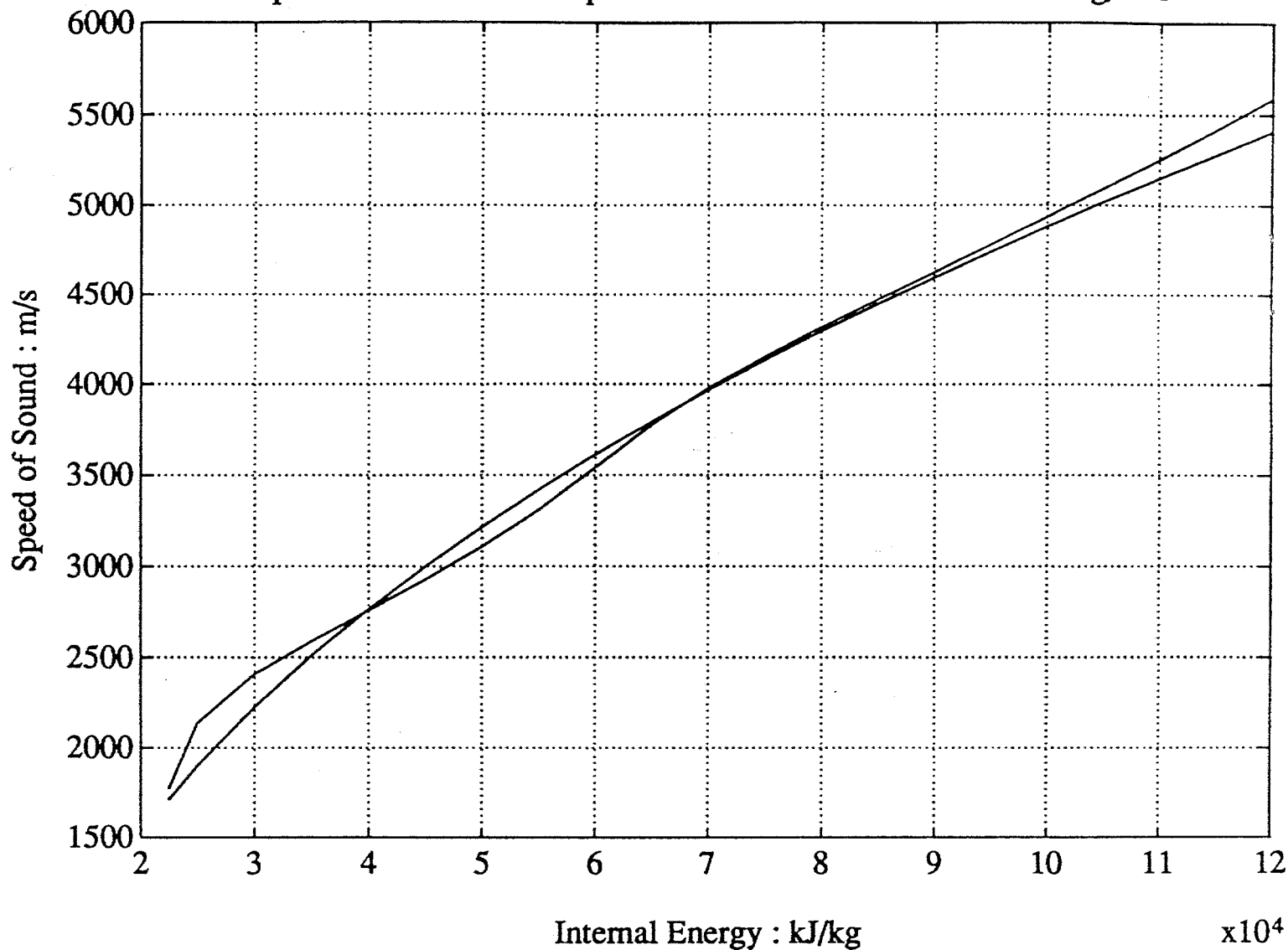
Figure 4.3

Chemically Frozen Lithium Hydride

In the Post LSD flow the LiH is fully dissociated and partially ionized. During LSD propagation and subsequent blast, the ionization is assumed to remain in equilibrium while the Hydrogen is assumed not to recombine -- to "freeze". This is because the recombination rates for
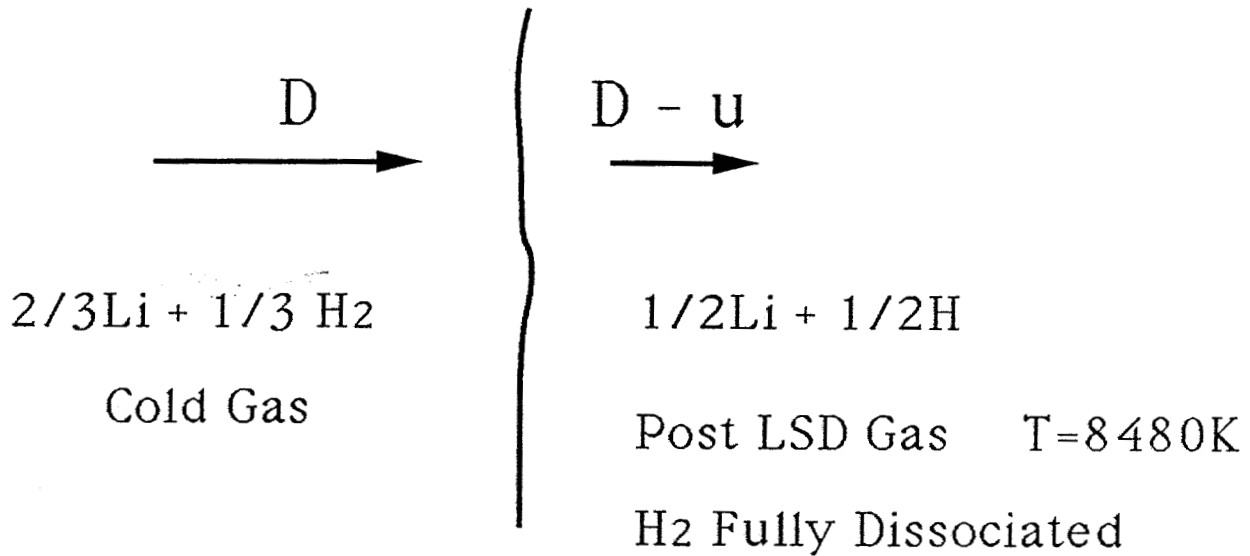
$$2H \longrightarrow H \qquad \text{and} \qquad Li + H \longrightarrow LiH$$

are slower than the flow timescales.

Using the Saha Equation for equilibrium ionization, a variable γ model has been constructed for the four species gas :   Li   H   Li +   e- .

Hot : $1.25 < \gamma < 1.6667$: Cold

Figure 4.4

Frozen Flow Losses for Lithium Hydride

$$D \longrightarrow$$

$$D - u \longrightarrow$$

2/3Li + 1/3 H2

Cold Gas

1/2Li + 1/2H

Post LSD Gas   T=8480K

H2 Fully Dissociated

Cold Gas is Ablated at Cost : 36,500 kJ/kg
LSD wave Dissociates the H2 at 4.5eV per Bond.
For PSI LSD wave, with D=8500 m/s, ρ_0 =0.1 kg/m^3
and Laser Flux of 5.2x10^6 W/cm^2 we have

Qlaser = 6.11 J/cm^2   : Main Pulse Heating
Qdiss = 2.68 J/cm^2   : Dissociation of H2
Qablate = 3.65 J/cm^2   : Ablation Cost

Total Qin: 9.76 J/cm^2. Available For K.E. :
6.11 J/cm^2 (full H2 recombination)
3.43 J/cm^2 (frozen: no H2 recombination)-

Figure 4.4 a

Recombination Kinetics for LiH

Consider the Reaction : $H_2 \rightleftharpoons 2H$

The Equilibrium Concentration of H_2 is negligible until the gas has cooled to the following (P , T) State:

$$\tau_{chem}$$

Case 1: P=10 atm T=5000K   2µs
Case 2: P=5atm   T=4200K   6µs
Case 3: P=1atm   T= 4200K   55µs

Reaction Rate analysis predicts that the expansion is frozen, while the 1-D core slug is in between Frozen and Equilibrium state.
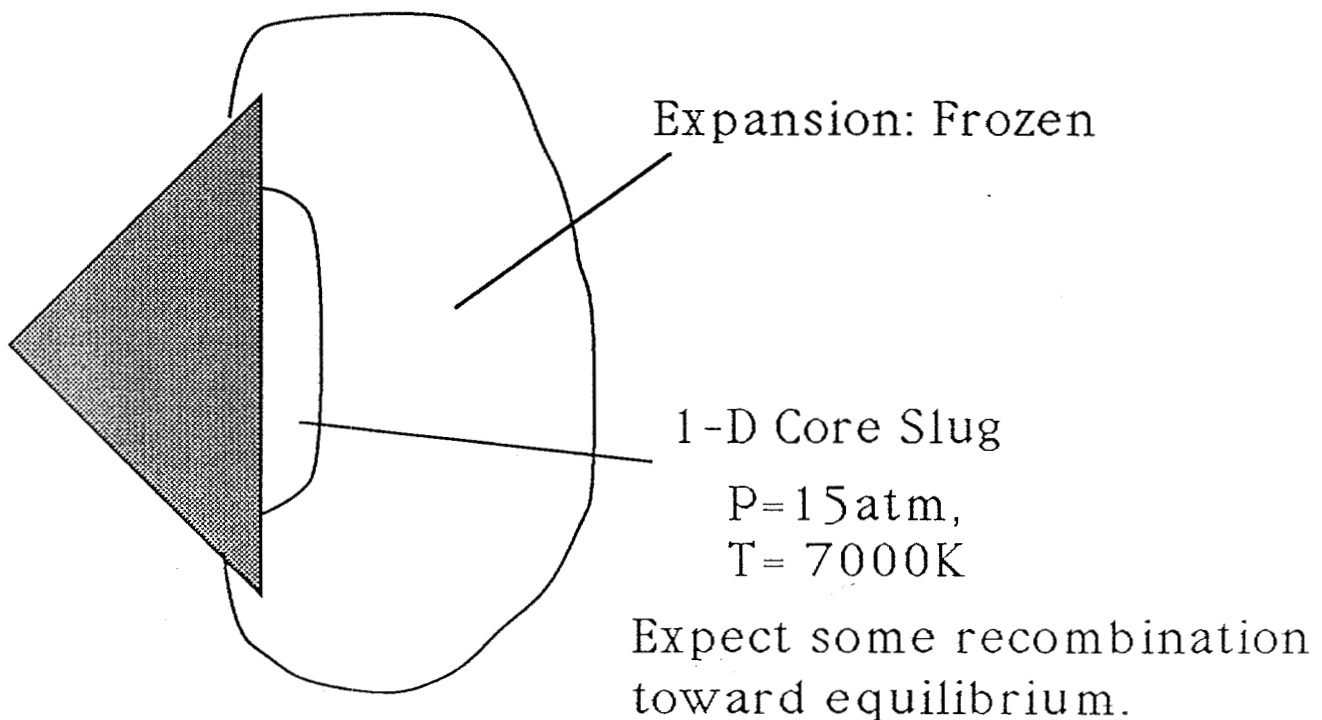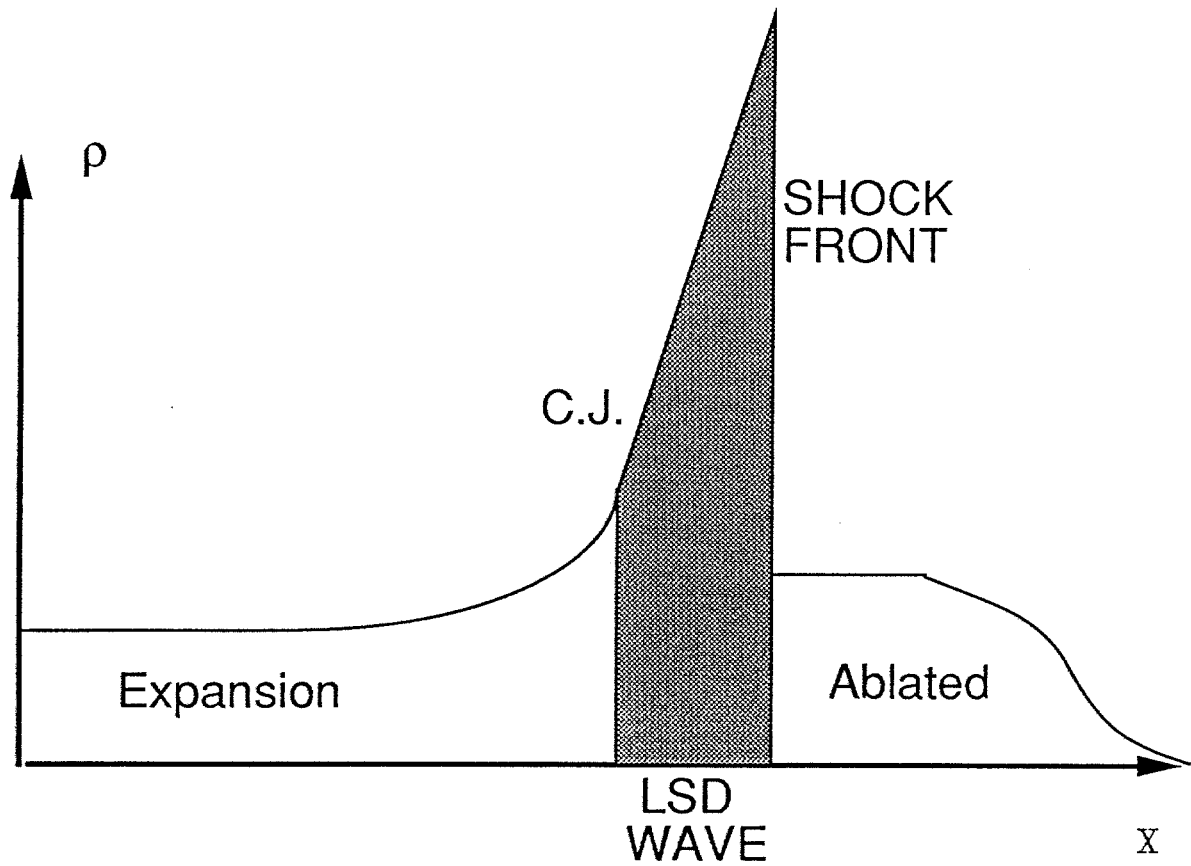

Expansion: Frozen

1-D Core Slug
    P=15atm,
    T= 7000K

Expect some recombination toward equilibrium.

Figure 4.5

Physical Sciences Inc. (PSI) Models the LSD wave
The Chapman Jouget point is their exit condition
The Ionization Model covers the Expansion

	ρ	u	c	P	γ	T
PSI	.1547	3000	5500	33	(1.2)	8480
MODEL	.1547	3000	5366	33	1.35	8980

Figure 4.6: Compatibility of Expansion with Detonation

The Ion model is compared to the PSI model. Units of
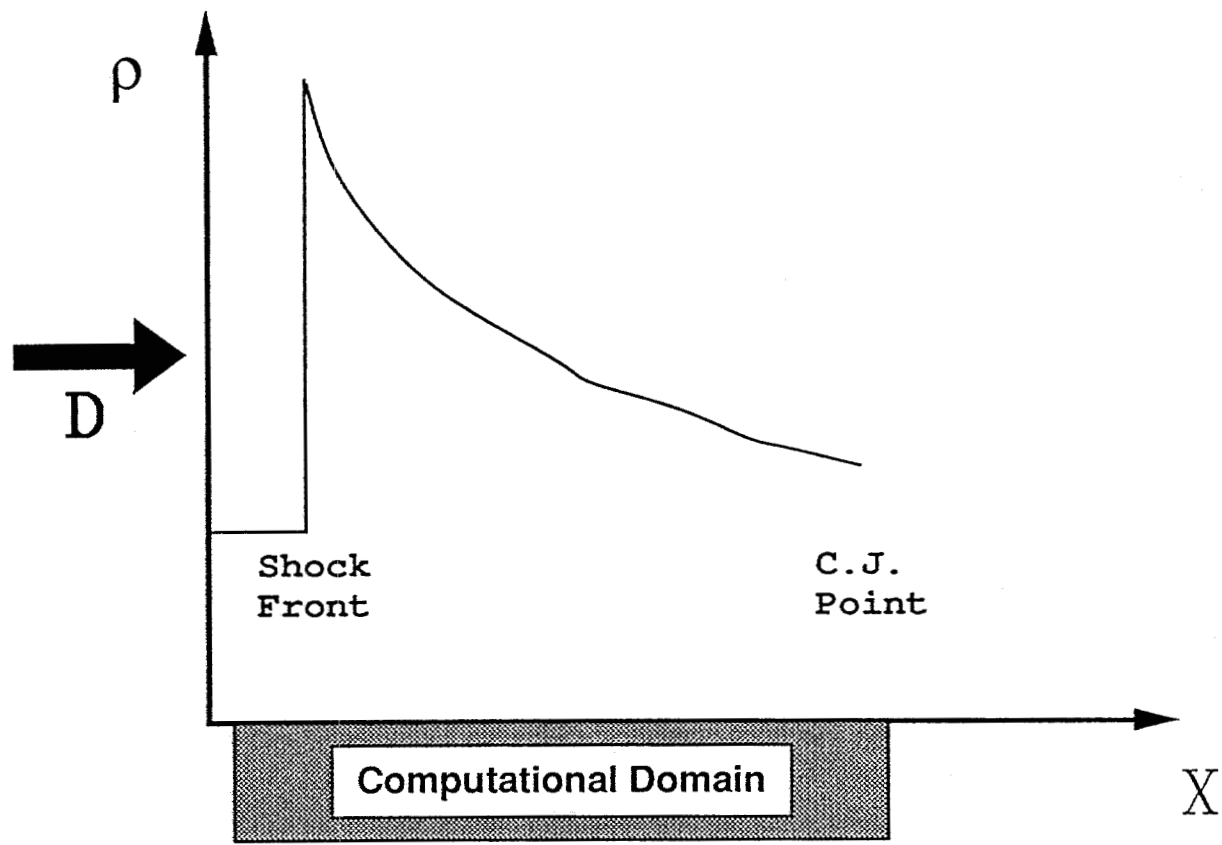u and c are (m/s). Pressure is in (atm) and T is in
Kelvins.

Figure 4.7 : Physical Sciences LSD Wave Model

The x coordinate is wave fixed. Gas enters the
Computational Domain in the cold state at the
speed D. A shock wave preceeds the main region of the
absorption of the laser flux. The exit condition is the
Chapman-Jouget Point, where the gas velocity equals the
speed of sound in these coordinates. For the case of
D=8500 m/s, this value of u = c is 5500 m/s.

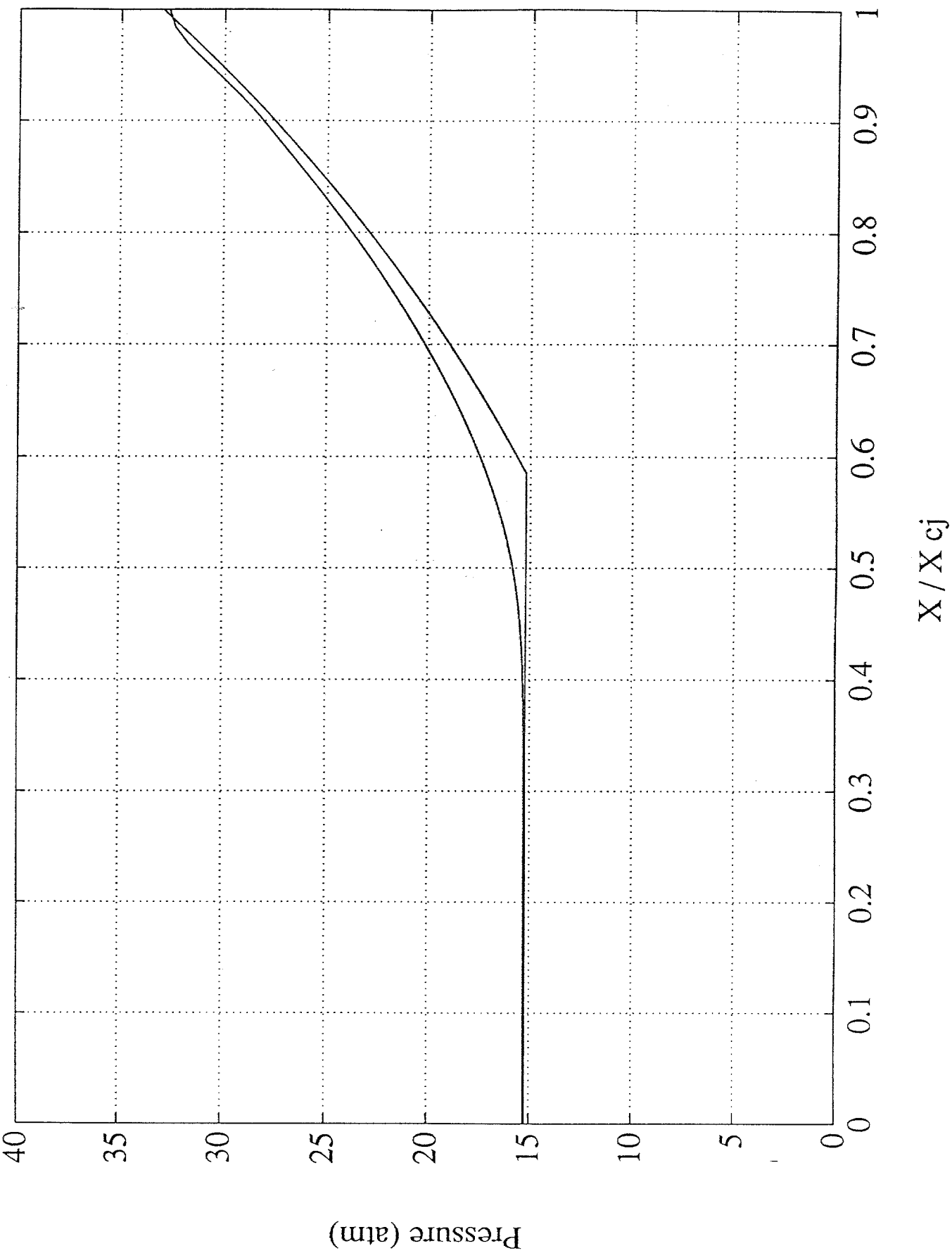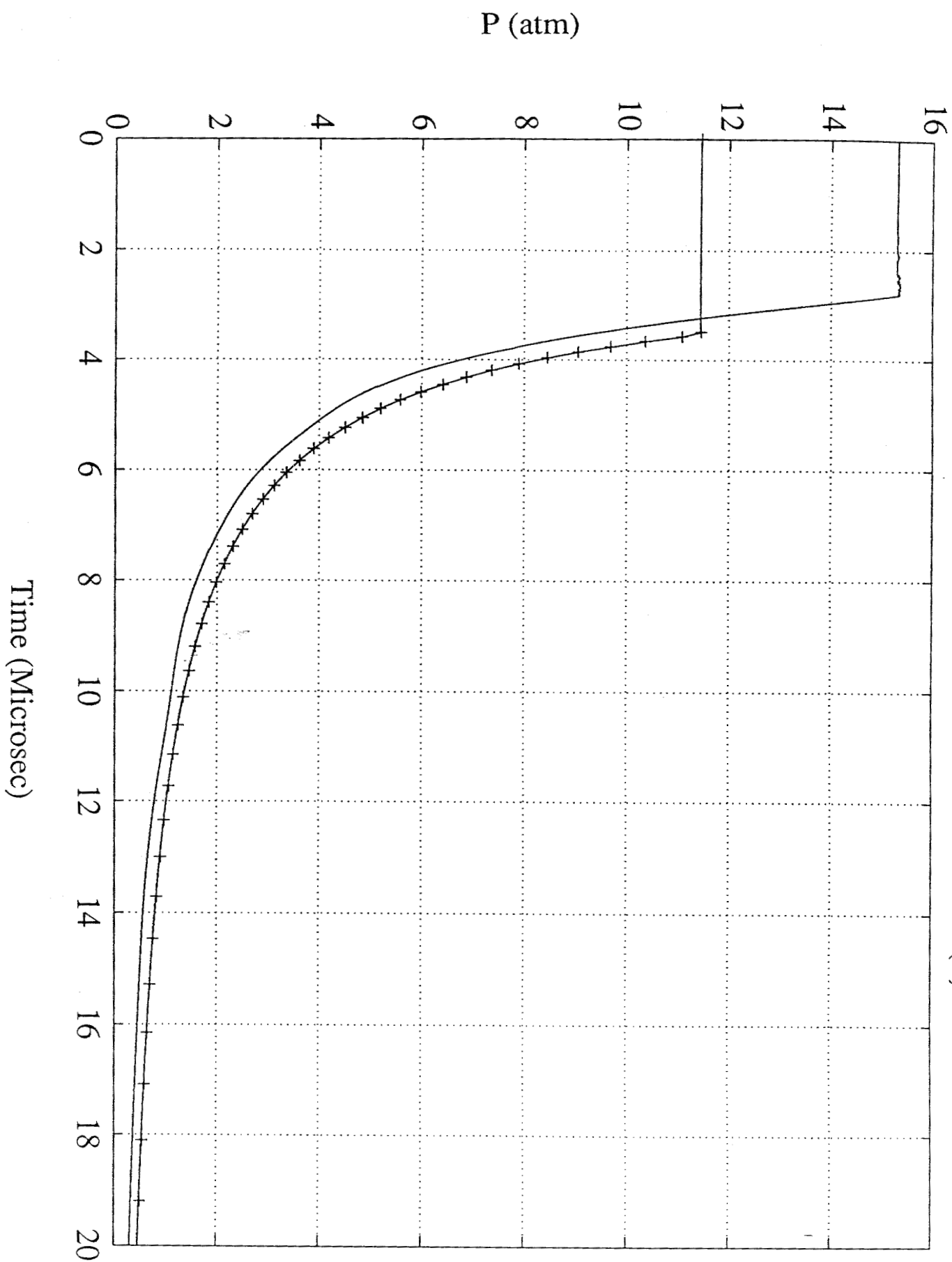FIGURE 4.8   Expansion Pressure Profile. Real and Gamma=1.35 with Same CJ conds.

FIGURE 4.9   Core Pressure vs. Time for Real Gas and Ideal Gas(+) Thruster

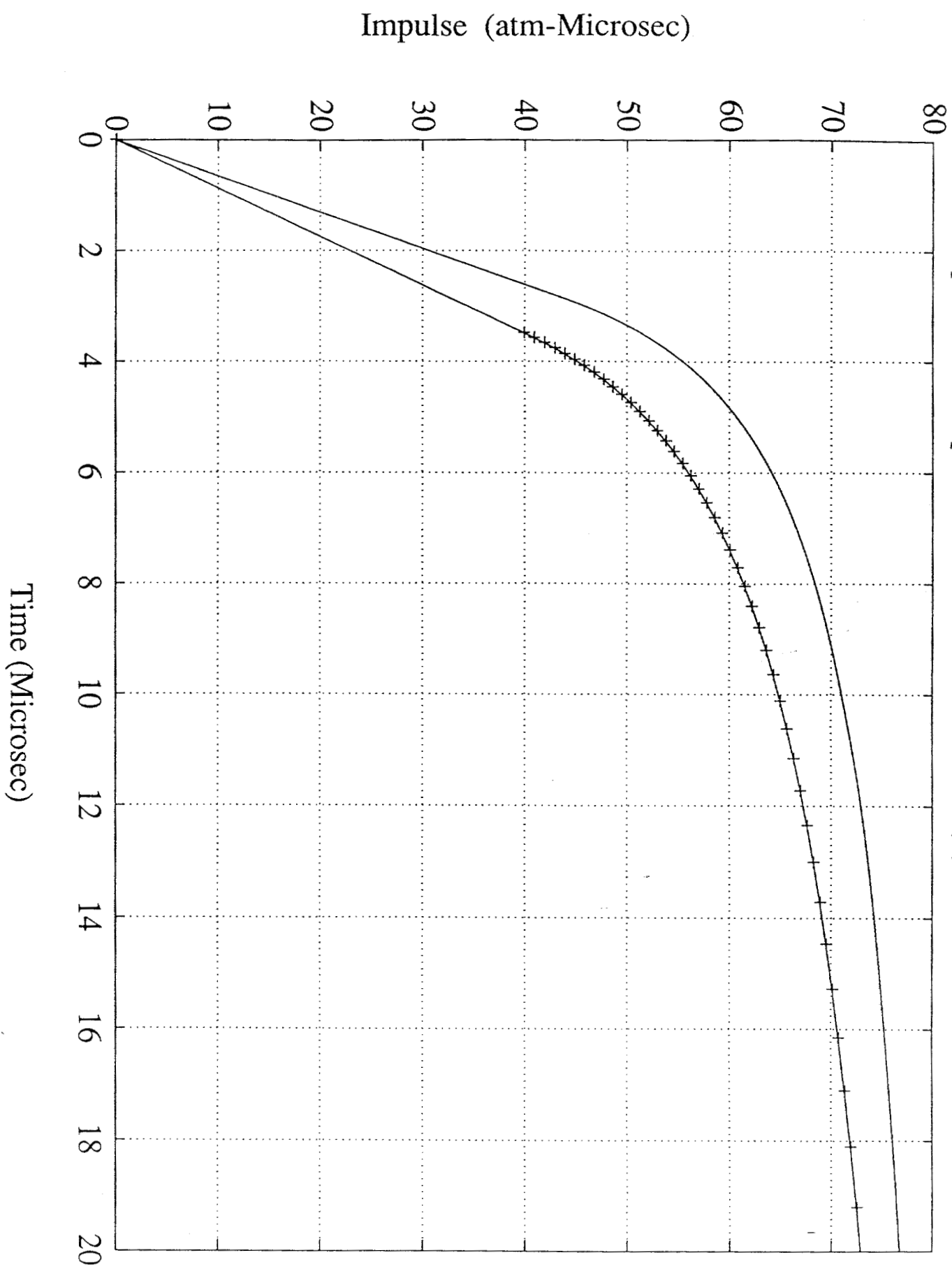FIGURE 4.10   Impulse Development for Real Gas and Ideal(+) Gas. 1 Microsec Pulse

FIGURE 4.11   Impulse Development for Real Gas and Ideal(+) Gas Thruster